Surface & Coatings Technology

On the sliding wear and solid particle erosion behaviour of HVOF-sprayed CoNiCrAlY coatings and NiCrCoTi substrates in dependence of the oxidation dwell time at 900 °C

--Manuscript Draft--

Manuscript Number:	SURFCOAT-D-22-04005
Article Type:	VSI:10RIPT
Keywords:	CoNiCrAlY; NiCrCoTi; Post-spray treatment; Microhardness; Sliding wear; Solid particle erosion
Corresponding Author:	Markus Kiryc, M.Eng. Westphalian University of Applied Sciences GERMANY
First Author:	Markus Kiryc, M.Eng.
Order of Authors:	Markus Kiryc, M.Eng.
	Deniz Kurumlu
	Gunther Eggeler
	Robert Vaßen
	Gabriela Marginean
Abstract:	In high temperature sections up to 900 °C overlay MCrAlY coatings are frequently used to increase the life time of Ni based components in technical applications. Beside oxidation protection, coatings resistance to sliding wear and solid particle erosion is required during different service operation regimes. In the present work the focus is set on the wear behaviour of HVOF-sprayed CoNiCrAlY coatings deposited on a NiCrCoTi substrate (Nimonic 90) and of uncoated substrate, before and after oxidation for different dwell times up to 1200 h at 900 °C. The samples were investigated in respect to their behaviour under dry sliding wear conditions and solid particle erosion at ambient temperatures. Sliding wear was tested by means of pin-on-disc method. Solid particle erosion was conducted using an in-house developed air jet erosion testing rig. Moreover, microhardness indentations HV 0.1 were performed in order to determine changes of materials hardness depending on the heat exposure. Microstructural and phase analysis was performed by means of scanning electron microscopy (SEM) combined with energy-dispersive X-ray spectroscopy (EDX) and by X-ray diffraction (XRD). Confocal laser scanning microscopy (CLSM) was used to measure thickness, hardness indentations and wear degree of the surfaces. Samples mass losses were considered as well. Coatings performance is pointed out in comparison with that of the uncoated NiCrCoTi substrate, set to same conditions. It could be shown, that the sliding wear and particle erosion behaviour of the investigated samples strongly depends on materials microstructure and chemical composition. The accelerated oxidation reaction kinetics of NiCrCoTi substrate lead to the formation of a thicker oxide scale, which exhibited protective effects of a glaze-layer during sliding wear. However, the oxide scales do not benefit the protection of solid particle erosion.
Suggested Reviewers:	Lech Pawlowski lech.pawlowski@unilim.fr
	Giovanni Bolelli giovanni.bolelli@unimore.it
	Shrikant Joshi shrikant.joshi@hv.se

Cover Letter

Dear Editor-in-Chief,

We are kindly sending you an article referring to the content of the contribution to the 10RIPT with the title "*On the sliding wear and solid particle erosion behaviour of HVOF-sprayed CoNiCrAlY coatings and NiCrCoTi substrates in dependence of the oxidation dwell time at 900 °C*" to be submitted as a research article in a special issue of Surface and Coatings Technology (Elsevier).

The background and the objectives of this research are as follows:

Metallic high temperature components are commonly subjected in practise to a collective detriment by sliding wear and solid particle erosion. In many studies the main focus is frequently set on investigations of tribological issues during high temperature conditions. However, on the one hand, sliding wear and particle erosion are deterioration processes also known to occur during low or ambient temperatures. On the other hand, wear is not a continuous phenomenon. This implies possibilities of a sudden occurring wear process on mechanically intact and well oxidised surfaces of already heat exposed material. Therefore, the objective of the current research was to investigate an influence of a prior oxidation on CoNiCrAlY coating's and NiCrCoTi substrate's performance regarding tribological issues. Uncoated substrate was designated as a reference in order to make it possible to classify coating's results. For the investigations, a previous isothermal oxidation procedure at 900 °C for 5 dwell times was performed. Studies on microstructure, chemical composition and its influence on material's hardness, sliding wear and solid particle erosion were conducted. For solid particle erosion studies, a testing rig was in-house developed and used.

This submission is original unpublished work, is not being submitted for publication elsewhere and is not under review at any other publication.

We hope that the editorial board will consider, assess and agree on the interests of this research.

With kind regards,
Markus Kiryc on behalf of the authors

Gelsenkirchen, 14.10.2022

Highlights

1. Characterisation of oxidised HVOF-sprayed CoNiCrAlY coatings and Nimonic 90
2. Microhardness profiles along substrate/coating interfaces
3. Sliding wear and particle erosion of oxidised CoNiCrAlY coatings and Nimonic 90
4. Influence of the grown oxide scale on the sliding wear behaviour
5. Dependence of erodent impact angle on the particle erosion behaviour

On the sliding wear and solid particle erosion behaviour of HVOF-sprayed CoNiCrAlY coatings and NiCrCoTi substrates in dependence of the oxidation dwell time at 900 °C

Markus Kiryc[a], Deniz Kurumlu[a], Gunther Eggeler[b], Robert Vaßen[c], Gabriela Marginean[a]

[a]Westfälische Hochschule Gelsenkirchen, Neidenburgerstraße 43, 45897, Gelsenkirchen, Germany, markus.kiryc@w-hs.de, deniz.kurumlu@w-hs.de, gabriela.marginean@w-hs.de

[b]Ruhr-Universität Bochum, Universitätsstraße 150, 44801, Bochum, Germany, gunther.eggeler@ruhr-uni-bochum.de

[c]Forschungszentrum Jülich GmbH, Wilhelm-Johnen-Straße, 52425, Jülich, Germany, r.vassen@fz-juelich.de

Corresponding author: Markus Kiryc, e-mail: markus.kiryc@w-hs.de,Telephone: +49 209 9596 162, Fax: +49 209 9596 207, Westfälische Hochschule Gelsenkirchen, Neidenburgerstraße 43, 45897, Gelsenkirchen, Germany

Abstract

In high temperature sections up to 900 °C overlay MCrAlY coatings are frequently used to increase the life time of Ni based components in technical applications. Beside oxidation protection, coatings resistance to sliding wear and solid particle erosion is required during different service operation regimes. In the present work the focus is set on the wear behaviour of HVOF-sprayed CoNiCrAlY coatings deposited on a NiCrCoTi substrate (Nimonic 90) and of uncoated substrate, before and after oxidation for different dwell times up to 1200 h at 900 °C. The samples were investigated in respect to their behaviour under dry sliding wear conditions and solid particle erosion at ambient temperatures. Sliding wear was tested by means of pin-on-disc method. Solid particle erosion was conducted using an in-house developed air jet erosion testing rig. Moreover, microhardness indentations HV 0.1 were performed in order to determine changes of materials hardness depending on the heat exposure. Microstructural and phase analysis was performed by means of scanning electron microscopy (SEM) combined with energy-dispersive X-ray spectroscopy (EDX) and by X-ray diffraction (XRD). Confocal laser scanning microscopy (CLSM) was used to measure thickness, hardness indentations and wear degree of the surfaces. Samples mass losses were considered as well. Coatings performance is pointed out in comparison with that of the uncoated NiCrCoTi substrate, set to same conditions. It could be shown, that the sliding wear and particle erosion behaviour of the investigated samples strongly depends on materials microstructure and chemical composition. The accelerated oxidation reaction kinetics of NiCrCoTi substrate lead to the formation of a thicker oxide scale, which exhibited protective effects of a glaze-layer during sliding wear. However, the oxide scales do not benefit the protection of solid particle erosion.

Keywords: CoNiCrAlY, NiCrCoTi, Post-spray treatment, Microhardness, Sliding wear, Solid particle erosion

1. Introduction

A protection of technical components from external influences is nowadays implemented by the industry in direct correlation with the operating conditions. Therefore, surfaces of components material can be either actively modified by thermal diffusion or in much common cases, passively treated by applying a protective overlay coating [1–5]. Technical components for applications in high temperature regions, present in particular in gas turbine processes, require oxidation resistance to maintain its respective desired performance. Although Ti-based or Ni-based alloys are frequently considered due to their mechanical properties for elevated temperature issues [6–12], deposition of coatings is recommended to impart a sufficient long-term oxidation protection [13]. An effective and reliable protection from surface oxidation has been achieved by using metallic MCrAlY (M = Ni, Co or Fe) coatings due to its combined superior mechanical properties and diffusion-controlled oxidation behaviour [1,2,14–22]. This type of coatings is frequently applied on the one hand as an essential bond coat in multilayer thermal barrier coating systems [1,18,23,24], used in temperature regions more than 1200 °C. Such elevated temperatures occur during gas turbine processes in combustion chambers and first stages of turbine blading. On the other hand, MCrAlY coatings benefit as monolayer materials oxidation protection during exposure at temperatures of 900 °C and below [1,25–27]. Especially the composition CoNiCrAlY is known for having advantageous properties under the above mentioned conditions [2], which can prevail in second/third stage of gas turbine or compressor regions [20]. However, components operating in lower temperature regions (< 900 °C) such as compressor blades and vanes are more likely be subjected to a collective detriment by external influences, having a direct effect on their performance. Sliding wear and solid particle erosion (SPE) are the most present of possible tribological issues, which can be attributed to many different environmental and technical reasons [5,10,20,28–33]. Although abrasion and erosion resistant coatings are frequently used in multilayer systems to combat the mentioned damages, application of MCrAlY coatings on engine components is justified due to technical and economic benefits [3,20,33,34]. However, pure MCrAlY coatings are rather known for insufficient and poor wear behaviour [15]. In tribological systems, CoNiCrAlY metallic coatings suffer to severe adhesive wear [26], especially when subjected to sliding wear against harder (ceramic) counterpart. Therefore much effort has been done to improve coating's properties by addition of reinforcements, mainly with ceramic phases such as Al_2O_3 [20,35–37]. Well investigated oxide-dispersion strengthened (ODS) MCrAlY coatings are mostly in focus of many researches to combat oxidation and wear at the same time. However, the results are controversially discussed [20,27,38]. In many studies the main focus is frequently set on investigations of sliding wear behaviour during high temperature conditions. On ODS MCrAlY coatings and Ni-based alloys, well described tribo-layers termed as glaze-layers are reported to develop during a high temperature exposure, which can mitigate wear [11,20,26,27,39–42]. These rather thicker and distinct grown layers are referred to be differently to thermally-grown oxides, since the growth mechanisms are different [40]. Beside sling wear, detriment of MCrAlY is frequently observed to be caused by erosive or impact wear. Especially investigations on cumulative effects of mechanical (erosion) and chemical (oxidation) degradation have been in focus in studies on the materials behaviour during high temperature impingement [10,28,30,37,42]. In any case, temperature related effects on coating's microstructure, mechanical properties and simultaneous formation of new oxides are assumed to be key factors controlling materials sliding wear or SPE behaviour when exposed to high temperature [12,36,41]. However, wear performance of pre-oxidised materials tested at ambient temperature is not well investigated yet. The objective of the current research was to investigate an influence of a prior oxidation on CoNiCrAlY coating's and NiCrCoTi substrate's performance regarding tribological issues. Uncoated substrate was designated as a reference in order to make it possible to classify coating's results. A previous isothermal oxidation procedure at 900 °C for 5 dwell times was performed. Studies on microstructure, chemical composition and its influence on materials hardness, sliding wear and solid particle erosion were conducted.

2. Methodology

2.1. Materials and methods

A Ni-based superalloy NiCrCoTi with the nominal chemical composition Ni-Cr20-Co18-Ti, wt.-% was used as base material due to its relevance in high temperature applications [8]. Likewise, this Ni-based alloy is selected as reference due to its similar qualitative chemical composition regarding coating’s elements. The hot rolled, descaled and softened NiCrCoTi sheet was procured and prepared to cuboidal (~ 40 mm x 30 mm x 5 mm) samples at HARALD PIHL GmbH, Mönchengladbach, Germany. The surfaces of the NiCrCoTi substrate samples were grid-blasted with alumina prior to the coating deposition. CoNiCrAlY overlay coatings with the nominal composition Co-32Ni-21Cr-8Al-0.5Y, wt.-% and a nominal thickness of 170 µm were HVOF-sprayed (DJ2600, Oerlikon Metco, Wohlen, Switzerland) using the feedstock powder Amdry 995 (Oerlikon Metco, Wohlen, Switzerland). Coatings thickness were based on typical values used in industry [24,43]. The chemical compositions of the powder material and the substrate are presented in Table 1. Coated and reference material surfaces were ground down to 150 µm using 1200 grit SiC abrasive paper and cleaned with ethanol before the oxidation procedure.

2.2. Oxidation procedure

The prepared coated and reference materials were oxidised in normal atmosphere up to 1200 h at 900 °C (Nabertherm Universal N7/H Furnace, Lilienthal, Germany). An equal number of samples was taken out of the furnace after a predefined oxidation dwell time of 10 h, 100 h, 350 h, 700 h and final 1200 h, respectively. Thus, a total number of 6 states was considered (Table 2), including the initial state of 0 h. For sampling, the furnace was slowly cooled to room temperature with a cooling rate of 1.5 °C/min. Thereafter the furnace was heated up again to 900 °C with a heating rate of 30 °C/min. After the oxidation procedure the heat exposed samples were not mechanically influenced, for example by grinding or cleaning.

2.3. Microstructural and mechanical characterisation

The microstructure of the investigated samples was characterised in each state before and after the specified oxidation dwell time. Embedded cross sections of the samples were ground to finally 4000 SiC paper and then polished with diamond suspensions (6 µm, 3 µm, 1 µm). Samples microstructure and surface were analysed by means of scanning electron microscopy (SEM: JEOL JSM-IT300 with LaB6-cathode, JEOL Ltd., Tokyo, Japan) and energy-dispersive X-ray spectroscopy (EDX: AMATEK EDAX Octane Elite). Images were acquired using backscattered electron (BSE) mode. X-ray diffraction (XRD: X’Pert MPD System with Cu-anode, Phillips, The Netherlands) analyses were carried out to investigate the phase evolution using XRD Philips X’Pert High Score 3.0 (PANalytical) and X’Pert Data Collector. At least 3 materials states (0 h, 350 h and 1200 h) were analysed at the surface and below. For the latter investigations, samples were ground after oxidation procedure in order to remove oxidised surfaces. Confocal laser scanning microscopy (CLSM: Keyence VK-X260K, Keyence Corporation, Osaka, Japan) was used to assess an overview evaluation of the developed microstructure together with the grown oxide scale. Inhomogeneities, such as delamination, cracks, pores, unmolten or oxidized particles and splat boundaries were likewise evaluated. Top-view and cross-section CLSM images (150× objective ~ 94.50 µm × 70.80 µm with resolution of 2048×1536 pixel) were recorded for two samples of each state. 10 equidistant and perpendicular to the materials surface measurement lines were placed in cross sections areas of width ~ 430 µm (parallel to the surface) and height ~ 100 µm to 200 µm (perpendicular to the surface). Coating thickness measurement and delimitation of respective microstructure characteristics was carried out manually. The average values together with the standard deviation were calculated based on 10 measurements. Microhardness measurements provide not only materials hardness values but also information concerning materials heterogeneity. Changes in microhardness lead to changes in materials mechanical properties, which are related to materials wear behaviour. Therefore, microhardness indentations HV 0.1 (100 gf) were performed according to ASTM E384-17 [44] on polished cross sections using a Vickers indenter (Hardness testing machine, ZwickRoell, ZHVµ-M, Ulm, Germany). For each sample at least 5 indentations were conducted for each certain distance (Fig. 1). Representative microhardness profiles for all states have been determined by statistical evaluation of 2 samples for each state, where the errors are equal to the standard deviation.

2.4. Sliding wear

Sliding wear tests regarding sliding wear resistance and coefficient of friction (COF) evolution were performed against 6 mm diameter spherical alumina (Al_2O_3) counterparts. Wear tests were carried out at ambient temperature under a unidirectional rotation configuration and dry non-conformal contact using a pin-on-disc Tribometer (CSM Instruments SA, Peseux, Switzerland). The data (tangential force) for the COF evolution was directly acquired during the test using software TriboX 2.7. The system was calibrated and test conditions were set according to ASTM G99-17 [45] to a normal force of F_n = 10 N, a linear speed of v = 15 cm/s, wear track radius of r = 3 mm, sliding distance of s = 500 m and an acquisition rate of f = 10 Hz. The stop conditions for the test time t (t ~ 55 min) corresponding to the total amount of laps l (l ~ 26500 laps) were defined with respect to the following criteria of coating breakthrough and reaching COF's steady condition. At least 3 test repetitions for each state were performed for statistics and test reproducibility. The topography of the whole wear track of each tested sample was analysed and evaluated in detail by means of CLSM. Wear volumes $V_{w,\ ring,\ measured}$ have been directly measured by the software in reference to a zero-point and compared with the calculated values $V_{w,\ ring,\ calculated}$ determined using a mathematical approach according to ASTM G99-17 [45]. Mass losses of the respective samples were measured using a digital precision balance with a resolution of 0.1 µg. The respective counterparts wear volumes $V_{w,\ pin,\ calculated}$ were calculated according to ASTM G99-17 [45] and to Burris [46] by considering the diameters of the counterpart wear tracks at the spherical end. Wear rates of the samples were calculated according to the relation $k_{disc} = V_{w,\ ring}/(F_n \bullet s)$ [$mm^3/(Nm)$] and that of the counterparts according to the relation $k_{pin} = V_{w,\ pin}/(F_n \bullet s)$ [$mm^3/(Nm)$]. Errors of calculated k-values and for medium COF are equal to the respective standard deviation. The morphology and the chemical composition of the resulting wear tracks were investigated and analysed by means of CLSM/ laser reflection data image (LRDI) and SEM/BSE with EDX.

2.5. Solid particle erosion

Solid particle erosion (SPE) behaviour was conducted using an in-house developed air jet erosion testing rig. The development, commissioning and calibration of the testing rig were done in accordance with ASTM G76-18 [47]. Tests performed in this study were carried out using control variables for testing both reference and coating materials, which were, concerning the criteria coating breakthrough, empirically adapted and defined as best fit to $v_{air}(\Delta p_{air})$ = 108 m/s, $\dot{m}_{Ep}$ = 5 g/min, φ = 30° / 90° and t = 20 min (see Table 3). Two different impact angles were selected to correlate the material and its surface properties with the corresponding erosion behaviour according to Hutching [48]. At least 3 test repetitions were done for the initial state (0 h) and final state (1200 h) and at least 1 repetition for the other oxidation states of both tested materials. The errors are equal to the respective standard deviation. Mass loss Δm was determined at t = 5 min intervals in between the testing time t by a digital precision balance. The respective wear volume $V_{w, SPE}$ at t = 20 min of a sample was measured by means of CLSM using 3D-data images as colour coded surface profile images (CCSPI), as shown in Fig. 2.

3. Results and discussion

3.1. *Materials characterisation*

Cross sectional illustrations of CoNiCrAlY coatings presented in Fig. 3(a) and (b) display the averaged thickness value as well as the developed microstructure in the final state, which did not exhibit any significant above mentioned inhomogeneities. Coating characteristics can be classified in different zones [22,23], which are typically considered towards the substrate as Thermally Grown Oxide (TGO) zone, Outer-β-Depletion Zone (OBDZ), β-Rich Zone (BRZ), Inner-β-Depletion Zone (IBDZ) and Interdiffusion Zone (IDZ). In the initial state, coating exhibited a homogenous distributed BRZ microstructure. According to XRD analysis performed in the BRZ and shown in Fig. 11(a), microstructure is composed of a mixture of γ-Ni(Cr, Co) fcc solid solution, γ′-$(Ni, Co)_3Al$ fcc and β-(Ni, Co)Al bcc brittle intermetallic phases. The TGO displayed in the BSE micrographs with EDX-mapping from Fig. 5 associated with the XRD pattern from Fig. 11(a) confirms that the around 7 µm thick oxide scale grown in final state mostly consists of stable α-Al_2O_3 beside local structures composed of Cr, Ni, Co oxides, which must derive from the materials very early oxidation stages. The distribution on surface, morphology and chemical composition of these structures are indicated in Fig. 9. Additionally, XRD pattern obtained at coating's surface, emphasizes the presence of $YAlO_3$ in rather small concentrations of precipitated particles as a typical phase in TGO [2,21,36,49]. Regarding the black spots illustrated in the micrographs in Fig. 5 and Fig. 7 and marked with a black arrow, internal Al oxides can be found preferentially along splat boundary regions. However, Al-rich oxide stringers could be likewise identified in the initial state, which can be formed during deposition period [26]. An increase of formation of a new Cr rich phase has been observed within the coating after prolonged dwell time (Fig. 5 and Fig. 7). It is described that coatings with a high concentration of Co supress a phase transformation during cooling to undesired brittle but stable α-Cr (γ+β to α+γ′) at temperatures 1000°C and above [2,17,25]. Therefore, at 900°C, little amounts of α-Cr might precipitate within coating's microstructure [20], indicated by green arrows in Fig. 5 and Fig. 7. These precipitates can be also located at BRZ NiAl rich β-phase [17,50] and are, however, difficult to distinguish due to low contrast in BSE micrographs. Co additionally promotes the formation of σ-(Co, Cr) phase, which can occur in slightly higher quantities than α-Cr [25] (see XRD pattern in Fig. 11(a)). However, σ-phase is reported to be instable at temperatures above 880°C and disappearance of this phase favours to increase the amount of α-Cr-phases [17,51]. An EDX-linescan shown in Fig. 8(a) was performed at the interface region to highlight the difference in materials chemical composition. According to XRD pattern in Fig. 11(b), substrate's bulk material is composed of similar phases, which are regarded as solid-solution strengthening γ-Ni(Cr, Co) primary phase and precipitation hardening γ'-$(Ni, Co)_3(Al, Ti)$ phase. The IDZ extends both in the substrate and in the coating. For a better delimitation of the areas, the zone extending from the interface into the coating is regarded as IBDZ in this study. Likewise OBDZ, γ(/γ') containing IBDZ expands during the heat exposure due to β-phase depletion. Since coating is characterized by a higher Al content, Al containing β-phase depleted due to Al diffusion towards IDZ, which is emphasised by EDX-maps shown in Fig. 7 and confirmed by EDX-linescan shown in Fig. 8 (compare Al profiles). Oxidation of Al, which can derive from coating's (β-NiAl) or substrate's (γ'-Ni_3Al) decomposed [16] Al rich phases, could be also observed at the interface (white arrow in Fig. 7). This results in formation of a protective layer, comparable to the coating's outer Al_2O_3 rich oxide scale, which prevents oxidation of the substrate. The angular Al-rich structures located at the interface region marked with a grey arrow in Fig. 7, are probable due to surface pre-treatment with alumina. At IDZ, local formation of rather deleterious [25] α-Cr-phases (green arrow in Fig. 7 and Fig. 8(b)) and σ-phase (purple arrows in Fig. 7) were observed, which might be likewise associated to Co diffusion into the substrate (compare Co profiles in Fig. 8). The decrease of Cr profile in IDZ can be attributed to precipitation of α-Cr. On the other hand, substrate's γ'-phase might decompose at 900 °C [7,51], which is also promoted by Co [17]. This could explain the increase of coexistence of γ-and σ-phases, a higher local Ni concentration in the IDZ (blue arrows in Fig. 7 and Fig. 8(b)) and a higher Ni concentration in coating's matrix due to diffusion, especially into IBDZ (compare Ni profiles in Fig. 8). The morphology of the oxide scale grown on the uncoated substrate can be classified according to Fig. 4(a) and (b). in an External Oxidation Zone (EOZ) and an Internal Oxidation Zone (IOZ). Fig. 10 emphasises the distribution and the morphology together with the chemical composition of the differently grown oxide structures on the substrate surface. As shown in Fig. 6 and confirmed by XRD analysis on EOZ according to Fig. 11(b), formations such as Co_3O_4, NiO, $NiCr_2O_4$ and TiO_2 could be detected. These are attached to the Cr_2O_3 containing sub-scale, whose arrangement is theoretically based on the Ellingham diagram [52]. In contrast to the coating, substrate contains little amount of Ti. Although Ti benefits material mechanical properties, it promotes the formation of a relative thick and fast growing Cr_2O_3-scale [13] and at the same time it might deteriorate its adherence [6]. Substrate's EOZ growing rates are higher compared to coating's TGO growing rates [1], which results in an almost 25 µm thick grown oxide scale. Regarding substrate's IOZ, an internal growth of different oxide structures could be observed along the grain boundaries. BSE micrograph in Fig. 6 emphasizes, the average grain size is estimated to be approximately 30 µm, typically expected of this Ni based alloy [8,42]. Fig. 6 shows Ti and Al rich oxides formed along substrate's sub-surface grain boundaries as acicular intergranular penetrations, which are typically comprised of TiO_2 and Al_2O_3 [13]. Consequently, a presumable decomposition of superalloys strengthening γ'-phase, formation of other phases [13,16] and the observed internal oxide formations at the sub-surface region can deteriorate the original mechanical properties at the substrate surface.

3.2. Vickers microhardness

In Fig. 12, selected positions of the microhardness profile measurements of the coated samples are shown for each state. It illustrates the characteristic local microstructures and corresponding indentations dimensions. The difference between each *dx* and *dy* and the standard deviation of at least 5 calculated hardness values was determined to be < 5 % per position. The averaged Vickers hardness results are presented in Fig. 13 as microhardness profiles. Regarding substrate's measured hardness values towards the interface, the initial state exhibits the lowest values, typical of softened and precipitation hardenable NiCrCoTi sheet [8,53]. Heat exposure for 10 h and slowly cooling, which can be regarded as a process of precipitation annealing, causes increase of substrate's strength and hardness values. This is associated with precipitation of coherent γ'-phases within γ-matrix [8]. Increasing dwell times up to 1200 h for the oxidation procedure led to a continuous slight decrease of hardness values. Alteration in hardness values in bulk material can be referred to substrate's peak hardening effect, which classifies the substrate to attain highest hardness values after 8-10 h of heat exposure under set conditions [8]. The values of the bulk material remain relatively constant towards the interface to a distance of almost 75 µm. Closer to the interface at IDZ, hardness values of each state rapidly increase, mainly due to blasting hardening during the substrate preparation, which led to plastic deformation, strain hardening and compressive stresses in substrate’s surface [11]. Heat exposure might have relaxed the stresses [20]. The results mean variation and the measurements uncertainty increase in this zone. This can be explained by the change in microstructure and its properties due to diffusion, indicated with purple, blue and green arrows in Fig. 7 and in Fig. 12 considering the fifth and the final states. Indentations performed directly at the interface were done to investigate the coating adhesion onto the substrate. No microcracks could be observed in any state, which might conclude consistent or even improved adhesion properties [9,39,54]. Regarding the coating, a comparable higher alteration in hardness values (Fig. 13) with increasing dwell time of oxidation could be observed. Similar to IDZ, coating’s microstructures and inhomogeneities have an impact on the local hardness values, resulting in higher values mean variation, compared to substrate’s bulk material. It must be noted, that test method and conditions significantly influence the obtained hardness values, which explain controversially reported hardness values for CoNiCrAlY coatings [27,36,39,50]. In the initial state, higher hardness values at IBDZ may be attributed to work hardening during coating’s HVOF-deposition. However, IBDZ in other states are affected by stress relief and elements diffusion. A relative consistent average hardness values for each state could be explained by a counteraction effect, attributed to increased formation of oxide stringers, indicated with black arrows in Fig. 5, Fig. 7 and Fig. 12. for the final state. Oxide stringer are brittle phases that can be regarded as obstacles to dislocation motion, while performing indentations on the material. Furthermore, as it can be observed in Fig. 12, coarsening of β-phase [23], which can also lead to a reduction of obstacles to dislocation motions, has a minor effect on hardness.

3.3. Sliding wear behaviour

Sliding wear test parameters were set empirically to ensure just the wear of the coating without mitigating the underlaying substrate. CCSPI illustrations with color coding in the relevant depth range according to Fig. 14 demonstrate, the substrate was not reached at the end of all performed tests. Corresponding LRDIs of the respective counterpart wear dimensions are strongly related to samples wear profiles. However, transferred metallic material from the samples accounts to increase the shapes dimension, which is indicated in Fig. 14 with a purple and blue arrow, respectively. The more oxides prevailed on materials surface and the thicker TGO or EOZ were developed (compare Fig. 3(a) and Fig. 4(a)), smaller wear profiles and the less material transfer could be observed. Since the oxide scale grown on the substrate was substantially thicker than that grown on the coating, this might contribute to substrate's smaller wear degree. Furthermore, profile measurements shown in Fig. 14 at the final states indicate different wear depths after the test for both materials. Since coating's final wear depth was measured to be around 80 µm in respect to the zero-point on the surface, coating's corresponding wear behaviour must be a response to the mechanical properties [26] of developed TGO, OBDZ and BRZ (see Fig. 3). Although coating's wear depth is observed to be the highest at the third and fourth states (see colour coding in Fig. 14), IBDZ and IDZ are comparable to that of the final state very little developed in order to have a significant influence on the wear degree. In contrast, substrate's final states wear depth was measured to be around 20 µm. As shown in Fig. 4, EOZ extends almost 25 µm and this implies wear to be limited to EOZ. The more EOZ grows due to heat exposure, the less wear might be expected in comparison to the initial state. However, this can only be concluded regarding experiments performed according to the present conditions. The quantitative results for averaged wear rates for every materials state with the corresponding counterparts wear rates are illustrated in Fig. 18(a) and Fig. 18(b), respectively. Averaged materials mass losses are shown in Table 4. As indicated in Fig. 15(a) and marked with black arrows, coating is mainly mitigated by ductile abrasion wear at the initial state, associated with plough grooves [36]. At higher magnification, marked with white arrows, plastic deformation as well as adhesion were visible, referred to adhesive wear and associated with fracture, delamination and plastic extrusion of lips [26]. Changes in coating's local microstructure and chemical composition can explain a slight increase of the wear degree towards the forth state [55]. However, considering the fifth and the final states, a higher content of ceramic phases might have contributed to slightly improve coating's wear degree. Most of the former oxide scale was delaminated and removed. Remaining local oxides in the form of larger flakes could be observed at the surface of the final state, which appear as dark shaped wear debris in Fig. 15(b) both in LRDI and BSE. The formations could be attributed to plastic deformation associated with adhesive wear, which behaved either as two- or three-body abradants [20,56]. Beside small amount of Al oxides (Spot 1), mostly Cr- and Co-rich oxides (Spot 2) could be detected as residues, locally attached and smeared on the worn metallic coating (Spot 3). During the wear process, these oxide debris could sinter and form local solid tribofilms. However, internal oxides after coating deposition could not promote a continuous and a dense tribofilm with beneficial effects of a glaze-layer, since layer regrowth is not expected significantly during the test. However, no major changes in the wear process and thus wear rates could be observed for the coating (see Fig. 18(a)), since abrasive wear is assumed to prevail as dominant mechanism and no dense glaze-layer was observed to develop. Relatively high wear rates can be furthermore associated with materials transfer from coating to the counterpart (Fig. 14, purple arrow). Comparable to the coating's surface, in the first and second states, substrate's metallic surface underwent severe abrasive and adhesive wear, indicated in Fig. 16(a) with black and white arrows, respectively. Substrate's low hardness (Fig. 13) in the initial state might contributed to increase the wear rate due to microcutting [12,35]. Beneficial effect of an oxide layer could be already observed on tested samples of the third state (see Fig. 18(b)). The longer tested samples were previously set to oxidation, the more oxide could growth, which can be associated with a decrease of wear [57]. As shown in Fig. 16(b) for the final state, almost whole substrate's surface was covered with a dark coloured and smooth layer. An intrusion of the counterpart that removes the oxide layer was not observed. In contrast to the coating, previous substrate's oxidation resulted in a formation of a well adjacent oxide layer comparable to a glaze-layer, usually observed to grow during high temperature wear tests [27,40]. Taking the different grey scales between LRDI and BSE micrograph in Fig. 16(b) into account, it must be noted, that LRDI grey scale distribution is attributed to different laser intensities and reflection angles, dependent of topographies structure. As indicated in Fig. 16(b), the layer predominantly consists of Cr-oxides (Spot 1), which are dominant in present oxide scale (Fig. 6). However, metallic phases (Spot 2) could be also detected on the surface, which indicate a degradation and local breakthrough through the layer. Remaining layer was rather compacted and smeared into substrate surface, while at the same time preventing the surface to suffer from cutting effects due to abrasive wear, mainly attributed to Cr oxides [11,57,58]. Adhesive wear prevailed as the major mechanism as indicated with white arrows in Fig. 16(a). In contrast to the first and second states (see blue arrow in Fig. 14), only little material transfer could be detected on the counterparts, as indicated with green arrow in Fig. 14. A continuous predominantly oxide to oxide contact between sample and counterpart might have been achieved during the tests, so wear rates for the substrate and counterpart were greatly reduced. Wear decreased by almost one order of magnitude for the substrate and by two orders of magnitude for the counterpart. Averaged COF evolutions of all material states are presented in Fig. 17(a) and Fig. 17(b), whereas the quantitative results of averaged medium COF are shown in Fig. 18(a) and Fig. 18(b), respectively. As shown in Fig. 17(a), in every coating's state, recorded tribosystem's COF profiles oscillated during the test, which reached quickly steady conditions. A continuous superposition of abrasive and adhesive wear might be one reason, whereas adhesive wear can be associated with stick-slip phenomena [26] by increasing the COF values to climax points. Both mechanisms contribute to the wear degree by plastic deformation and a sudden loss of material by abrasion and pull-out effect, which can change local topography, chemical composition and therefore COFs evolution rates. In the final state, COF decreased at around the half of the test duration. It can be presumed, the smeared oxide layer must have been delaminated and removed at this point, resulting in a predominantly worn metallic surface (Fig. 15(b)). Regarding Fig. 17(b), substrate's initial and second states exhibited likewise an oscillating COF. It increased in the other states due to higher contribution of adhesive wear, which is at the same time correlated with the presence of ceramic oxide phases in the system. Likewise, COF evolution stabilised towards the final state, since the adhesive wear mechanism got dominant. However, mentioned oxide to oxide contact was not observed during tests at ambient temperature to contribute to a low COF [11]. Highest tangential forces and thus obtained COF resulted in observed layers with undulating shape (Fig. 16(b)).

3.4. Solid particle erosion behaviour

CCSPI illustrations of the erosion scars geometry [29] on the respective material at the end of the test are shown in Fig. 19. Since coating's breakthrough was not observed in any case within preliminary investigations, CCSPI colour coding was set in a narrower range, in order to distinguish the fine depth differences due to material removal. The maximum erosion depth was measured to be within BRZ for the coating and deeper than IOZ for the substrate, respectively. Due to the set colour coding, a certain trend concerning materials SPE behaviour could be observed. Measured wear volumes indicated in Table 5, which correspond to the illustrations in Fig. 19, are determined to increase at both impact angles towards the final state. As exception, an opposite behaviour could be only observed regarding the coating, tested at an impact angle of 30°. Likewise, independent mass loss measurements confirmed the in Fig. 19 illustrated trend in materials behaviour toward the respective material final state. Materials quantitative results for measured and averaged mass loss during SPE tests performed at an impact angle of 30° and 90° are shown in Fig. 20 and Fig. 21, respectively. As shown in Fig. 19 and Fig. 20(a) for the initial state, subjected to impact wear at 30°, a relative high wear volume and mass loss have been measured, which could be attributed to ductile erosion mechanism [59]. As indicated by colour coding in Fig. 19, IDZ is not supposed be participated in SPE process, otherwise IDZs lower microhardness values were expected to have a greater impact on mass loss rates. Furthermore, increasing amount of external and internal oxide formations increased coating's ceramic phase ratio. Consequently, this could lead to a change from ductile to brittle SPE response and thus counteract ductile erosion, especially during the initial testing time. This explanation can be likewise transferred to measured mass losses, presented in Fig. 20(a). In contrast to coating's initial state, the final state exhibits a flatter mass loss rate during the first 5 min of SPE exposure, which can be contributed to a brittle character of a well adjacent oxide scale, slightly mitigating effects of ductile erosion. Despite of measurement uncertainties, mass loss evolution >5 min runs largely parallel to each other, indicating coating's identical long term SPE behaviour, independently from dwell time of previous performed oxidation procedure. Considering substrate's erosion wear volume (Fig. 19) and mass loss evolution (Fig. 20(b)), a different erosion behaviour could be observed for the states 100 h and longer of previous heat exposure. However, subjected to an impact angle of 30°, similar to coating's mass loss rates of the initial and second states might be likewise associated with ductile phase compositions at the surfaces. 10 h previous heat exposure had a slight effect on the measured mass loss since values decreased, which could be in this case, attributed to a change in substrate's hardness. For the other states, materials detriment due to oxidation gets significantly obvious. Substrate's thicker grown oxide scale was primely removed. IOZ was observed to expand the longer the material was exposed to temperature. Since IOZs were previously described to have poor mechanical properties, greater volumes of IOZ might have been removed towards the final state. EOZ and IOZ of each state seem to be removed during a testing time < 5 min, which can be related to parallel mass loss evolutions during testing time > 5 min and therefore to identical SPE behaviour. Erosion scars of each state were measured to be deeper than 50 µm after the test (Fig. 19), which confirms a certain removal of both zones and a further attack of substrate's bulk material. Regarding coating's SPE behaviour tested at an impact angle of 90° (see Fig. 19 and Fig. 21(a)), the effect of brittle erosion on a ductile material gets obvious. Coating at the initial state exhibited a comparable low and constant erosion rate, attributed to the ability of plastic deformation. Towards coating's final state, incline in mass loss rate was observed to be the highest during testing time < 5 min. Increased mass loss rate during testing time < 5 min and slight difference in incline rates during testing time > 5 min can be likewise associated with increasing amount of ceramic and brittle phases, changes in coating's microstructures and chemical compositions at the surface. However, heat exposed coatings exhibited higher mass losses and erosion rates, frequently observed during brittle erosion [28]. Substrate's SPE response at an impact angle of 90° was observed to follow a similar trend to results, obtained at impact angle of 30° (Fig. 21(b) and Fig. 20(b)). For the first both states, slightly higher erosion rates compared to the coating can be attributed to substrate's mechanical properties, since coating's microstructure properties are associated with more ductile behaviour [29]. Greater developed EOZ and IOZ were responsible for higher mass losses under brittle erosion.

4. Conclusions

For this study, CoNiCrAlY coatings were deposited by means of HVOF on NiCrCoTi substrate, which was selected as reference materials for the exposure to isothermal oxidation up to 1200 h at 900 °C. Microstructural investigations shown that the materials exhibited a typical diffusion-controlled microstructure and oxide scales. In comparison to the uncoated substrate, the coating exhibited a better oxidation behaviour and thus a better protection to the underlaying substrate from oxidation and deterioration. Coating’s microhardness was measured to be higher than that of the substrate in any oxidation state. Significant changes in microhardness profiles were mainly observed at the interface region of the substrate/coating system, which were associated with interdiffusion. Materials hardness is supposed to have a minor effect on sliding wear and solid particle erosion behaviour. Temperature and dwell time related changes in microstructure and chemical composition were mainly attributed to have a significant influence on the obtained results. Sliding wear rates of materials initial states were calculated to settle at same order of magnitude. Towards the respective finale states, coating’s sliding wear rates did not deviate significantly, whereas substrate’s sliding wear rates decreased. Substrate’s thicker grown oxide is discussed to mitigate sliding wear, which could, however, not be certainly observed considering the coating’s behaviour at final state. Corresponding coefficient of friction increased with increasing the oxidation time, which could be attributed to a higher content of the ceramic phases. Contrary, solid particle erosion was mainly associated with material removal. Both materials suffer higher erosion wear subjected to an impact angle of 30° due to ductile wear mechanism. Grown oxide scales were not observed to have a strong beneficial influence on the erosion wear resistance, independently of the applied impact angle. However, an interrelation and interdependency between microstructures properties, chemical composition and materials removal could be presented. Supplementary nanoindentation tests will be considered for further studies to allow better correlation of materials microstructure and properties with observed sliding wear and solid particle erosion behaviour.

Acknowledgements

The authors would like to thank to Prof. Robert Vaßen for the HVOF coating deposition at Forschungszentrum Jülich GmbH, IEK-1, Jülich, Germany and to Prof. Gunther Eggeler for the SEM/EDX investigations performed at the Chair for Materials Science and Engineering of Ruhr-Universität Bochum, Germany.

Funding sources

The present research was funded by the Westphalian University of Applied Sciences Gelsenkirchen Bocholt Recklinghausen.

References

[1] C.U. Hardwicke, Y.-C. Lau, Advances in Thermal Spray Coatings for Gas Turbines and Energy Generation: A Review, J Therm Spray Tech. 22 (2013) 564–576. https://doi.org/10.1007/s11666-013-9904-0.

[2] W.G. Sloof, Nijdam T. J., On the high-temperature oxidation of MCrAlY coatings, International Journal of Materials Research. 100 (2009) 1318–1330. https://doi.org/10.3139/146.110201.

[3] R. Rajendran, Gas turbine coatings – An overview, Engineering Failure Analysis. 26 (2012) 355–369. https://doi.org/10.1016/j.engfailanal.2012.07.007.

[4] G.W. Goward, Progress in coatings for gas turbine airfoils, Surface and Coatings Technology. 108-109 (1998) 73–79. https://doi.org/10.1016/S0257-8972(98)00667-7.

[5] N.D. Prasanna, C. Siddaraju, G. Shetty, M.R. Ramesh, M. Reddy, Studies on the role of HVOF coatings to combat erosion in turbine alloys, Materials Today: Proceedings. 5 (2018) 3130–3136. https://doi.org/10.1016/j.matpr.2018.01.119.

[6] S. Bose, High temperature coatings, Second edition ed., Butterworth-Heinemann an imprint of Elsevier, Kidlington, Cambridge, MA, 2018.

[7] F. Vogel, N. Wanderka, S. Matsumura, J. Banhart, Early stages of decomposition within the γ' phase of a Ni–Al–Ti model alloy, Intermetallics. 22 (2012) 226–230. https://doi.org/10.1016/j.intermet.2011.11.011.

[8] A. Venkateswarlu, V. Sharma, L. Krishna, Evaluation of and Fracture Behavior of Alloy 90 Sheets, IOSR-JMCE. 6 (2013) 52–66. https://doi.org/10.9790/1684-0625266.

[9] P. Poza, P.S. Grant, Microstructure evolution of vacuum plasma sprayed CoNiCrAlY coatings after heat treatment and isothermal oxidation, Surface and Coatings Technology. 201 (2006) 2887–2896. https://doi.org/10.1016/j.surfcoat.2006.06.001.

[10] M. Roy, Approaches to enhance elevated temperature erosion resistance of Ni-base superalloys, Materials at High Temperatures. 36 (2019) 142–156. https://doi.org/10.1080/09603409.2018.1482077.

[11] S. Sun, L. Li, C. Hu, Q. Li, T. Yuan, Tribological Behavior of a Shot-Peened Nickel-Based Single Crystal Superalloy at High Temperature, Tribol Lett. 70 (2022) 1–13. https://doi.org/10.1007/s11249-022-01637-9.

[12] J.H. Ramírez-Ramírez, J. Manuel Alvarado-Orozco, F.A. Pérez-González, R. Colás, N.F. Garza-Montes-de-Oca, Influence of Heat Treatment on the Wear Behavior of a Haynes 282® Nickel-Based Superalloy, Journal of Tribology. 141 (2019). https://doi.org/10.1115/1.4042274.

[13] S. Cruchley, H. Evans, M. Taylor, An overview of the oxidation of Ni-based superalloys for turbine disc applications: surface condition, applied load and mechanical performance, Materials at High Temperatures. 33 (2016) 465–475. https://doi.org/10.1080/09603409.2016.1171952.

[14] A. Zakeri, E. Bahmani, A. Sabour Rouh Aghdam, B. Saeedi, M. Bai, A study on the effect of nano-CeO2 dispersion on the characteristics of thermally-grown oxide (TGO) formed on NiCoCrAlY powders and coatings during isothermal oxidation, Journal of Alloys and Compounds. 835 (2020) 155319. https://doi.org/10.1016/j.jallcom.2020.155319.

[15] Z. Esmaeili, M.R. Loghman-Estarki, M. Ramezani, M. Naderi, E. Mohammad Sharifi, Toward hardening of NiCrAlY alloy by spark plasma sintering of NiCrAlY-nanoSi3N4-graphite nanocomposite, Journal of Alloys and Compounds. 847 (2020) 155802. https://doi.org/10.1016/j.jallcom.2020.155802.

[16] Y.Z. Liu, X.B. Hu, S.J. Zheng, Y.L. Zhu, H. Wei, X.L. Ma, Microstructural evolution of the interface between NiCrAlY coating and superalloy during isothermal oxidation, Materials & Design. 80 (2015) 63–69. https://doi.org/10.1016/j.matdes.2015.05.014.

[17] J. Toscano, A. Gil, T. Hüttel, E. Wessel, D. Naumenko, L. Singheiser, W.J. Quadakkers, Temperature dependence of phase relationships in different types of MCrAlY-coatings, Surface and Coatings Technology. 202 (2007) 603–607. https://doi.org/10.1016/j.surfcoat.2007.06.044.

[18] F. Ghadami, A. Sabour Rouh Aghdam, S. Ghadami, A comprehensive study on the microstructure evolution and oxidation resistance of conventional and nanocrystalline MCrAlY coatings, Scientific reports. 11 (2021) 875. https://doi.org/10.1038/s41598-020-79323-w.

[19] Y. Chen, X. Zhao, P. Xiao, Effect of microstructure on early oxidation of MCrAlY coatings, Acta Materialia. 159 (2018) 150–162. https://doi.org/10.1016/j.actamat.2018.08.018.

[20] A. Zakeri, E. Bahmani, A. Ramazani, A Review on the Enhancement of Mechanical and Tribological Properties of MCrAlY Coatings Reinforced by Dispersed Micro and Nanoparticles, Energies. 15 (2022) 1914. https://doi.org/10.3390/en15051914.

[21] K. Yuan, R. Lin Peng, X.-H. Li, S. Johansson, Y.-D. Wang, Some aspects of elemental behaviour in HVOF MCrAlY coatings in high-temperature oxidation, Surface and

Coatings Technology. 261 (2015) 86–101. https://doi.org/10.1016/j.surfcoat.2014.11.053.

[22] L. Yang, M. Chen, J. Wang, Y. Qiao, P. Guo, S. Zhu, F. Wang, Microstructure and composition evolution of a single-crystal superalloy caused by elements interdiffusion with an overlay NiCrAlY coating on oxidation, Journal of Materials Science & Technology. 45 (2020) 49–58. https://doi.org/10.1016/j.jmst.2019.11.017.

[23] W.-X. Weng, Y.-M. Wang, Y.-M. Liao, C.-C. Li, Q. Li, Comparison of microstructural evolution and oxidation behaviour of NiCoCrAlY and CoNiCrAlY as bond coats used for thermal barrier coatings, Surface and Coatings Technology. 352 (2018) 285–294. https://doi.org/10.1016/j.surfcoat.2018.08.024.

[24] H. Chen, T.H. Hyde, Use of multi-step loading small punch test to investigate the ductile-to-brittle transition behaviour of a thermally sprayed CoNiCrAlY coating, Materials Science and Engineering: A. 680 (2017) 203–209. https://doi.org/10.1016/j.msea.2016.10.097.

[25] D.R.G. Achar, R. Munoz-Arroyo, L. Singheiser, W.J. Quadakkers, Modelling of phase equilibria in MCrAlY coating systems, Surface and Coatings Technology. 187 (2004) 272–283. https://doi.org/10.1016/j.surfcoat.2004.02.018.

[26] G. Bolelli, A. Candeli, L. Lusvarghi, A. Ravaux, K. Cazes, A. Denoirjean, S. Valette, C. Chazelas, E. Meillot, L. Bianchi, Tribology of NiCrAlY+Al2O3 composite coatings by plasma spraying with hybrid feeding of dry powder+suspension, Wear. 344-345 (2015) 69–85. https://doi.org/10.1016/j.wear.2015.10.014.

[27] G. Bolelli, C. Vorkötter, L. Lusvarghi, S. Morelli, V. Testa, R. Vaßen, Performance of wear resistant MCrAlY coatings with oxide dispersion strengthening, Wear. 444-445 (2020) 203116. https://doi.org/10.1016/j.wear.2019.203116.

[28] H.S. Nithin, V. Desai, M.R. Ramesh, Elevated temperature solid particle erosion behaviour of carbide reinforced CoCrAlY composite coatings, Mater. Res. Express. 5 (2018) 66529. https://doi.org/10.1088/2053-1591/aac998.

[29] E. Bousser, L. Martinu, J.E. Klemberg-Sapieha, Solid particle erosion mechanisms of protective coatings for aerospace applications, Surface and Coatings Technology. 257 (2014) 165–181. https://doi.org/10.1016/j.surfcoat.2014.08.037.

[30] F. Cernuschi, C. Guardamagna, S. Capelli, L. Lorenzoni, D.E. Mack, A. Moscatelli, Solid particle erosion of standard and advanced thermal barrier coatings, Wear. 348-349 (2016) 43–51. https://doi.org/10.1016/j.wear.2015.10.021.

[31] O. Gohardani, Impact of erosion testing aspects on current and future flight conditions, Progress in Aerospace Sciences. 47 (2011) 280–303. https://doi.org/10.1016/j.paerosci.2011.04.001.

[32] S. Hanumanthlal, C. Siddaraju, M.R. Ramesh, High-Temperature Solid-Particle Erosion Behaviour of Plasma-Sprayed Fe17Cr2Ni0.18C/Cenosphere-Based Composite Coating, J Bio Tribo Corros. 7 (2021). https://doi.org/10.1007/s40735-021-00503-w.

[33] J. Alqallaf, N. Ali, J.A. Teixeira, A. Addali, Solid Particle Erosion Behaviour and Protective Coatings for Gas Turbine Compressor Blades—A Review, Processes. 8 (2020) 984. https://doi.org/10.3390/pr8080984.

[34] AZO Materials, Abradable Coatings Increase Gas Turbine Engine Efficiency. https://www.azom.com/article.aspx?articleid=739, 2022 (accessed 17 September 2022).

[35] Y. Yanliang, L. Shaolei, Z. Rui, W. Changyi, Z. Shengfeng, Influence of Al2O3 particles on the tribological properties of CoCrAlYTa coating produced by laser-induction hybrid cladding, Ceramics International. 47 (2021) 19434–19442. https://doi.org/10.1016/j.ceramint.2021.03.280.

[36] J. Pereira, J. Zambrano, M. Licausi, M. Tobar, V. Amigó, Tribology and high temperature friction wear behavior of MCrAlY laser cladding coatings on stainless steel, Wear. 330-331 (2015) 280–287. https://doi.org/10.1016/j.wear.2015.01.048.

[37] H. Vasudev, L. Thakur, H. Singh, A. Bansal, Effect of addition of Al2O3 on the high-temperature solid particle erosion behaviour of HVOF sprayed Inconel-718 coatings, Materials Today Communications. 30 (2022) 103017. https://doi.org/10.1016/j.mtcomm.2021.103017.

[38] G. Hou, Y. An, X. Zhao, H. Zhou, J. Chen, Effect of alumina dispersion on oxidation behavior as well as friction and wear behavior of HVOF-sprayed CoCrAlYTaCSi coating at elevated temperature up to 1000 °C, Acta Materialia. 95 (2015) 164–175. https://doi.org/10.1016/j.actamat.2015.05.025.

[39] M. Szala, M. Walczak, A. Świetlicki, Effect of Microstructure and Hardness on Cavitation Erosion and Dry Sliding Wear of HVOF Deposited CoNiCrAlY, NiCoCrAlY and NiCrMoNbTa Coatings, Materials (Basel, Switzerland). 15 (2021). https://doi.org/10.3390/ma15010093.

[40] F.H. Stott, D.S. Lin, G.C. Wood, The structure and mechanism of formation of the 'glaze' oxide layers produced on nickel-based alloys during wear at high temperatures, Corrosion Science. 13 (1973) 449–469. https://doi.org/10.1016/0010-938X(73)90030-9.

[41] L. Li, K. He, S. Sun, W. Yang, Z. Yue, H. Wan, High-Temperature Friction and Wear Features of Nickel-Based Single Crystal Superalloy, Tribol Lett. 68 (2020) 1–12. https://doi.org/10.1007/s11249-020-1266-4.

[42] G. Khajuria, M.F. Wani, High-Temperature Friction and Wear Studies of Nimonic 80A and Nimonic 90 Against Nimonic 75 Under Dry Sliding Conditions, Tribol Lett. 65 (2017) 1–26. https://doi.org/10.1007/s11249-017-0881-1.

[43] W. Wen, G.A. Jackson, H. Li, W. Sun, An experimental and numerical study of a CoNiCrAlY coating using miniature specimen testing techniques, International Journal of Mechanical Sciences. 157-158 (2019) 348–356. https://doi.org/10.1016/j.ijmecsci.2019.04.001.

[44] ASTM Standard E384-17, Test Method for Microindentation Hardness of Materials, E04 Committee, ASTM International, West Conshohocken, PA. 2017. https://doi.org/10.1520/E0384-17.

[45] ASTM Standard G99-17, Test Method for Wear Testing with a Pin-on-Disk Apparatus, G02 Committee, ASTM International, West Conshohocken, PA. 2017. https://doi.org/10.1520/G0099-17.

[46] D.L. Burris, W.G. Sawyer, Measurement Uncertainties in Wear Rates, Tribol Lett. 36 (2009) 81–87. https://doi.org/10.1007/s11249-009-9477-8.

[47] ASTM Standard G76-18, Test Method for Conducting Erosion Tests by Solid Particle Impingement Using Gas Jets, G02 Committee, ASTM International, West Conshohocken, PA. 2018. https://doi.org/10.1520/G0076-18.

[48] I.M. Hutchings, Tribology: Friction and wear of engineering materials, Repr ed., Metallurgy and materials science series, Butterworth-Heinemann, Oxford, 2001.

[49] A. Gil, V. Shemet, R. Vassen, M. Subanovic, J. Toscano, D. Naumenko, L. Singheiser, W.J. Quadakkers, Effect of surface condition on the oxidation behaviour of MCrAlY coatings, Surface and Coatings Technology. 201 (2006) 3824–3828. https://doi.org/10.1016/j.surfcoat.2006.07.252.

[50] S. Saeidi, K.T. Voisey, D.G. McCartney, Mechanical Properties and Microstructure of VPS and HVOF CoNiCrAlY Coatings, J Therm Spray Tech. 20 (2011) 1231–1243. https://doi.org/10.1007/s11666-011-9666-5.

[51] D.R.G. Achar, R. Munoz-Arroyo, L. Singheiser, W.J. Quadakkers, Modelling of phase distributions in MCrAlY coatings and their interactions with nickel based alloys, J. Phys. IV France. 120 (2004) 231–238. https://doi.org/10.1051/jp4:2004120027.

[52] P. Stratton, Ellingham diagrams – their use and misuse, International Heat Treatment and Surface Engineering. 7 (2013) 70–73. https://doi.org/10.1179/1749514813Z.00000000053.

[53] HARALD PIHL GmbH, Nimonic-Alloy-90 Datasheet. https://www.haraldpihl.com/de/products/Nickellegierungen/nimonic-90/, 2022 (accessed 14 September 2022).

[54] J. Lesage, M.H. Staia, D. Chicot, C. Godoy, P.E.V. de Miranda, Effect of thermal treatments on adhesive properties of a NiCr thermal sprayed coating, Thin Solid Films. 377-378 (2000) 681–686. https://doi.org/10.1016/S0040-6090(00)01450-4.

[55] S. Li, C. Langlade, S. Fayeulle, D. Tréheux, Influence of the microstructure of plasma deposited MCrAlY coatings on their tribological behaviour, Surface and Coatings Technology. 100-101 (1998) 7–11. https://doi.org/10.1016/S0257-8972(97)00579-3.

[56] P. Seenuvasaperumal, A. Elayaperumal, R. Jayavel, Influence of calcium hexaboride reinforced magnesium composite for the mechanical and tribological behviour, Tribology International. 111 (2017) 18–25. https://doi.org/10.1016/j.triboint.2017.02.042.

[57] C. Rynio, H. Hattendorf, J. Klöwer, G. Eggeler, On the physical nature of tribolayers and wear debris after sliding wear in a superalloy/steel tribosystem at 25 and 300°C, Wear. 317 (2014) 26–38. https://doi.org/10.1016/j.wear.2014.04.022.

[58] E.G.A. Luis, A. Bedolla-Jacuinde, C.C. Eduardo, F.V. Guerra, A. Ruiz, Dry sliding wear of a Ni-based superalloy as a function of the aging time, MRS Advances. 5 (2020) 3091–3102. https://doi.org/10.1557/adv.2020.422.

[59] M. Demirci, M. Bagci, High temperature solid particle erosion comparison of atmospheric plasma sprayed MCrAlY coatings, Surf. Topogr.: Metrol. Prop. 9 (2021) 35007. https://doi.org/10.1088/2051-672X/ac1048.

[60] P.J. Terberger, Alterung von Vakuum-plasmagespritzten MCrAIY-Schutzschichten und ihre Wechselwirkung mit Nickel- und Cobalt-basierten γ/γ‘-Superlegierungen, Schriften des Forschungszentrums Jülich Reihe Energie & Umwelt, volume 301, Forschungszentrum Jülich GmbH, Zentralbibliothek, Jülich, 2015.

Tables

Table 1
Chemical compositions in weight percent from [27,60] for the powder material CoNiCrAlY (Amdry 995) and from chemical analysis for the substrate material NiCrCoTi (Nimonic 90)

Material	Co	Ni	Cr	Al	Ti	Y
Amdry 995	Bal.	34	21.3	8.39	-	0.42
Nimonic 90	15.7	Bal.	19.3	1.4	2.4	-

Table 2
Designation of the respective sample states and corresponding oxidation dwell times

Designation	Oxidation dwell time
Initial state	0 h
Second state	10 h
Third state	100 h
Fourth state	350 h
Fifth state	700 h
Final state	1200 h

Table 3
Selected test parameters and varied control variables for performing solid particle erosion tests using an in-house developed air jet erosion testing rig

Test parameters		Control variables	
Transport medium	dry air	Transport medium velocity $v_{air}(\Delta p_{air})$	75 – 200 m/s
Erodent particles (Ep)	Al_2O_3	Ep-mass flow $\dot{m}_{Ep}$	2 – 10 g/min
Ep-size	50 µm	Testing angle φ	15 – 90 °
$Ø_{Nozzle}$	1,5 ± 0,075 mm	Testing time t	5 – 20 min
Nozzle length l_N	50 mm		
Distance nozzle/sample a	10 ± 1 mm		
Test temperature T	20 – 30 °C		

Table 4
Measured and averaged sliding wear related samples mass losses of all coating’s and substrate’s states at the end of the test

	Mass loss [g]	
State	CoNiCrAlY-coating	NiCrCoTi-substrate
0 h	0.0146 ± 0.0006	0.0285 ± 0.0013
10 h	0.0183 ± 0.0003	0.0236 ± 0.0021
100 h	0.0225 ± 0.0014	0.0051 ± 0.0015
350 h	0.0221 ± 0.0022	0.0025 ± 0.0006
700 h	0.0155 ± 0.0014	0.0016 ± 0.0001
1200 h	0.0098 ± 0.0013	0.0011 ± 0.0002

Table 5
Measured and averaged solid particle erosion related samples wear volumes of all coating’s and substrate’s states at the end of the test

	Wear volume [mm³] at 30 ° impact angle		Wear volume [mm³] at 90 ° impact angle	
State	CoNiCrAlY-coating	NiCrCoTi-substrate	CoNiCrAlY-coating	NiCrCoTi-substrate
0 h	0.902 ± 0.006	0.689 ± 0.007	0.083 ± 0.009	0.194 ± 0.005
10 h	0.832	0.652	0.203	0.199
100 h	0.739	0.774	0.269	0.408
350 h	0.696	0.818	0.354	0.706
700 h	0.669	0.853	0.402	0.966
1200 h	0.649 ± 0.013	1.171 ± 0.0012	0.512 ± 0.015	1.062 ± 0.011

List of figure captions

Fig. 1. Schematic representation of indentation positions within a coated sample

Fig. 2. CLSM 3D-data image of exemplary samples significant erosion scar regions as conventional light microscope image (CLMI) and colour coded surface profile image (CCSPI), illustrating the approaches to determine the samples wear volumes induced by the erosion tests at a (a) 30 ° and (b) 90 ° testing angle

Fig. 3. Graphical indication of coating's thicknesses and substrate/coating system's microstructures characteristics. (a) Within cross-sections of each state based on averaged value, (b) determination of an averaged value exemplarily shown in laser reflection data image (LRDI) for the final state ~ 1200 h

Fig. 4. Graphical indication of substrate's microstructure characteristics. (a) Within cross-sections of each state based on averaged values, (b) determination of an averaged value exemplarily shown in LRDI for the final state ~ 1200 h

Fig. 5. SEM/BSE image and EDX-mapping of a coating's cross-section at surface region for the final state ~ 1200 h

Fig. 6. SEM/BSE image and EDX-mapping of a substrate's cross-section at surface region for the final state ~ 1200 h

Fig. 7. SEM/BSE image and EDX-mapping of a substrate/coating system's cross-section at interface region for final state ~1200 h

Fig. 8. EDX-linescan of substrate/coating system's cross-section at interface region (a) initial state ~ 0 h and (b) final state ~ 1200 h

Fig. 9. SEM/BSE micrographs of coating's surface structure and EDX spectra of local chemical compositions for the final state ~ 1200 h

Fig. 10. SEM/BSE micrographs of substrate's surface structure and EDX spectra of local chemical compositions for the final state ~ 1200 h

Fig. 11. XRD patterns attained on (a) coating's material at BRZ in the initial ~ 0 h, in third ~ 350 h and coating's surface in final ~ 1200 h states and (b) substrate's bulk material in the initial ~ 0 h, in third ~ 350 h and substrate's surface in final ~ 1200 h states

Fig. 12. CLSM/LRDI illustration of different indentation positions with an offset distance (in µm) to the substrate/coating interface, showing characteristic local microstructures and corresponding indentations dimensions for each state

Fig. 13. Vickers microhardness profiles along the substrate/coating interface for every state of the coated samples and exemplary illustration of corresponding characteristic local microstructure of coating's final state ~ 1200 h

Fig. 14. CLSM/CCSPI of whole wear tracks of all coating's and substrate's states and CLSM/LRDI of respective counterpart wear tracks at spherical end. Colour coding is set from red +40 µm to dark blue -145 µm in respect to the zero-point.

Fig. 15. LRDI and SEM/BSE micrographs of local sliding wear tracks on coating's surface in (a) initial state ~ 0 h and (b) final state ~ 1200 h with indications for the respective wear mechanisms. Corresponding EDX spectra show surfaces chemical composition after the test.

Fig. 16. LRDI and SEM/BSE micrographs of local sliding wear tracks on substrate's surface in (a) initial state ~ 0 h and (b) final state ~ 1200 h with indications for the respective wear mechanisms. Corresponding EDX spectra show surfaces chemical composition after the test.

Fig. 17. Averaged COF evolution during the sliding wear tests against alumina counterpart for each of (a) coating's and (b) substrate's states

Fig. 18. Quantitative results for (a) coating's, (b) substrate's and the respective counterpart's calculated and averaged wear rate *k* and the medium COF of each state after sliding wear tests

Fig. 19. CLSM/CCSPI of significant erosion scar regions at impact angle of 30° and 90° of all coating's and substrate's states at the end of the test. Colour coding is set from red +20 µm to dark blue -55 µm in respect to the zero-point.

Fig. 20. Quantitative results for (a) coating's and (b) substrate's measured and averaged mass losses of each state during solid particle erosion tests at an impact angle of 30 °

Fig. 21. Quantitative results for (a) coating's and (b) substrate's measured and averaged mass losses of each state during solid particle erosion tests at an impact angle of 90 °

Figures

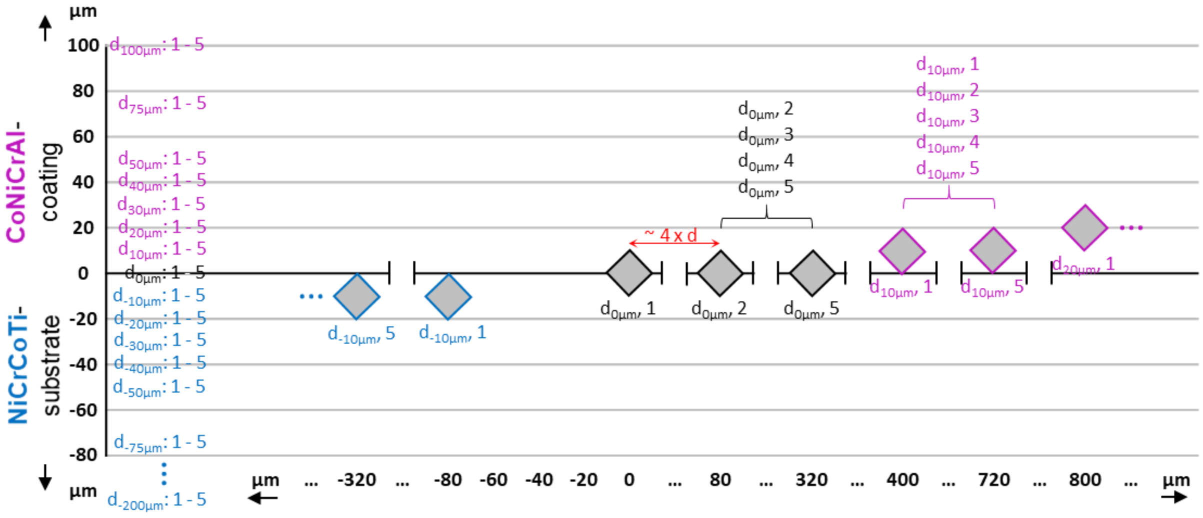

Fig. 1

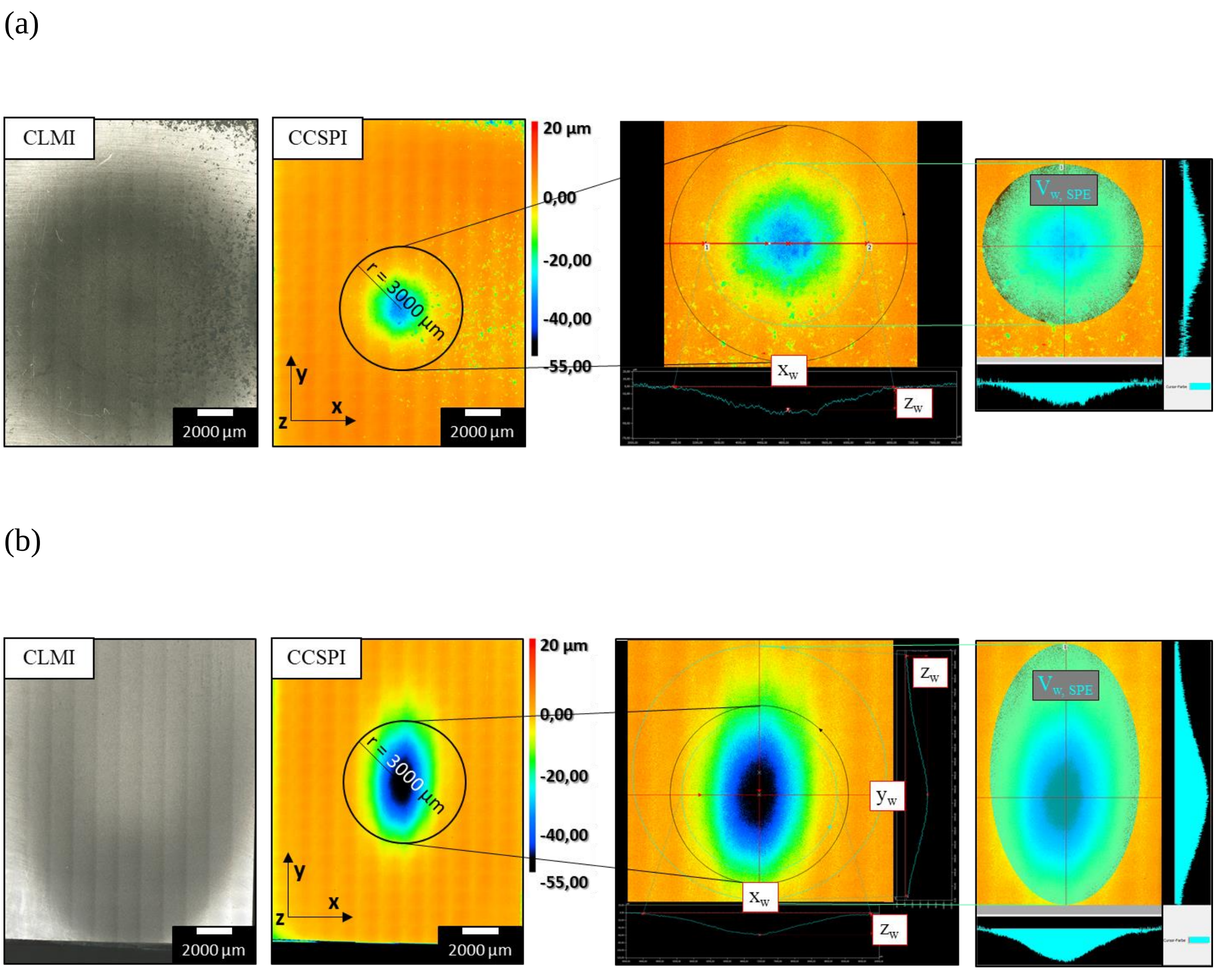
(a)
CLMI
2000 µm
CCSPI
r = 3000 µm
y
x
z
2000 µm
20 µm
0,00
-20,00
-40,00
-55,00
x_w
z_w
V_w, SPE
(b)
CLMI
2000 µm
CCSPI
r = 3000 µm
y
x
z
2000 µm
20 µm
0,00
-20,00
-40,00
-55,00
z_w
y_w
x_w
z_w
V_w, SPE

Fig. 2

(a)

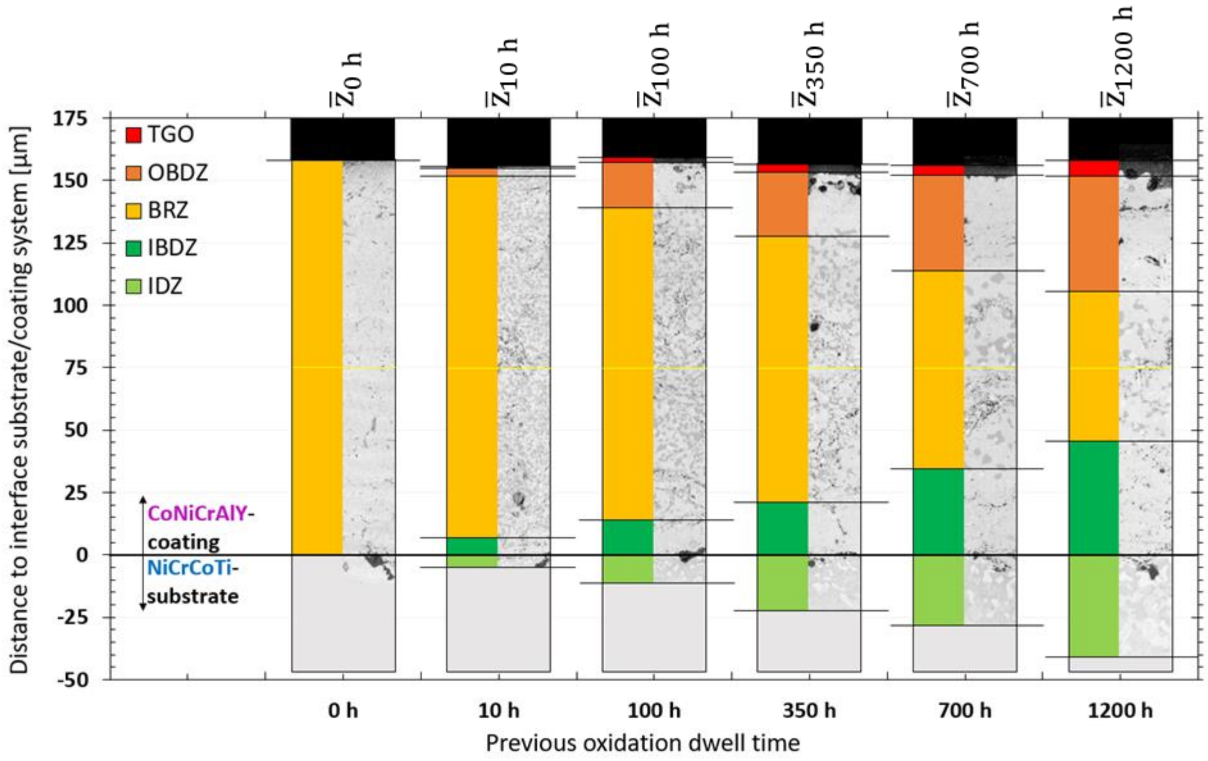
$\bar{z}_{0\ h}$
$\bar{z}_{10\ h}$
$\bar{z}_{100\ h}$
$\bar{z}_{350\ h}$
$\bar{z}_{700\ h}$
$\bar{z}_{1200\ h}$
175
150
125
100
75
50
25
0
-25
-50
Distance to interface substrate/coating system [µm]
🟥 TGO
🟧 OBDZ
🟨 BRZ
🟩 IBDZ
🟩 IDZ
CoNiCrAlY-
coating
NiCrCoTi-
substrate
0 h
10 h
100 h
350 h
700 h
1200 h
Previous oxidation dwell time

(b)

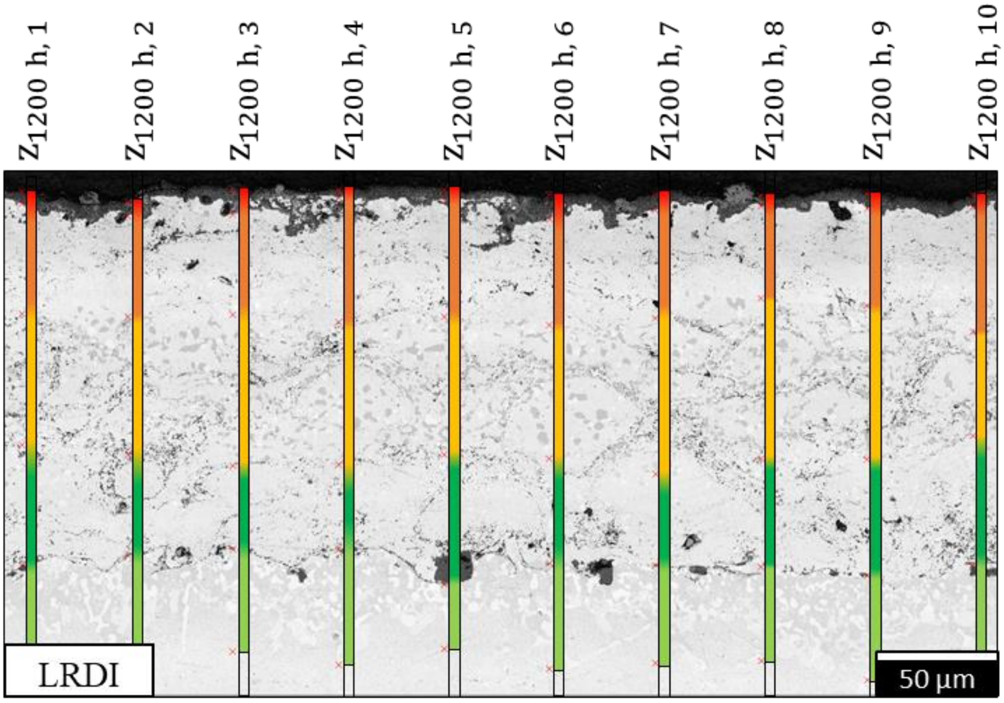
$z_{1200\ h,\ 1}$
$z_{1200\ h,\ 2}$
$z_{1200\ h,\ 3}$
$z_{1200\ h,\ 4}$
$z_{1200\ h,\ 5}$
$z_{1200\ h,\ 6}$
$z_{1200\ h,\ 7}$
$z_{1200\ h,\ 8}$
$z_{1200\ h,\ 9}$
$z_{1200\ h,\ 10}$
LRDI
50 µm

Fig. 3

(a)

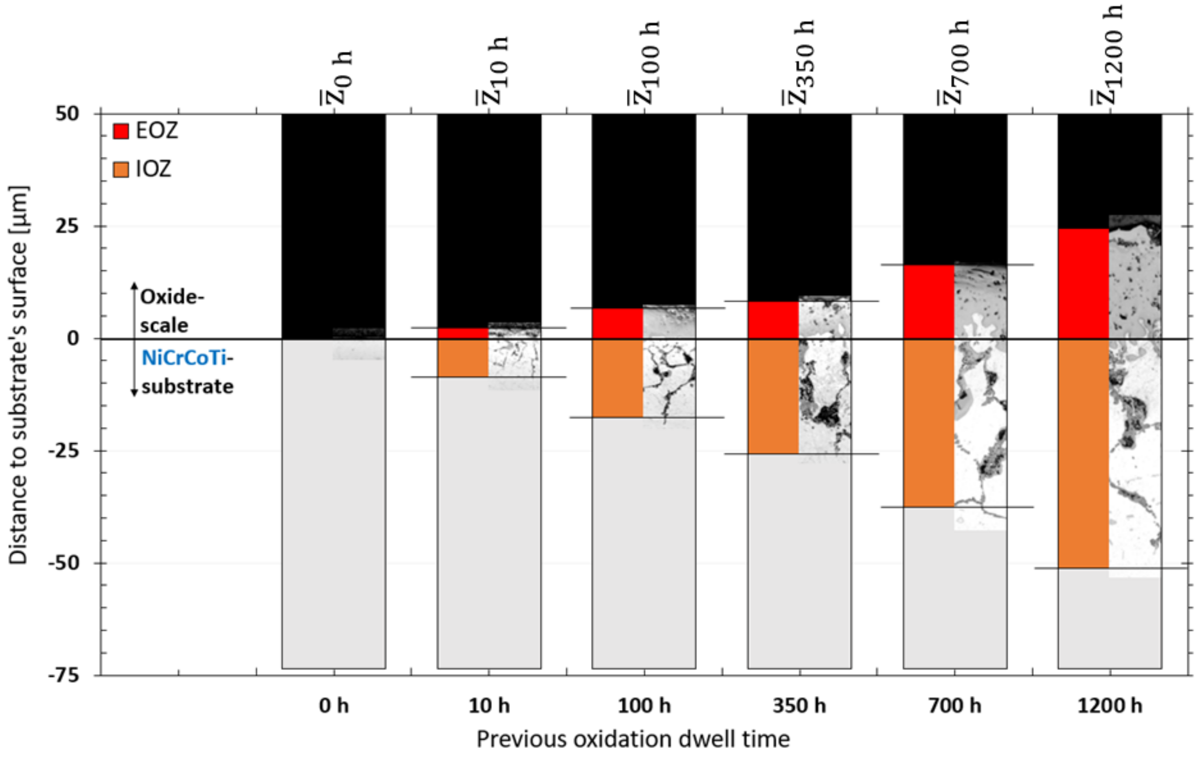
$\bar{z}_{0\ h}$
$\bar{z}_{10\ h}$
$\bar{z}_{100\ h}$
$\bar{z}_{350\ h}$
$\bar{z}_{700\ h}$
$\bar{z}_{1200\ h}$
🟥 EOZ
🟧 IOZ
Oxide-
scale
NiCrCoTi-
substrate
50
25
0
-25
-50
-75
Distance to substrate's surface [µm]
0 h
10 h
100 h
350 h
700 h
1200 h
Previous oxidation dwell time

(b)

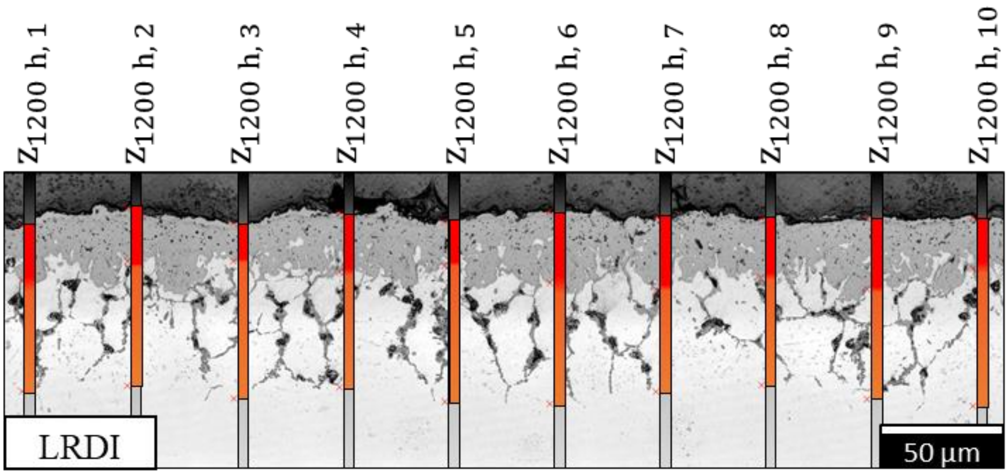
$z_{1200\ h,\ 1}$
$z_{1200\ h,\ 2}$
$z_{1200\ h,\ 3}$
$z_{1200\ h,\ 4}$
$z_{1200\ h,\ 5}$
$z_{1200\ h,\ 6}$
$z_{1200\ h,\ 7}$
$z_{1200\ h,\ 8}$
$z_{1200\ h,\ 9}$
$z_{1200\ h,\ 10}$
LRDI
50 µm

Fig. 4

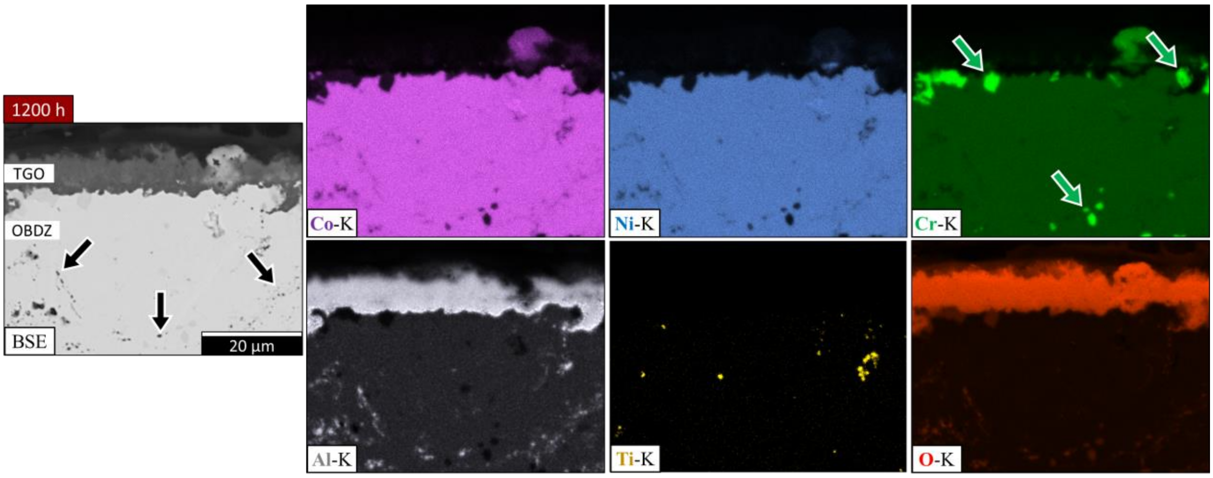

Fig. 5

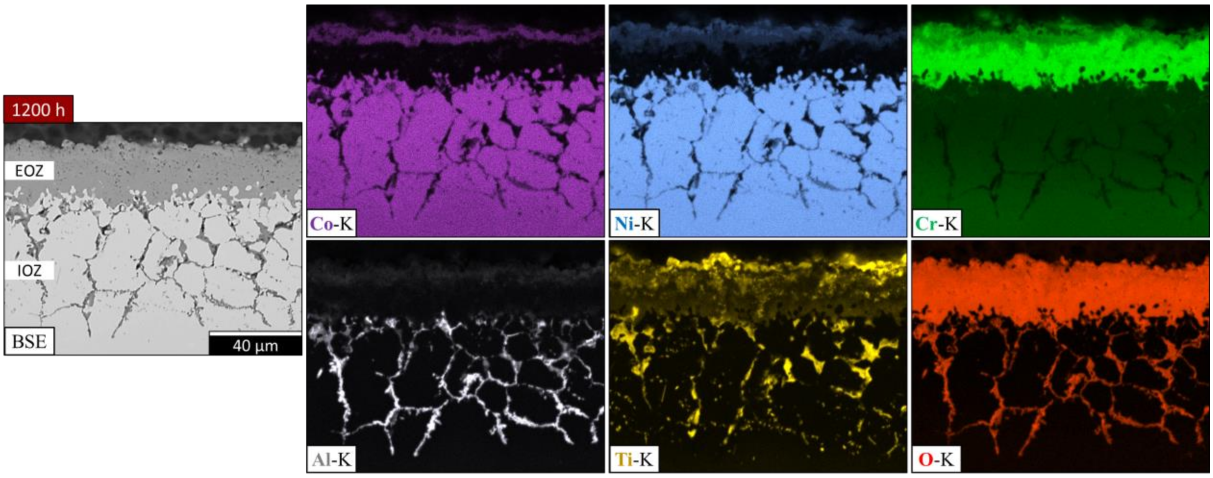

Fig. 6

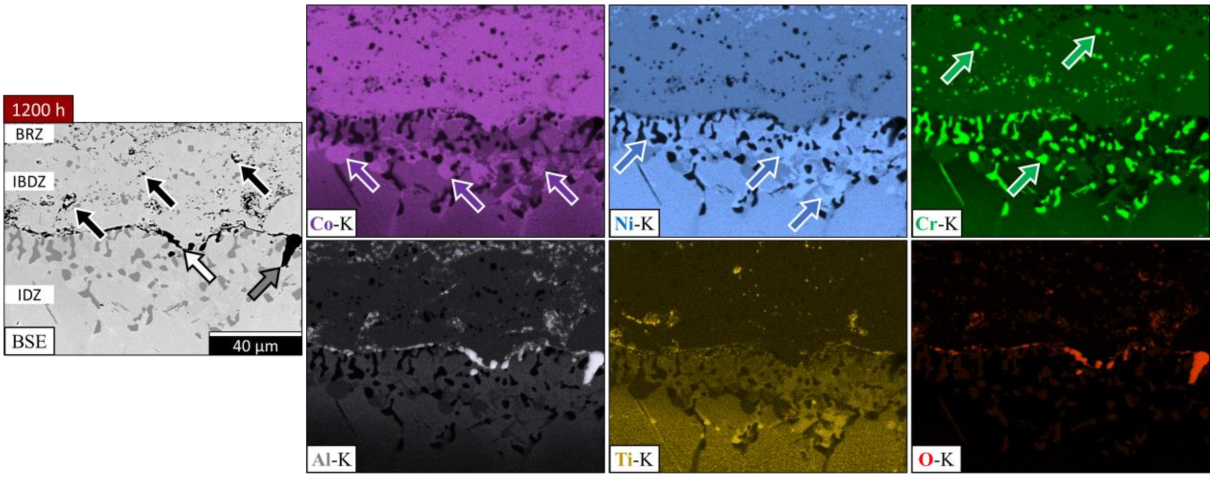

Fig. 7

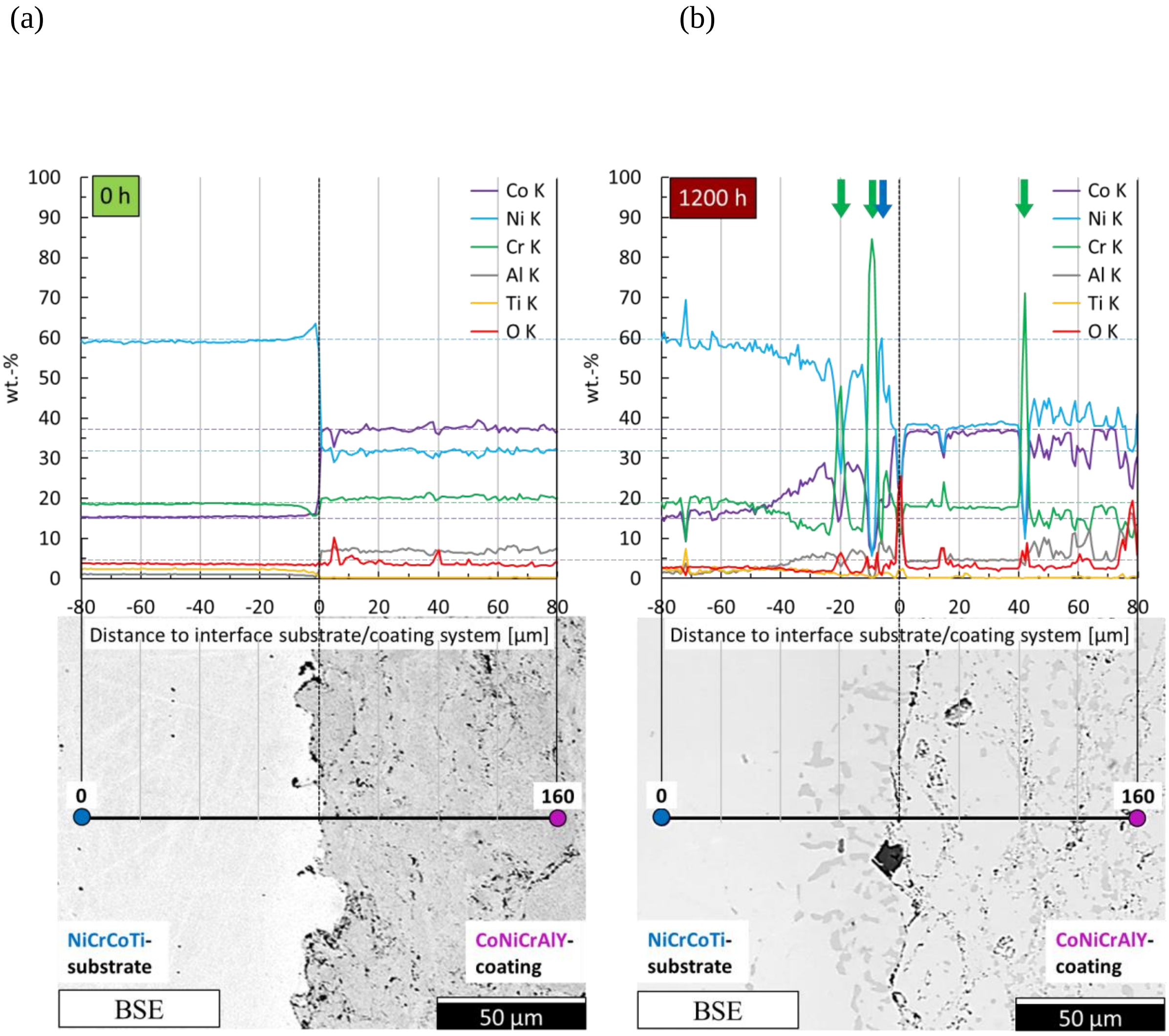

(a)
(b)
0 h
1200 h
Co K
Ni K
Cr K
Al K
Ti K
O K
wt.-%
100
90
80
70
60
50
40
30
20
10
0
-80
-60
-40
-20
0
20
40
60
80
Distance to interface substrate/coating system [µm]
0
160
NiCrCoTi-substrate
CoNiCrAlY-coating
BSE
50 µm

Fig. 8

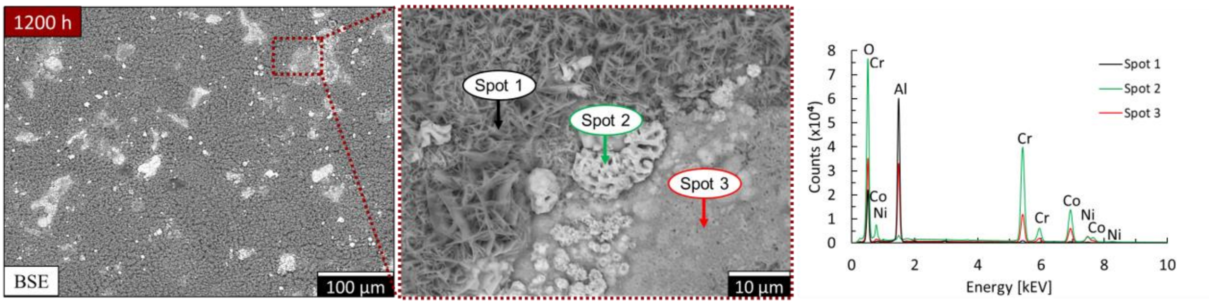
1200 h
BSE
100 µm
Spot 1
Spot 2
Spot 3
10 µm
Counts (x10⁴)
Energy [kEV]
O
Cr
Al
Co
Ni
Cr
Cr
Co
Ni
Co
Ni
Spot 1
Spot 2
Spot 3
0
1
2
3
4
5
6
7
8
0
2
4
6
8
10

Fig. 9

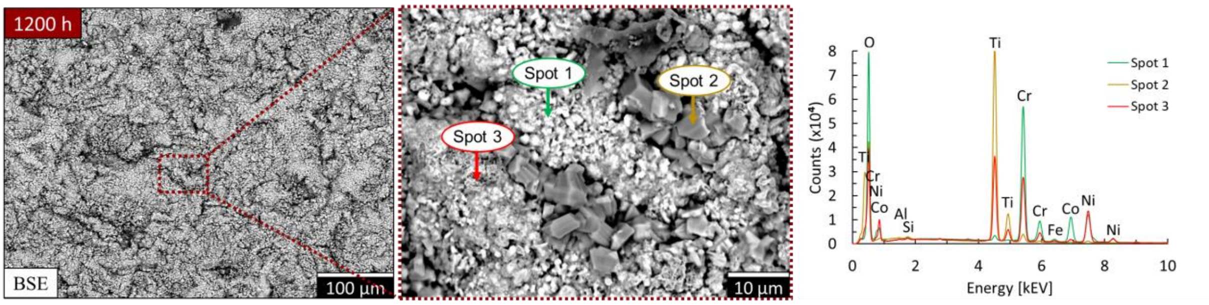
1200 h
BSE
100 µm
Spot 1
Spot 2
Spot 3
10 µm
Counts (x10⁴)
Energy [kEV]
O
Ti
Ti
Cr
Ni
Co
Al
Si
Ti
Cr
Fe
Co
Ni
Cr
Ni
Spot 1
Spot 2
Spot 3
0
1
2
3
4
5
6
7
8
0
2
4
6
8
10

Fig. 10

(a)

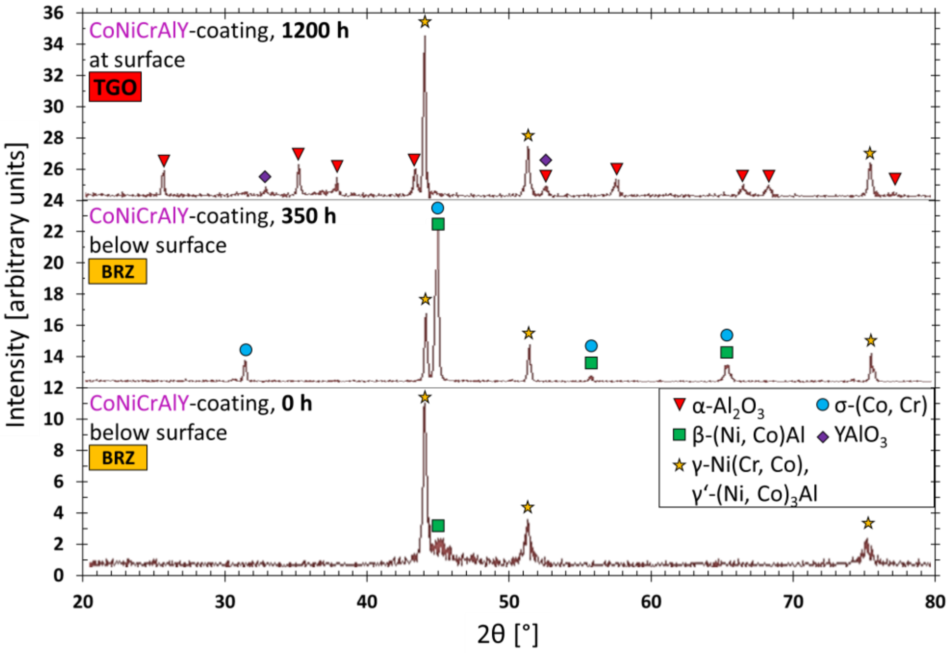
CoNiCrAlY-coating, 1200 h
at surface
TGO
CoNiCrAlY-coating, 350 h
below surface
BRZ
CoNiCrAlY-coating, 0 h
below surface
BRZ
α-Al_2O_3
σ-(Co, Cr)
β-(Ni, Co)Al
$YAlO_3$
γ-Ni(Cr, Co),
γ'-$(Ni, Co)_3Al$
Intensity [arbitrary units]
2θ [°]
0
2
4
6
8
10
12
14
16
18
20
22
24
26
28
30
32
34
36
20
30
40
50
60
70
80

(b)

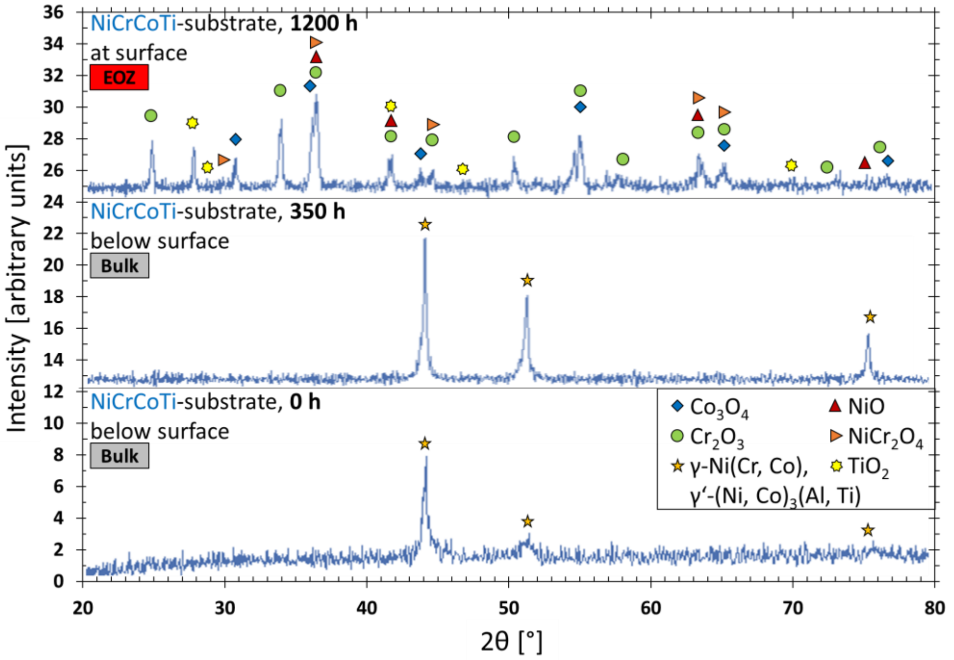
NiCrCoTi-substrate, 1200 h
at surface
EOZ
NiCrCoTi-substrate, 350 h
below surface
Bulk
NiCrCoTi-substrate, 0 h
below surface
Bulk
Co_3O_4
NiO
Cr_2O_3
$NiCr_2O_4$
γ-Ni(Cr, Co),
TiO_2
γ'-$(Ni, Co)_3(Al, Ti)$
Intensity [arbitrary units]
2θ [°]
0
2
4
6
8
10
12
14
16
18
20
22
24
26
28
30
32
34
36
20
30
40
50
60
70
80

Fig. 11

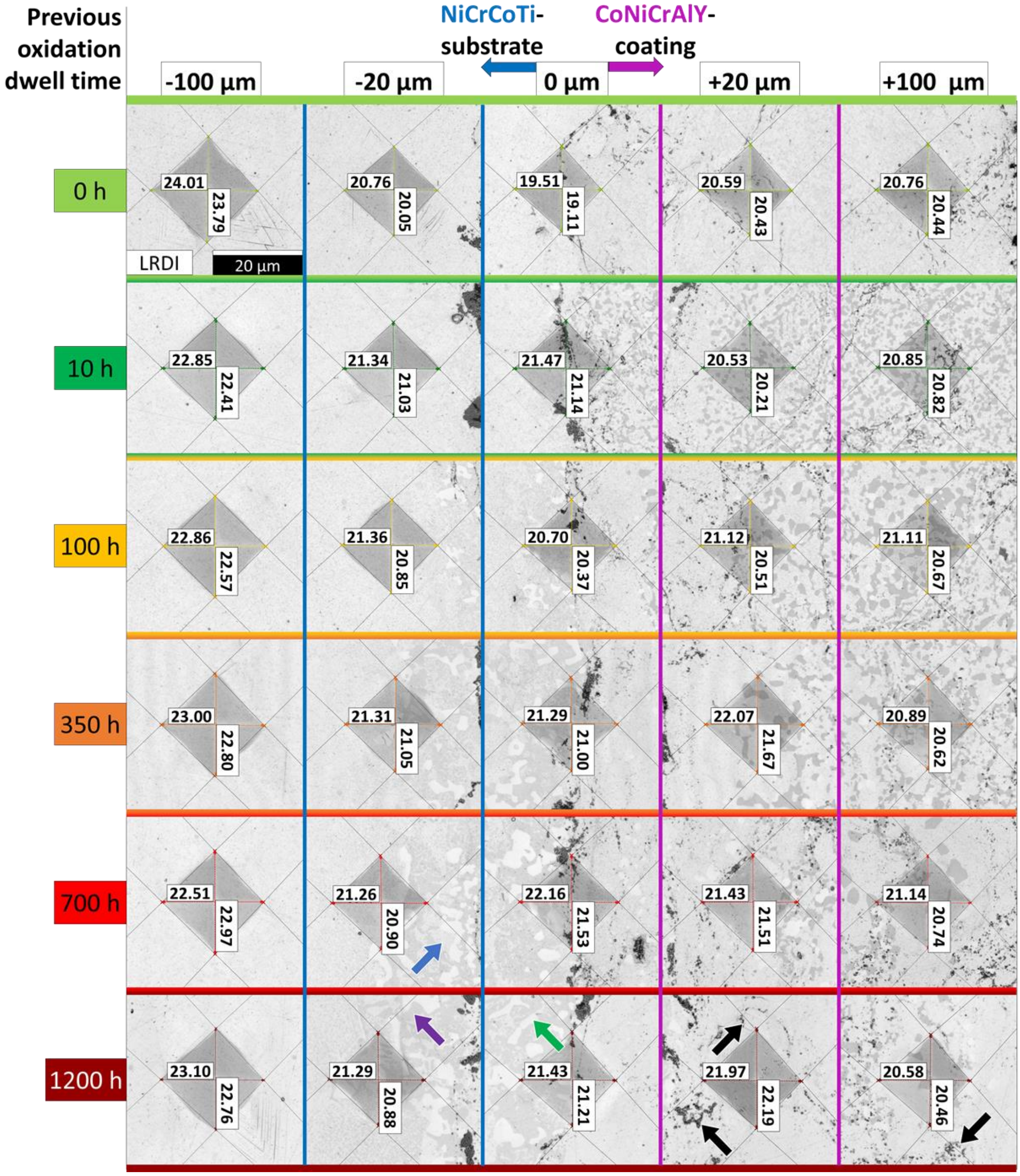
Previous oxidation dwell time
NiCrCoTi-substrate
CoNiCrAlY-coating
-100 µm
-20 µm
0 µm
+20 µm
+100 µm
0 h
24.01
23.79
LRDI
20 µm
20.76
20.05
19.51
19.11
20.59
20.43
20.76
20.44
10 h
22.85
22.41
21.34
21.03
21.47
21.14
20.53
20.21
20.85
20.82
100 h
22.86
22.57
21.36
20.85
20.70
20.37
21.12
20.51
21.11
20.67
350 h
23.00
22.80
21.31
21.05
21.29
21.00
22.07
21.67
20.89
20.62
700 h
22.51
22.97
21.26
20.90
22.16
21.53
21.43
21.51
21.14
20.74
1200 h
23.10
22.76
21.29
20.88
21.43
21.21
21.97
22.19
20.58
20.46

Fig. 12

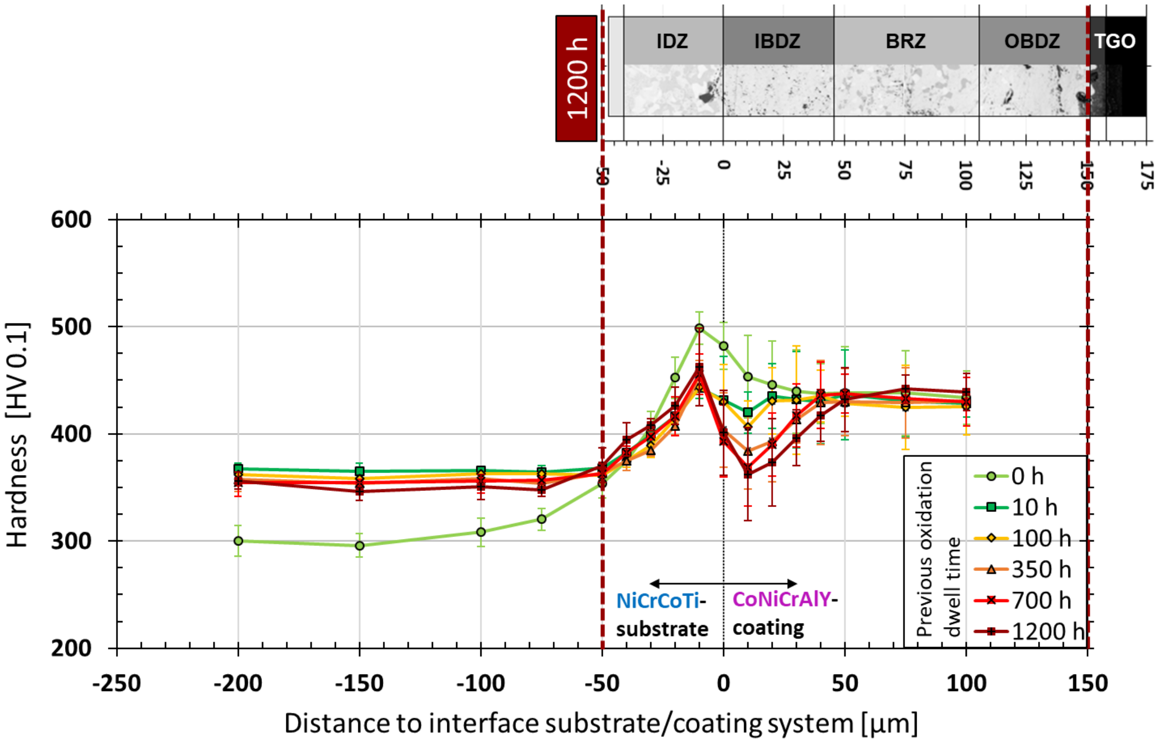
1200 h
IDZ
IBDZ
BRZ
OBDZ
TGO
-50
-25
0
25
50
75
100
125
150
175
600
500
400
300
200
Hardness [HV 0.1]
-250
-200
-150
-100
-50
0
50
100
150
Distance to interface substrate/coating system [µm]
NiCrCoTi-
substrate
CoNiCrAlY-
coating
Previous oxidation
dwell time
0 h
10 h
100 h
350 h
700 h
1200 h

Fig. 13

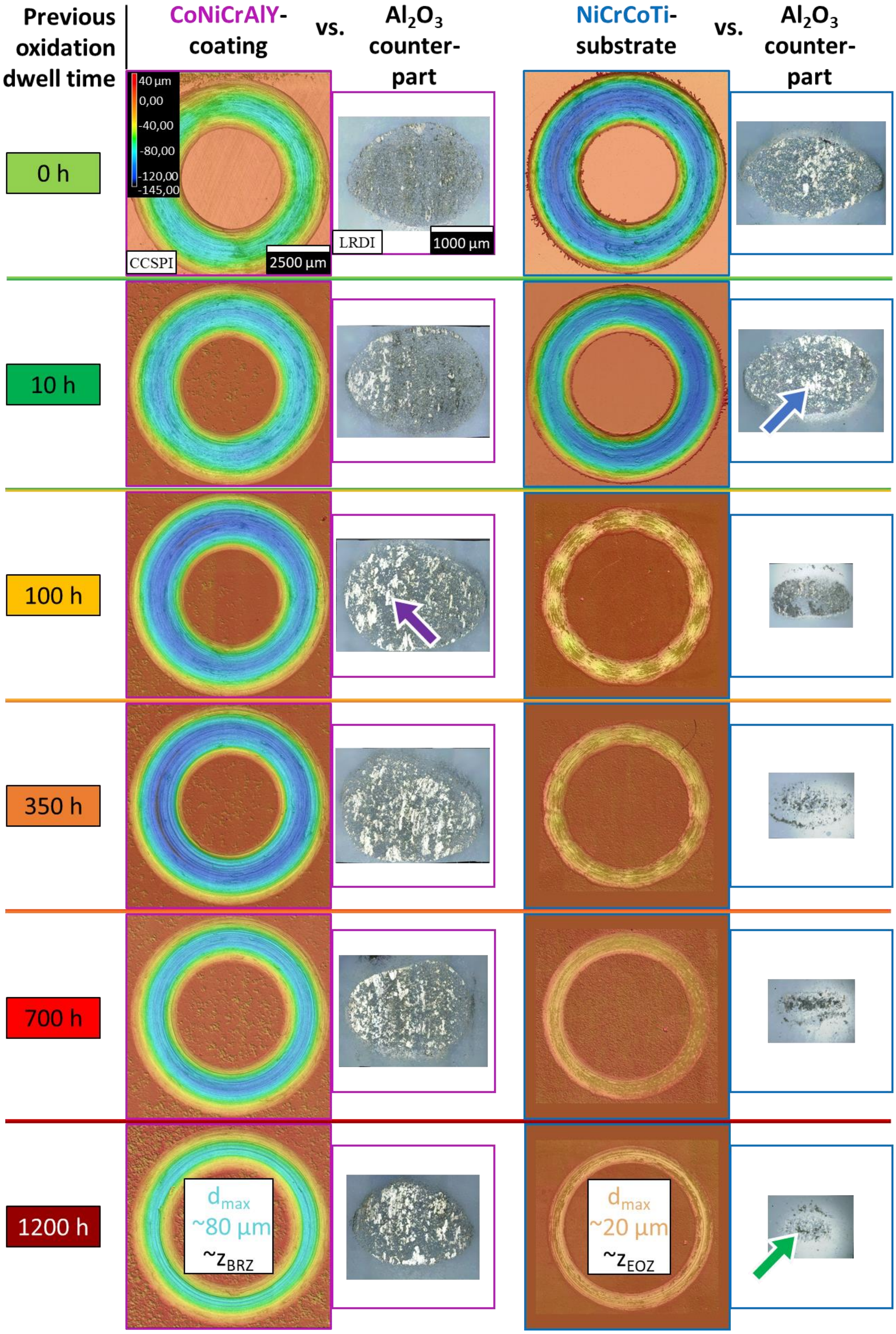
Previous oxidation dwell time
CoNiCrAlY-coating
vs.
Al_2O_3 counter-part
NiCrCoTi-substrate
vs.
Al_2O_3 counter-part
40 µm
0,00
-40,00
-80,00
-120,00
-145,00
CCSPI
2500 µm
LRDI
1000 µm
0 h
10 h
100 h
350 h
700 h
1200 h
d_{max} ~80 µm ~z_{BRZ}
d_{max} ~20 µm ~z_{EOZ}

Fig. 14

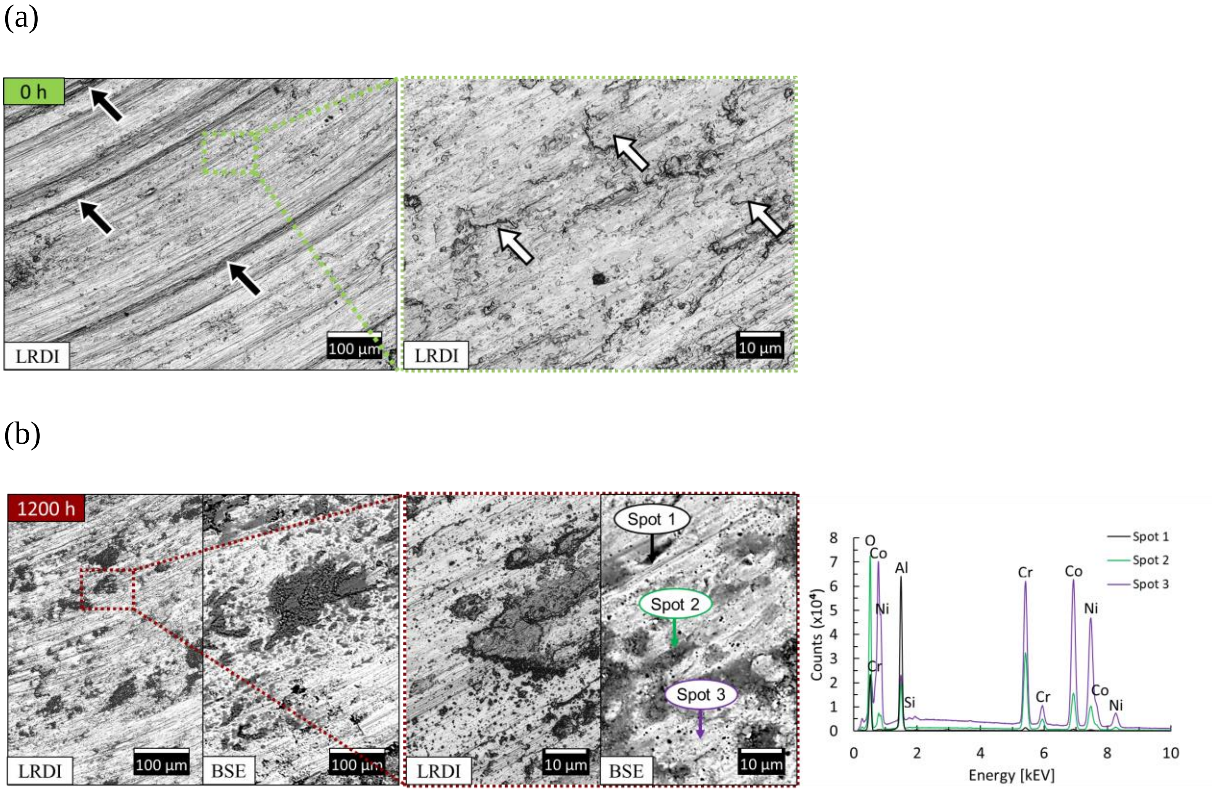
(a)
0 h
LRDI
100 µm
LRDI
10 µm
(b)
1200 h
LRDI
100 µm
BSE
100 µm
LRDI
10 µm
BSE
10 µm
Spot 1
Spot 2
Spot 3
Counts (x10⁴)
Energy [kEV]
O
Co
Ni
Cr
Al
Si
Cr
Co
Ni
Cr
Co
Ni
Spot 1
Spot 2
Spot 3

Fig. 15

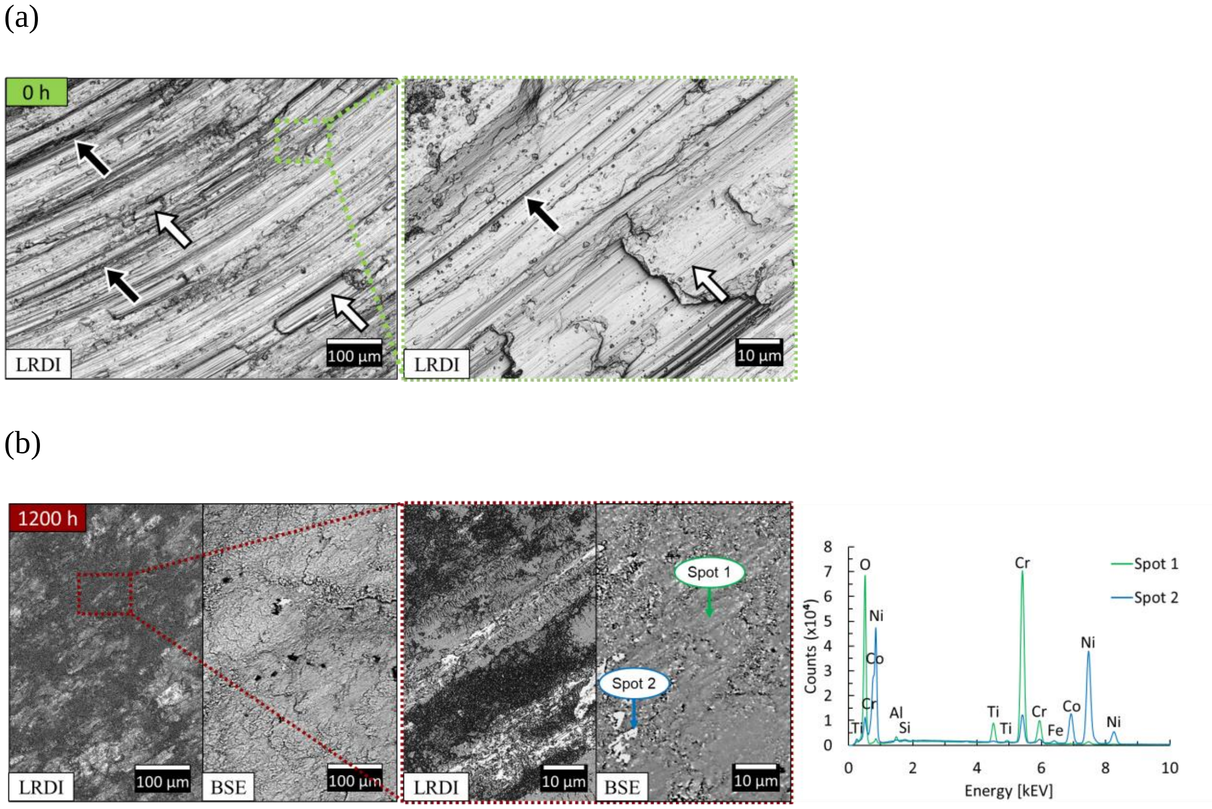
(a)
0 h
LRDI
100 µm
LRDI
10 µm
(b)
1200 h
LRDI
100 µm
BSE
100 µm
LRDI
10 µm
BSE
10 µm
Spot 1
Spot 2
Counts (x10⁴)
Energy [kEV]
O
Ni
Co
Cr
Ti
Al
Si
Ti
Ti
Cr
Cr
Fe
Co
Ni
Ni
Spot 1
Spot 2

Fig. 16

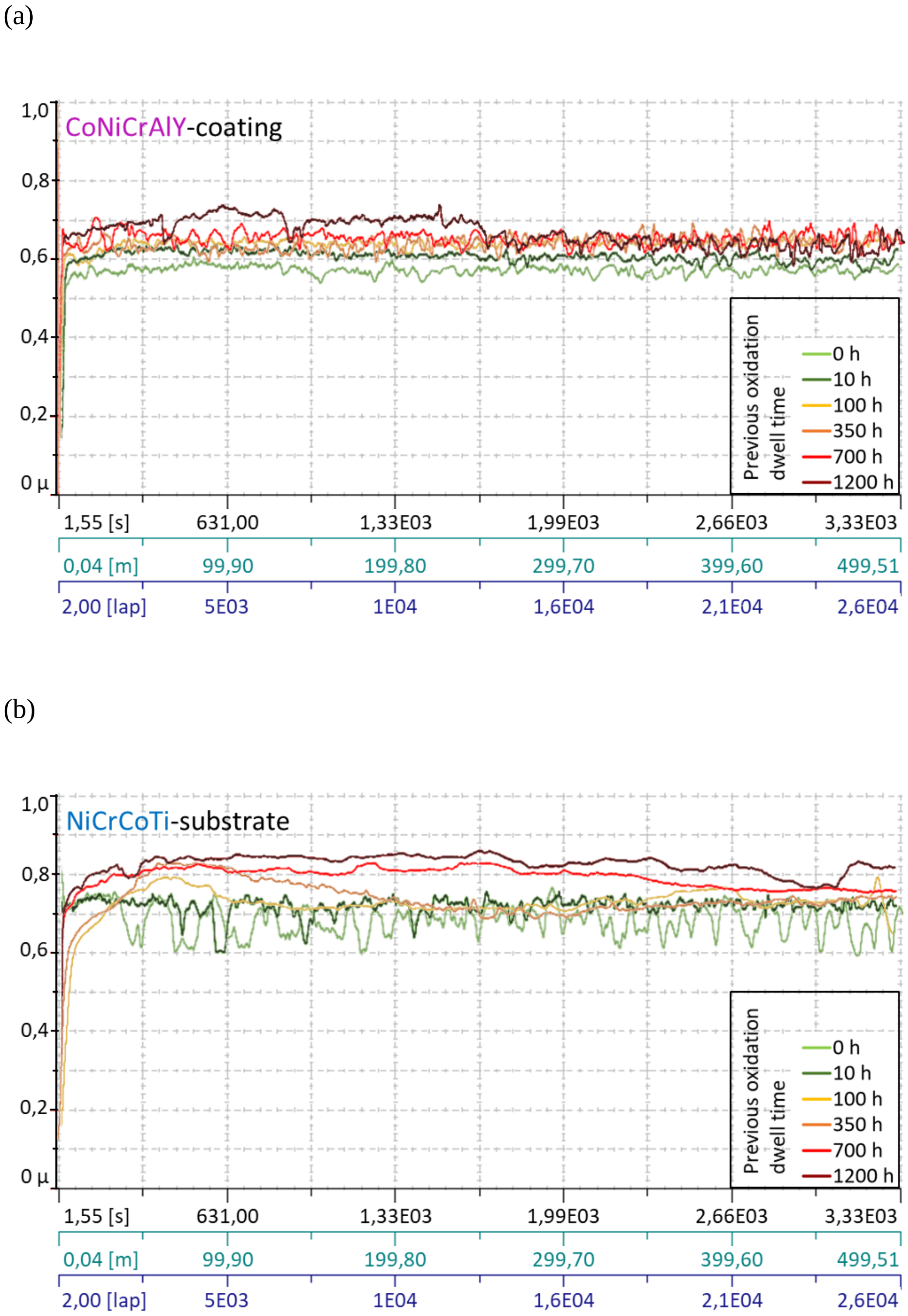
(a)
CoNiCrAlY-coating
1,0
0,8
0,6
0,4
0,2
0 µ
Previous oxidation dwell time
0 h
10 h
100 h
350 h
700 h
1200 h
1,55 [s]
631,00
1,33E03
1,99E03
2,66E03
3,33E03
0,04 [m]
99,90
199,80
299,70
399,60
499,51
2,00 [lap]
5E03
1E04
1,6E04
2,1E04
2,6E04
(b)
NiCrCoTi-substrate
1,0
0,8
0,6
0,4
0,2
0 µ
Previous oxidation dwell time
0 h
10 h
100 h
350 h
700 h
1200 h
1,55 [s]
631,00
1,33E03
1,99E03
2,66E03
3,33E03
0,04 [m]
99,90
199,80
299,70
399,60
499,51
2,00 [lap]
5E03
1E04
1,6E04
2,1E04
2,6E04

Fig. 17

(a)

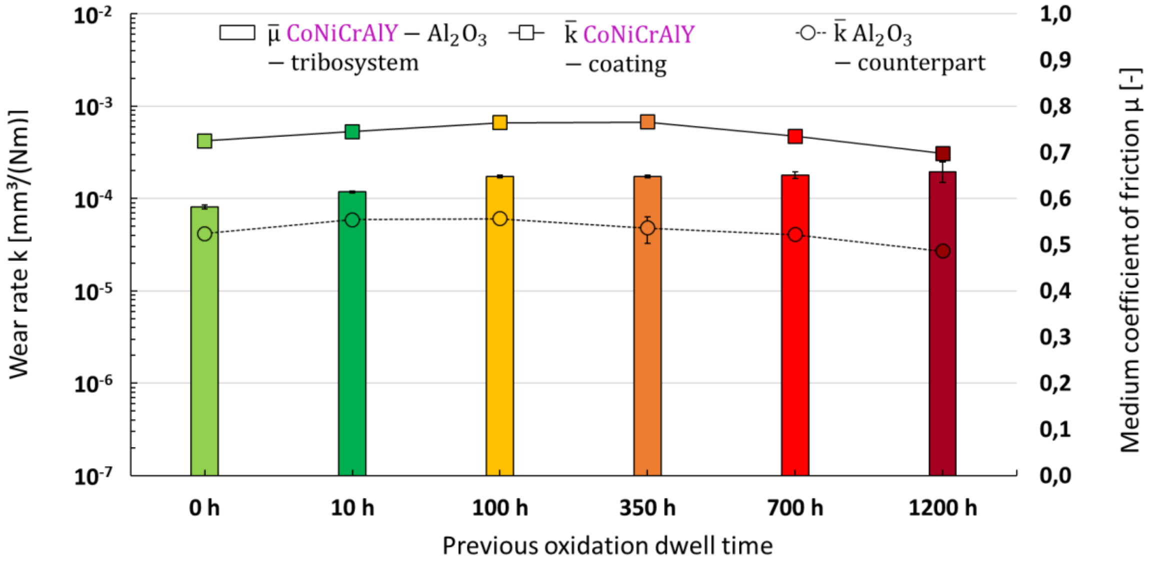
μ̄ CoNiCrAlY – Al₂O₃ – tribosystem
k̄ CoNiCrAlY – coating
k̄ Al₂O₃ – counterpart
Wear rate k [mm³/(Nm)]
10-2
10-3
10-4
10-5
10-6
10-7
Medium coefficient of friction μ [-]
1,0
0,9
0,8
0,7
0,6
0,5
0,4
0,3
0,2
0,1
0,0
0 h
10 h
100 h
350 h
700 h
1200 h
Previous oxidation dwell time

(b)

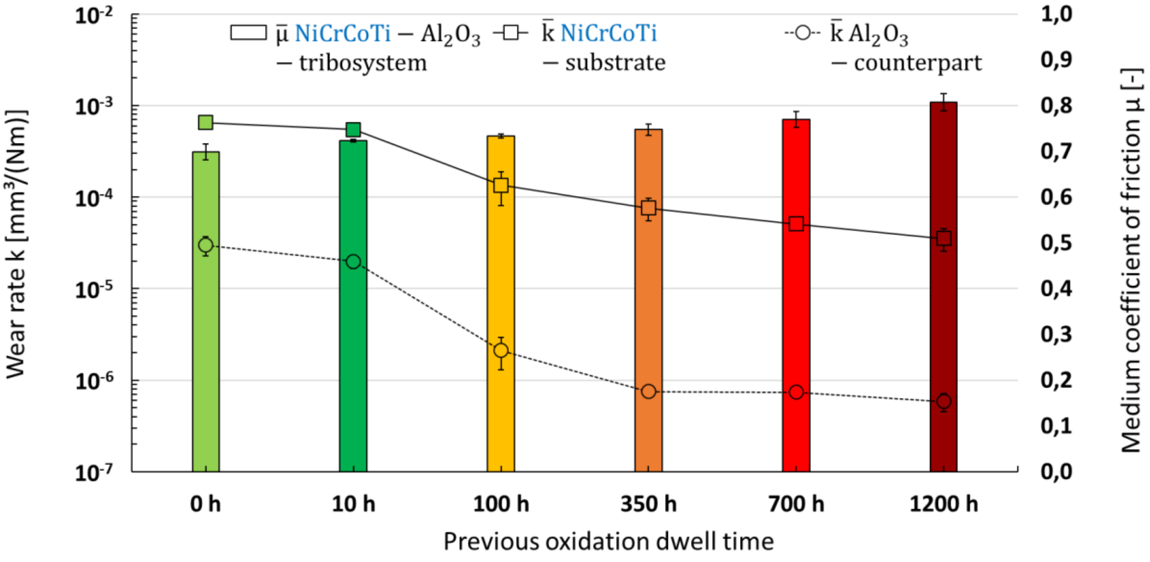
μ̄ NiCrCoTi – Al₂O₃ – tribosystem
k̄ NiCrCoTi – substrate
k̄ Al₂O₃ – counterpart
Wear rate k [mm³/(Nm)]
10-2
10-3
10-4
10-5
10-6
10-7
Medium coefficient of friction μ [-]
1,0
0,9
0,8
0,7
0,6
0,5
0,4
0,3
0,2
0,1
0,0
0 h
10 h
100 h
350 h
700 h
1200 h
Previous oxidation dwell time

Fig. 18

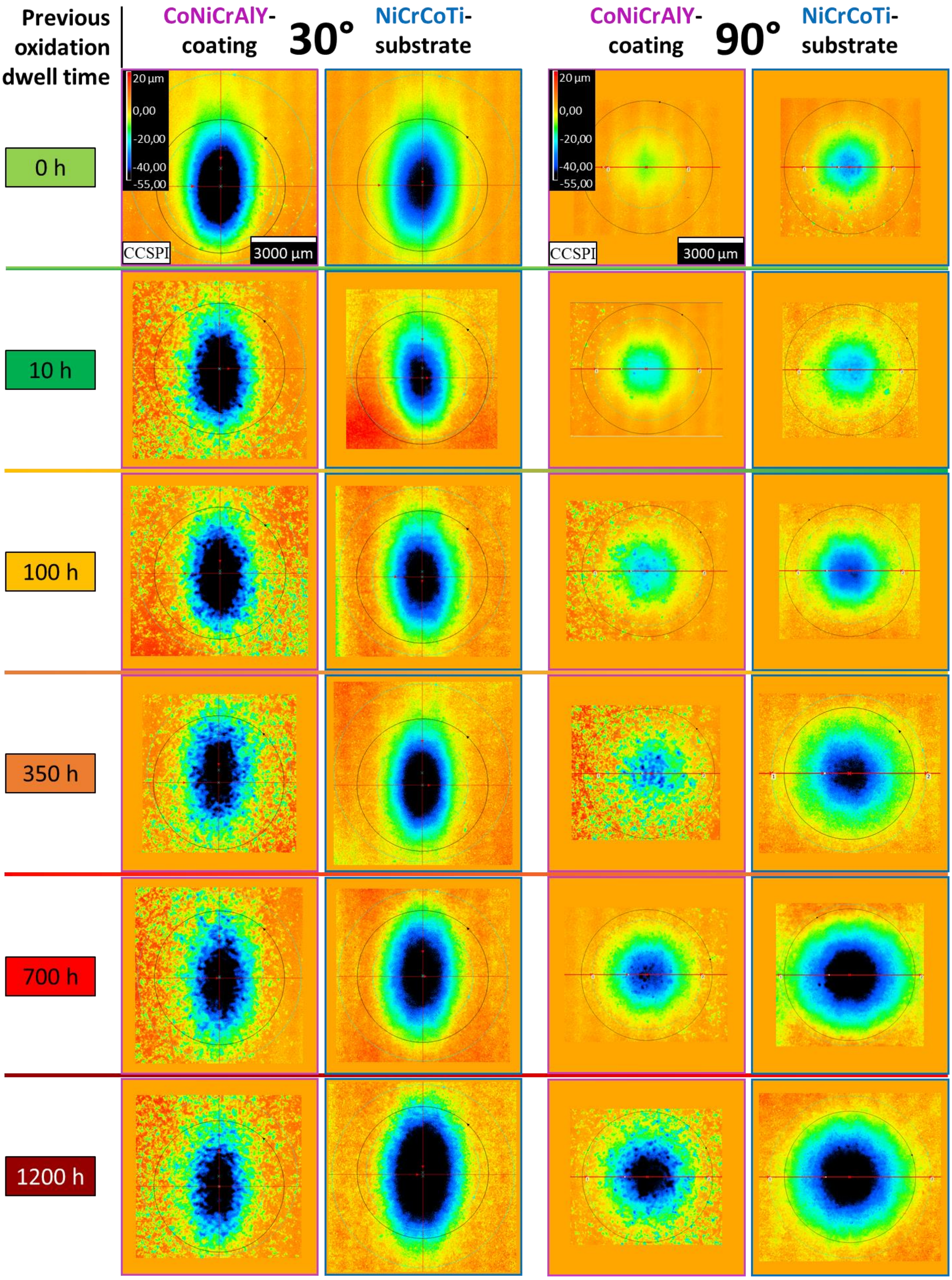
Previous oxidation dwell time
CoNiCrAlY-coating
30°
NiCrCoTi-substrate
CoNiCrAlY-coating
90°
NiCrCoTi-substrate
20 µm
0,00
-20,00
-40,00
-55,00
CCSPI
3000 µm
20 µm
0,00
-20,00
-40,00
-55,00
CCSPI
3000 µm
0 h
10 h
100 h
350 h
700 h
1200 h

Fig. 19

(a)

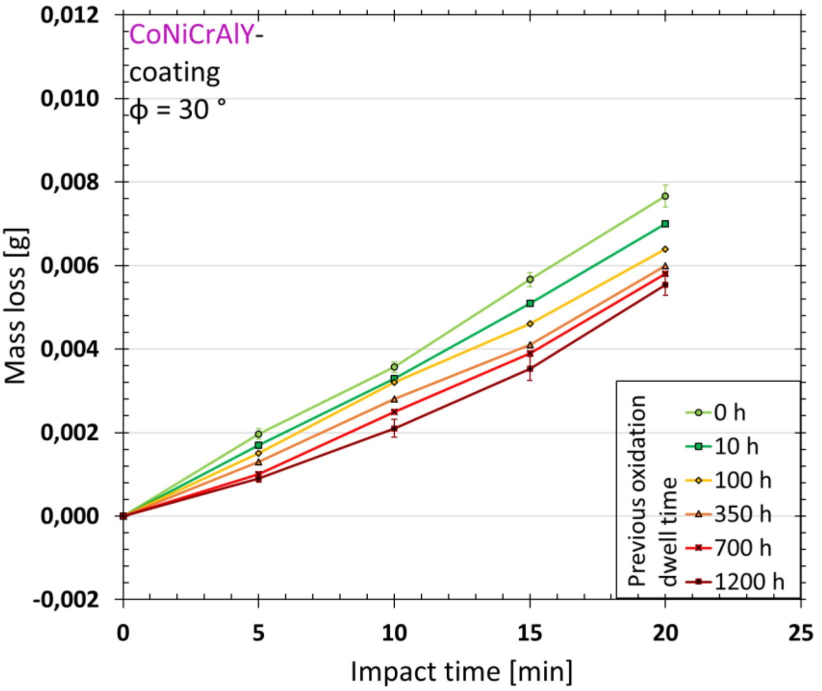
CoNiCrAlY-
coating
ϕ = 30 °
Mass loss [g]
0,012
0,010
0,008
0,006
0,004
0,002
0,000
-0,002
Impact time [min]
0
5
10
15
20
25
Previous oxidation
dwell time
0 h
10 h
100 h
350 h
700 h
1200 h

(b)

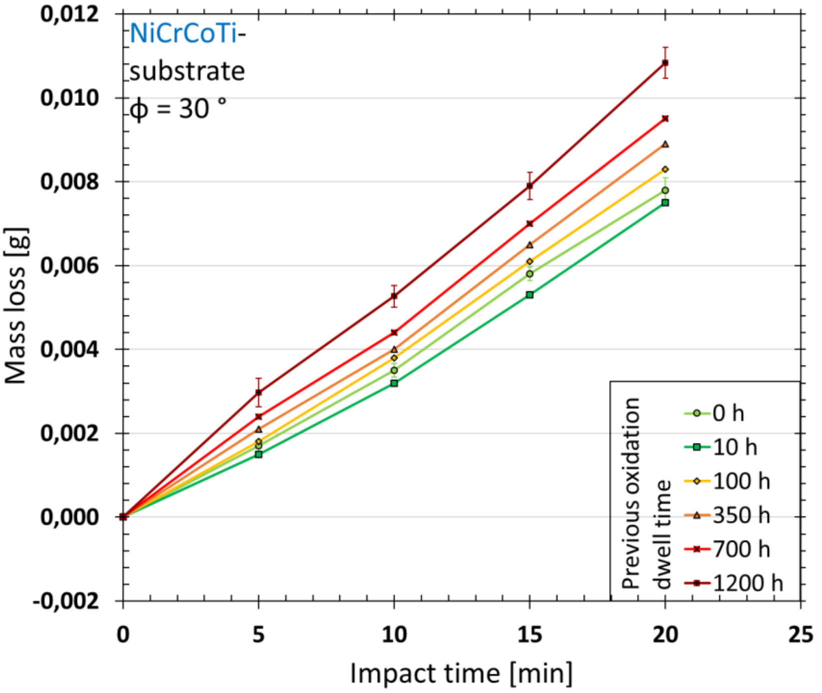
NiCrCoTi-
substrate
ϕ = 30 °
Mass loss [g]
0,012
0,010
0,008
0,006
0,004
0,002
0,000
-0,002
Impact time [min]
0
5
10
15
20
25
Previous oxidation
dwell time
0 h
10 h
100 h
350 h
700 h
1200 h

Fig. 20

(a)

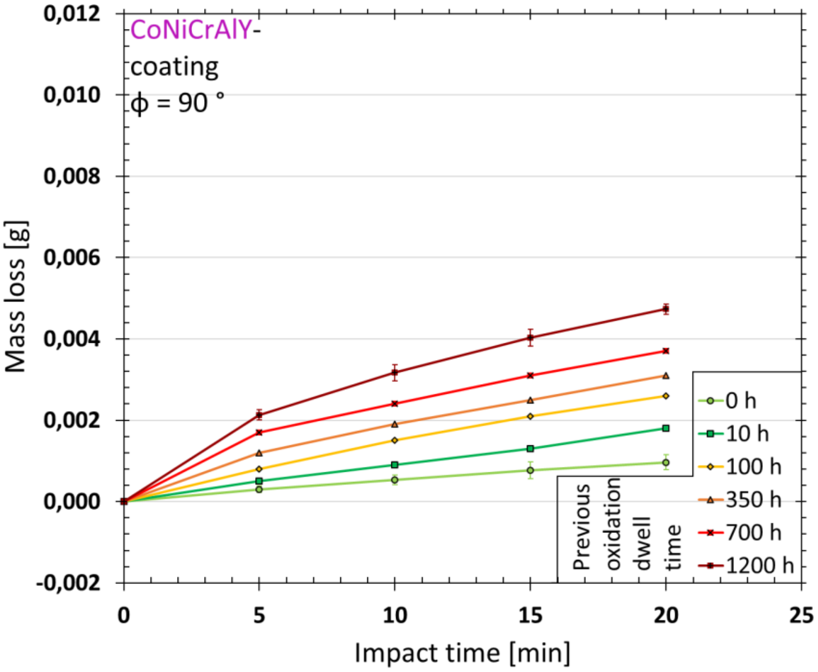

CoNiCrAlY-
coating
ϕ = 90 °
Mass loss [g]
0,012
0,010
0,008
0,006
0,004
0,002
0,000
-0,002
0
5
10
15
20
25
Impact time [min]
Previous oxidation dwell time
0 h
10 h
100 h
350 h
700 h
1200 h

(b)

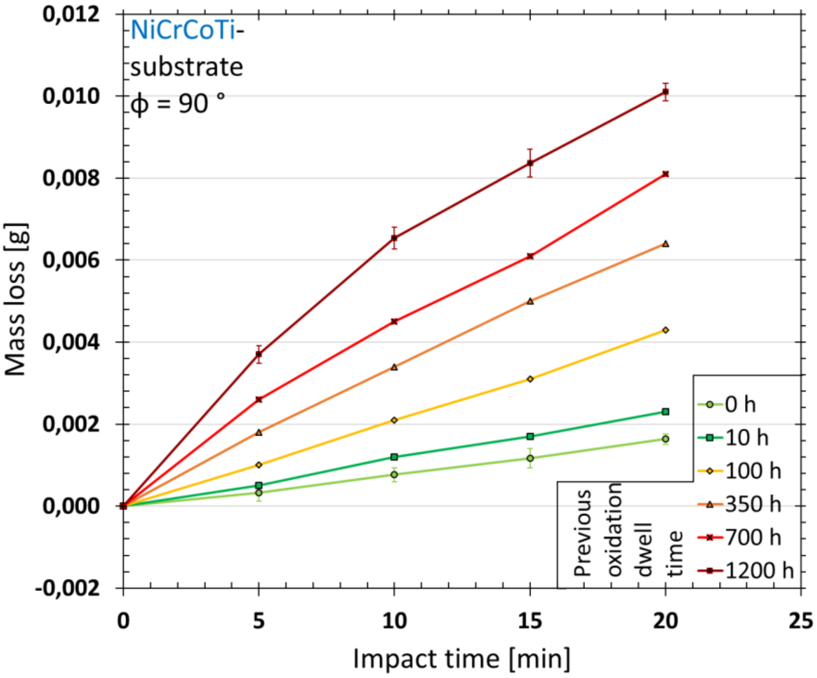

NiCrCoTi-
substrate
ϕ = 90 °
Mass loss [g]
0,012
0,010
0,008
0,006
0,004
0,002
0,000
-0,002
0
5
10
15
20
25
Impact time [min]
Previous oxidation dwell time
0 h
10 h
100 h
350 h
700 h
1200 h

Fig. 21

Tables

Table 1
Chemical compositions in weight percent from [27,60] for the powder material CoNiCrAlY (Amdry 995) and from chemical analysis for the substrate material NiCrCoTi (Nimonic 90)

Material	Co	Ni	Cr	Al	Ti	Y
Amdry 995	Bal.	34	21.3	8.39	-	0.42
Nimonic 90	15.7	Bal.	19.3	1.4	2.4	-

Table 2
Designation of the respective sample states and corresponding oxidation dwell times

Designation	Oxidation dwell time
Initial state	0 h
Second state	10 h
Third state	100 h
Fourth state	350 h
Fifth state	700 h
Final state	1200 h

Table 3
Selected test parameters and varied control variables for performing solid particle erosion tests using an in-house developed air jet erosion testing rig

Test parameters		Control variables	
Transport medium	dry air	Transport medium velocity $v_{air}(\Delta p_{air})$	75 – 200 m/s
Erodent particles (Ep)	Al_2O_3	Ep-mass flow $\dot{m}_{Ep}$	2 – 10 g/min
Ep-size	50 µm	Testing angle φ	15 – 90 °
$Ø_{\mathrm{Nozzle}}$	1,5 ± 0,075 mm	Testing time t	5 – 20 min
Nozzle length l_N	50 mm		
Distance nozzle/sample a	10 ± 1 mm		
Test temperature T	20 – 30 °C		

Table 4
Measured and averaged sliding wear related samples mass losses of all coating’s and substrate’s states at the end of the test

	Mass loss [g]	
State	CoNiCrAlY-coating	NiCrCoTi-substrate
0 h	0.0146 ± 0.0006	0.0285 ± 0.0013
10 h	0.0183 ± 0.0003	0.0236 ± 0.0021
100 h	0.0225 ± 0.0014	0.0051 ± 0.0015
350 h	0.0221 ± 0.0022	0.0025 ± 0.0006
700 h	0.0155 ± 0.0014	0.0016 ± 0.0001
1200 h	0.0098 ± 0.0013	0.0011 ± 0.0002

Table 5
Measured and averaged solid particle erosion related samples wear volumes of all coating's and substrate's states at the end of the test

	Wear volume [mm³] at 30 ° impact angle		Wear volume [mm³] at 90 ° impact angle	
State	CoNiCrAlY-coating	NiCrCoTi-substrate	CoNiCrAlY-coating	NiCrCoTi-substrate
0 h	0.902 ± 0.006	0.689 ± 0.007	0.083 ± 0.009	0.194 ± 0.005
10 h	0.832	0.652	0.203	0.199
100 h	0.739	0.774	0.269	0.408
350 h	0.696	0.818	0.354	0.706
700 h	0.669	0.853	0.402	0.966
1200 h	0.649 ± 0.013	1.171 ± 0.0012	0.512 ± 0.015	1.062 ± 0.011

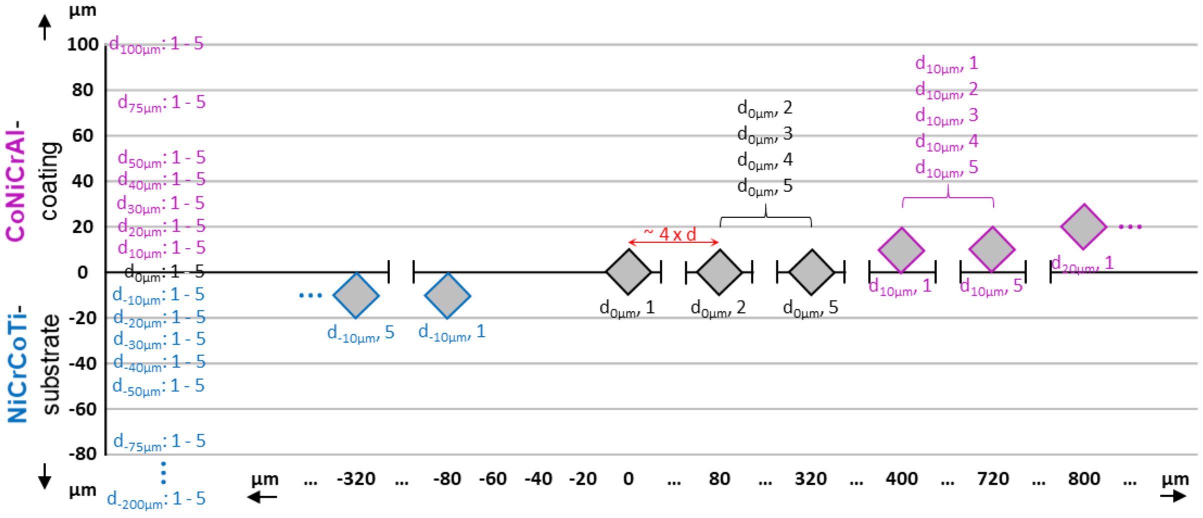
µm
100
80
60
40
20
0
-20
-40
-60
-80
µm
CoNiCrAl-
coating
NiCrCoTi-
substrate
d100µm: 1 - 5
d75µm: 1 - 5
d50µm: 1 - 5
d40µm: 1 - 5
d30µm: 1 - 5
d20µm: 1 - 5
d10µm: 1 - 5
d0µm: 1 - 5
d-10µm: 1 - 5
d-20µm: 1 - 5
d-30µm: 1 - 5
d-40µm: 1 - 5
d-50µm: 1 - 5
d-75µm: 1 - 5
d-200µm: 1 - 5
d-10µm, 5
d-10µm, 1
d0µm, 1
d0µm, 2
d0µm, 5
d0µm, 2
d0µm, 3
d0µm, 4
d0µm, 5
~ 4 x d
d10µm, 1
d10µm, 2
d10µm, 3
d10µm, 4
d10µm, 5
d10µm, 1
d10µm, 5
d20µm, 1
µm
...
-320
...
-80
-60
-40
-20
0
...
80
...
320
...
400
...
720
...
800
...
µm

Fig. 1

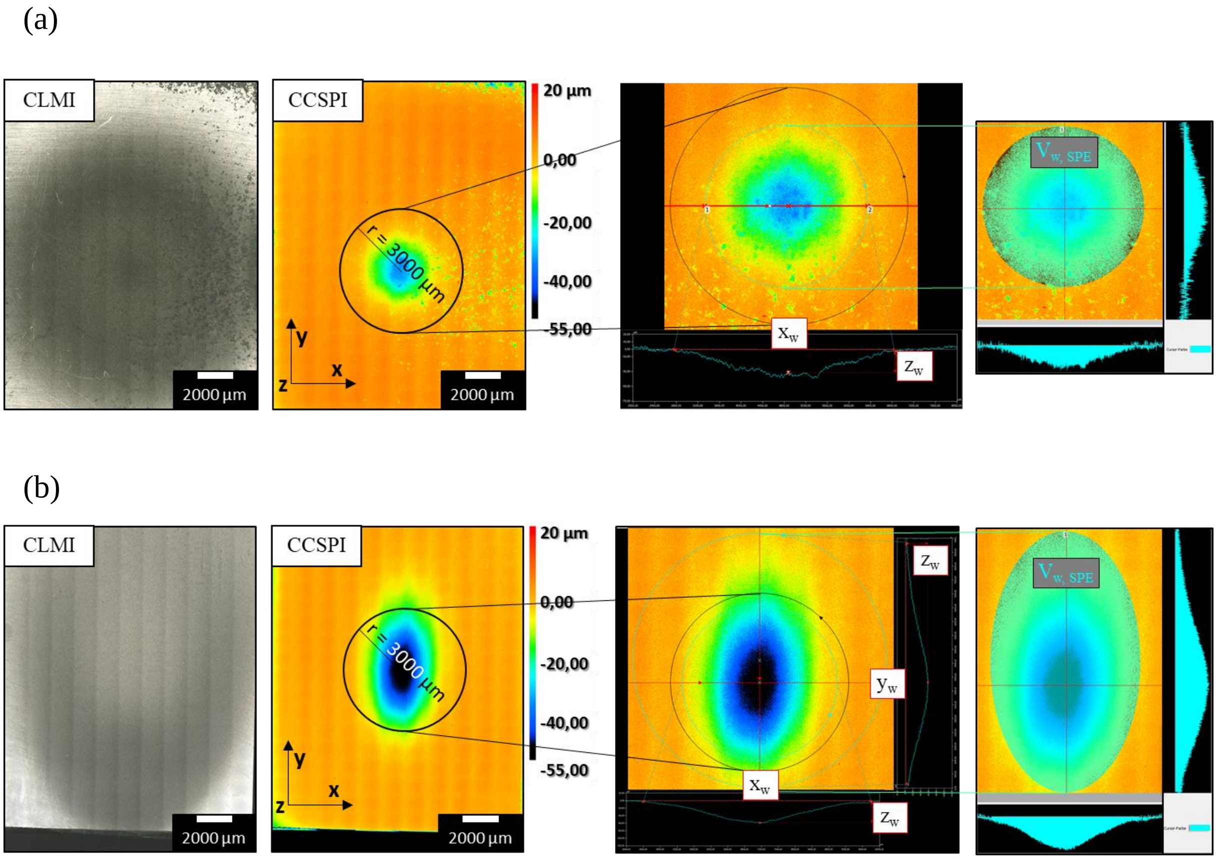
(a)
CLMI
2000 µm
CCSPI
r = 3000 µm
y
x
z
2000 µm
20 µm
0,00
-20,00
-40,00
-55,00
x_w
z_w
$V_{w, SPE}$
(b)
CLMI
2000 µm
CCSPI
r = 3000 µm
y
x
z
2000 µm
20 µm
0,00
-20,00
-40,00
-55,00
z_w
y_w
x_w
z_w
$V_{w, SPE}$

Fig. 2

(a)

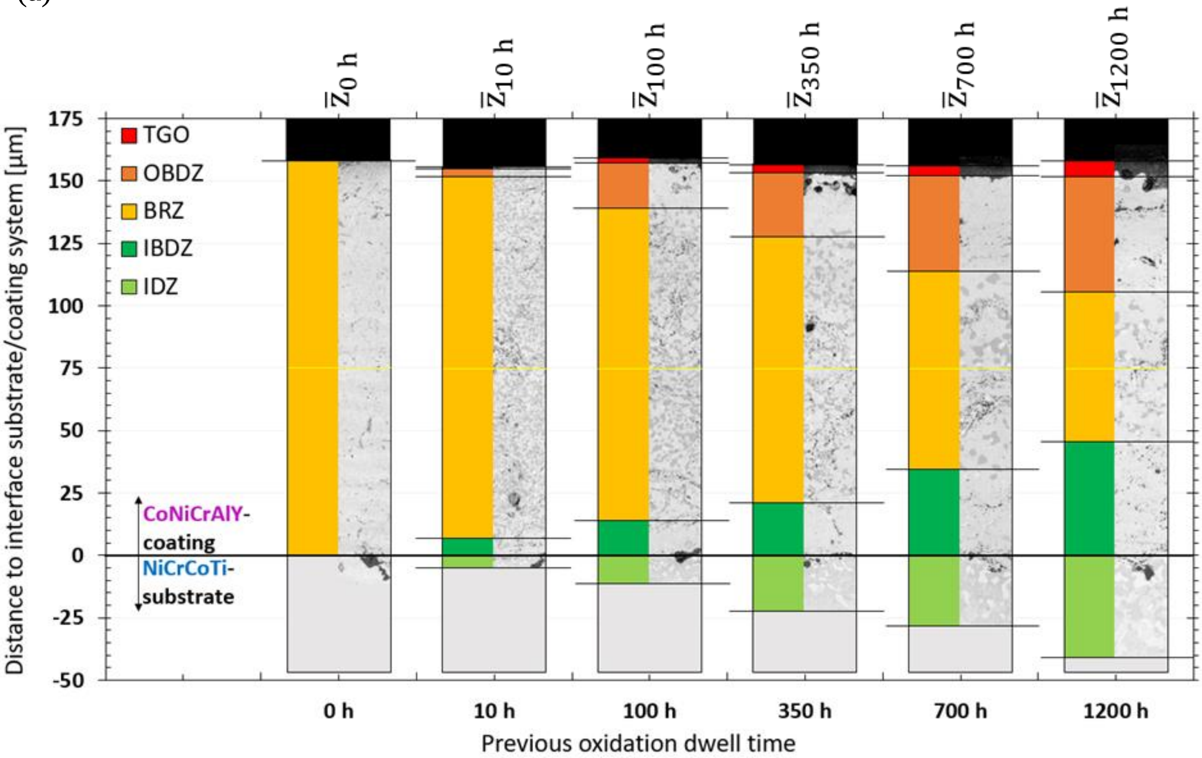
$\bar{z}_{0\,h}$
$\bar{z}_{10\,h}$
$\bar{z}_{100\,h}$
$\bar{z}_{350\,h}$
$\bar{z}_{700\,h}$
$\bar{z}_{1200\,h}$
🟥 TGO
🟧 OBDZ
🟨 BRZ
🟩 IBDZ
🟩 IDZ
Distance to interface substrate/coating system [µm]
175
150
125
100
75
50
25
0
-25
-50
CoNiCrAlY-coating
NiCrCoTi-substrate
0 h
10 h
100 h
350 h
700 h
1200 h
Previous oxidation dwell time

(b)

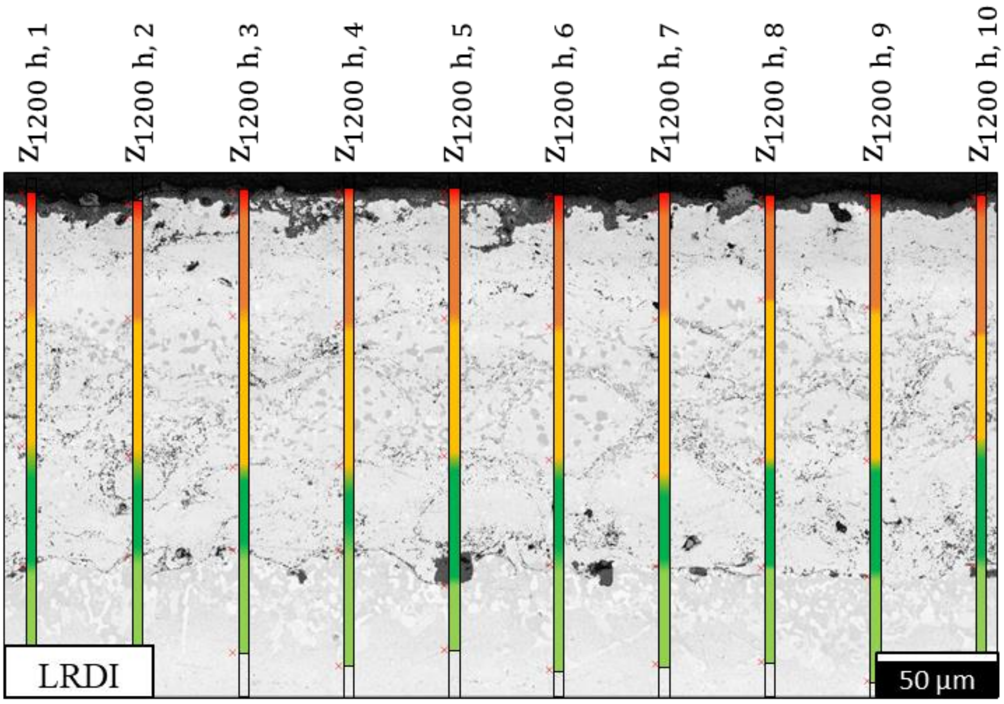
$z_{1200\,h,\,1}$
$z_{1200\,h,\,2}$
$z_{1200\,h,\,3}$
$z_{1200\,h,\,4}$
$z_{1200\,h,\,5}$
$z_{1200\,h,\,6}$
$z_{1200\,h,\,7}$
$z_{1200\,h,\,8}$
$z_{1200\,h,\,9}$
$z_{1200\,h,\,10}$
LRDI
50 µm

Fig. 3

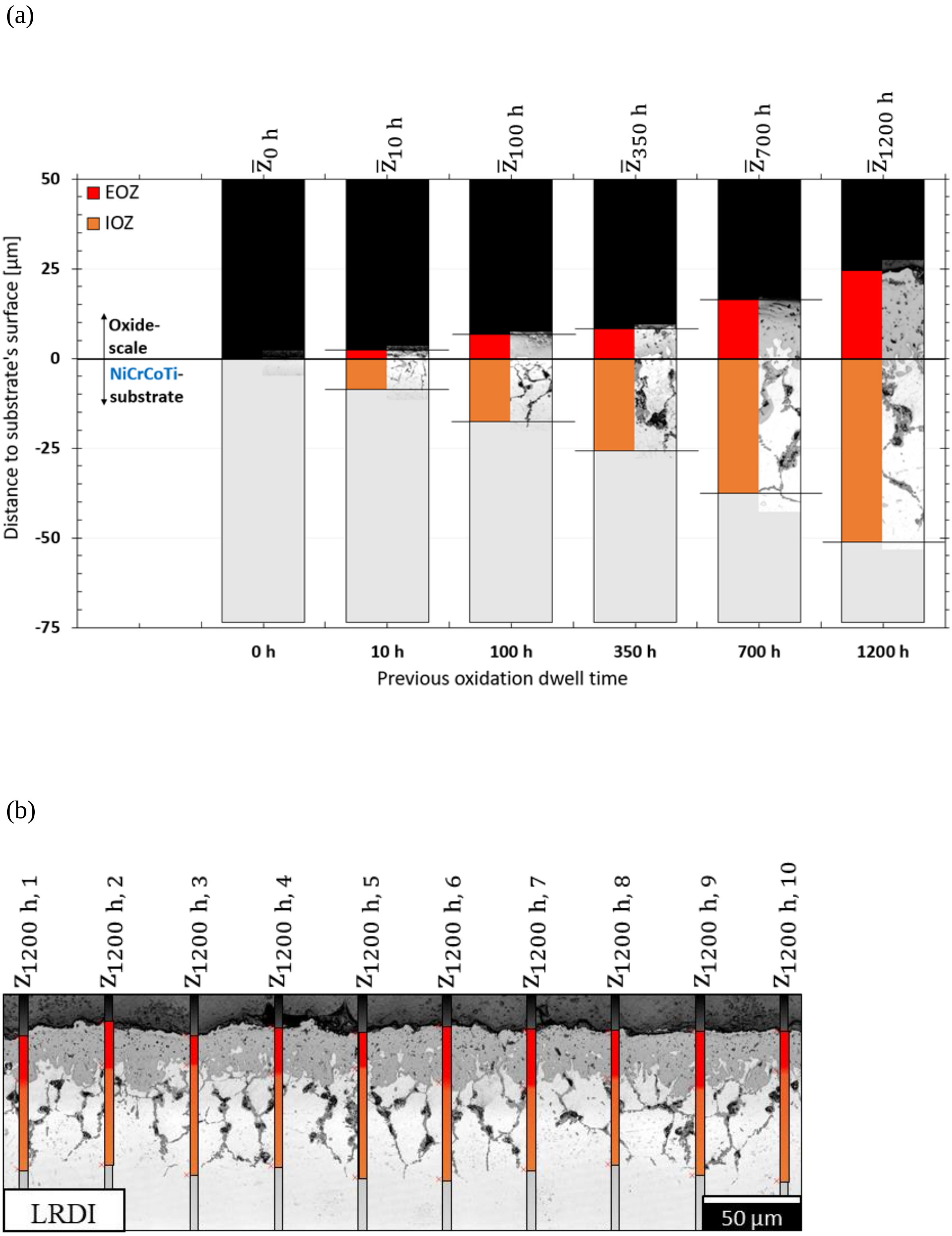
(a)
$\bar{z}_{0\,h}$
$\bar{z}_{10\,h}$
$\bar{z}_{100\,h}$
$\bar{z}_{350\,h}$
$\bar{z}_{700\,h}$
$\bar{z}_{1200\,h}$
🟥 EOZ
🟧 IOZ
Oxide-scale
NiCrCoTi-substrate
Distance to substrate's surface [µm]
50
25
0
-25
-50
-75
0 h
10 h
100 h
350 h
700 h
1200 h
Previous oxidation dwell time
(b)
$z_{1200\,h,\,1}$
$z_{1200\,h,\,2}$
$z_{1200\,h,\,3}$
$z_{1200\,h,\,4}$
$z_{1200\,h,\,5}$
$z_{1200\,h,\,6}$
$z_{1200\,h,\,7}$
$z_{1200\,h,\,8}$
$z_{1200\,h,\,9}$
$z_{1200\,h,\,10}$
LRDI
50 µm

Fig. 4

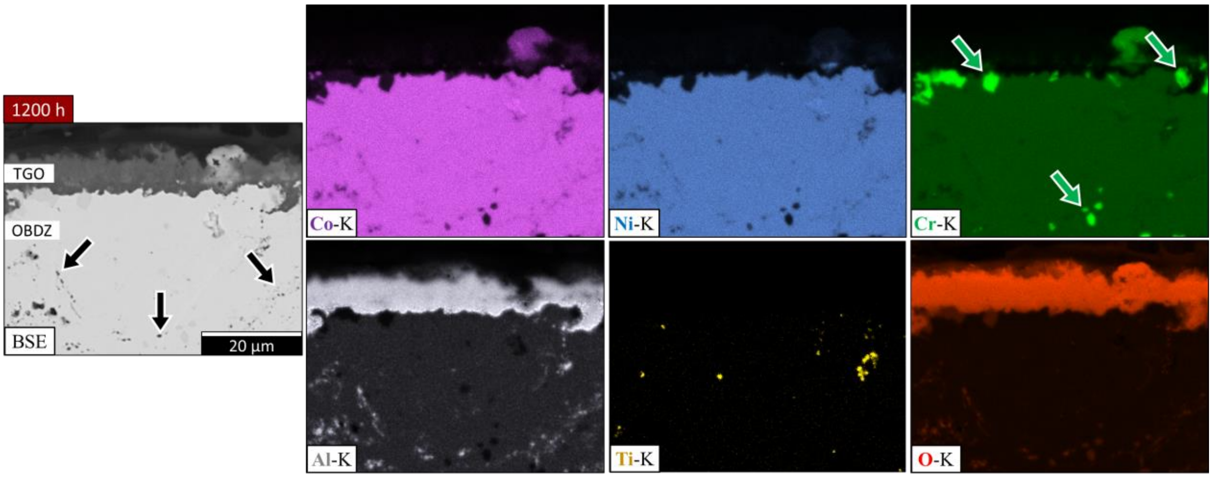

Fig. 5

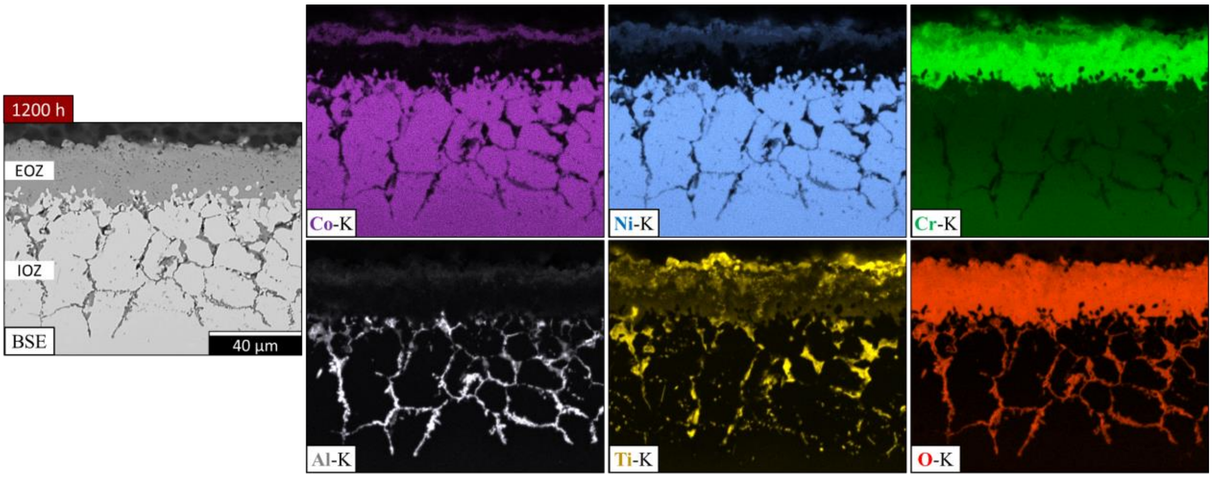

Fig. 6

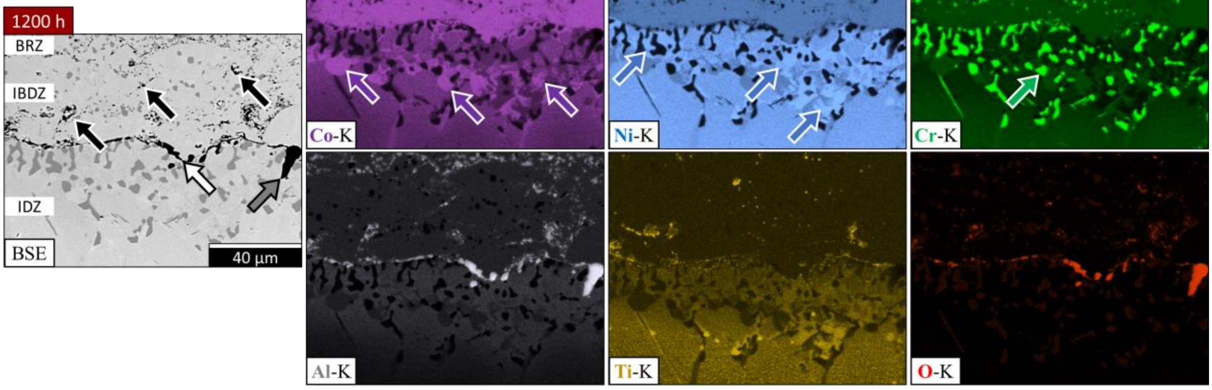

Fig. 7

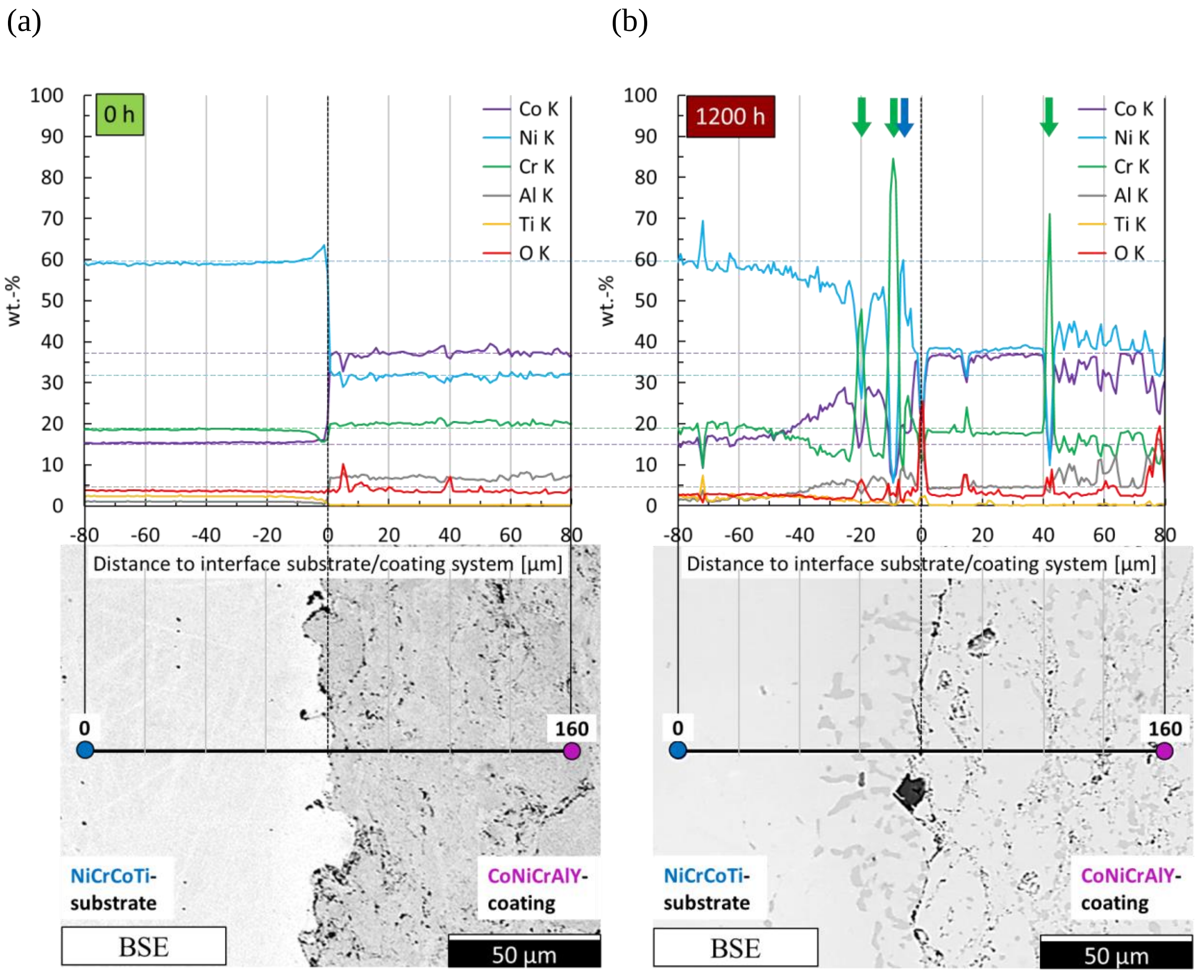
(a)
(b)
0 h
1200 h
Co K
Ni K
Cr K
Al K
Ti K
O K
wt.-%
100
90
80
70
60
50
40
30
20
10
0
-80
-60
-40
-20
0
20
40
60
80
Distance to interface substrate/coating system [µm]
0
160
NiCrCoTi-substrate
CoNiCrAlY-coating
BSE
50 µm

Fig. 8

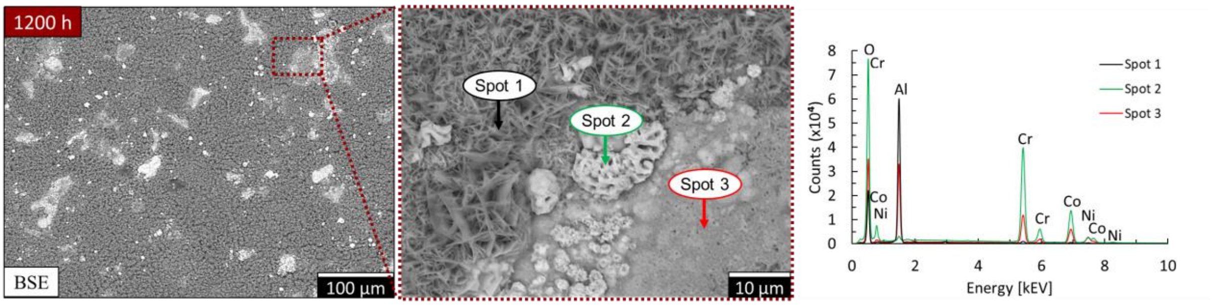
1200 h
BSE
100 µm
Spot 1
Spot 2
Spot 3
10 µm
Counts (x10⁴)
Energy [keV]
0
1
2
3
4
5
6
7
8
0
2
4
6
8
10
O
Cr
Al
Co
Ni
Cr
Cr
Co
Ni
Co
Ni
Spot 1
Spot 2
Spot 3

Fig. 9

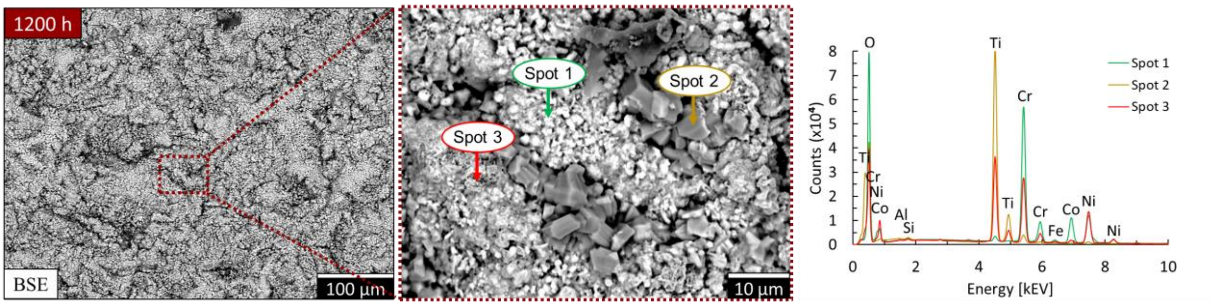
1200 h
BSE
100 µm
Spot 1
Spot 2
Spot 3
10 µm
Counts (x10^4)
0
1
2
3
4
5
6
7
8
O
Ti
Cr
Ni
Co
Al
Si
Ti
Cr
Ti
Cr
Fe
Co
Ni
Ni
Spot 1
Spot 2
Spot 3
0
2
4
6
8
10
Energy [kEV]

Fig.10

(a)

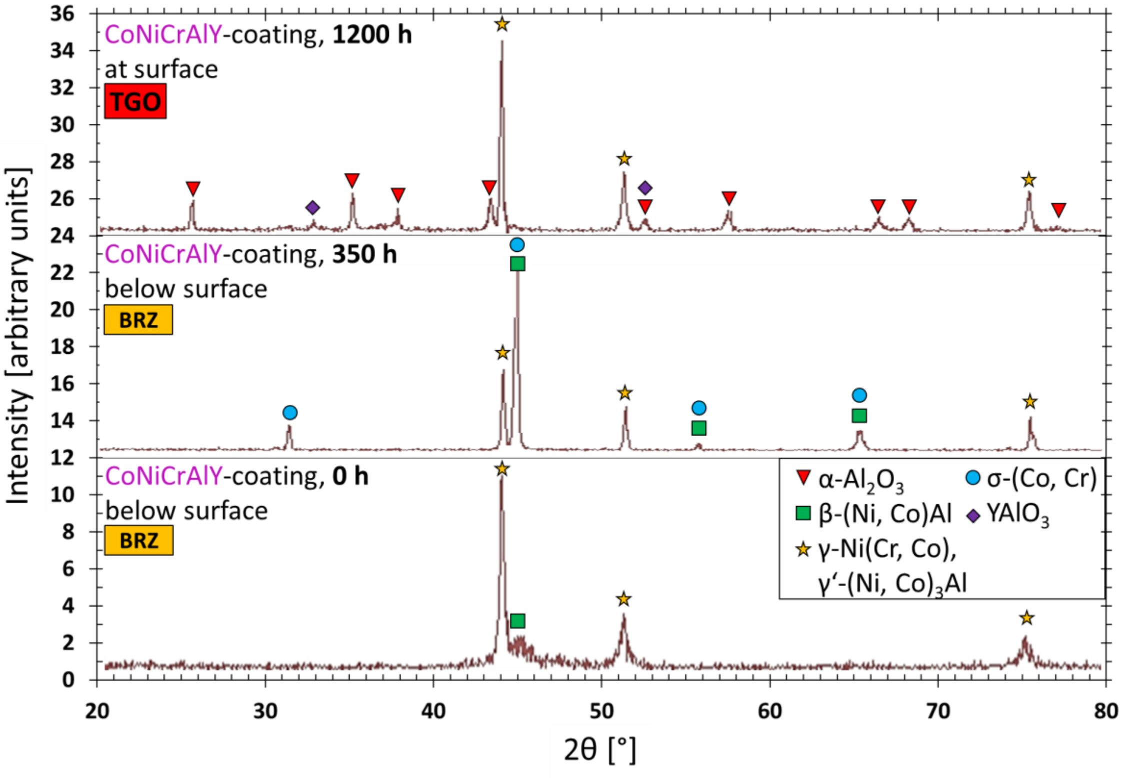
CoNiCrAlY-coating, 1200 h
at surface
TGO
CoNiCrAlY-coating, 350 h
below surface
BRZ
CoNiCrAlY-coating, 0 h
below surface
BRZ
α-Al2O3
σ-(Co, Cr)
β-(Ni, Co)Al
YAlO3
γ-Ni(Cr, Co),
γ'-(Ni, Co)3Al
Intensity [arbitrary units]
2θ [°]
0
2
4
6
8
10
12
14
16
18
20
22
24
26
28
30
32
34
36
20
30
40
50
60
70
80

(b)

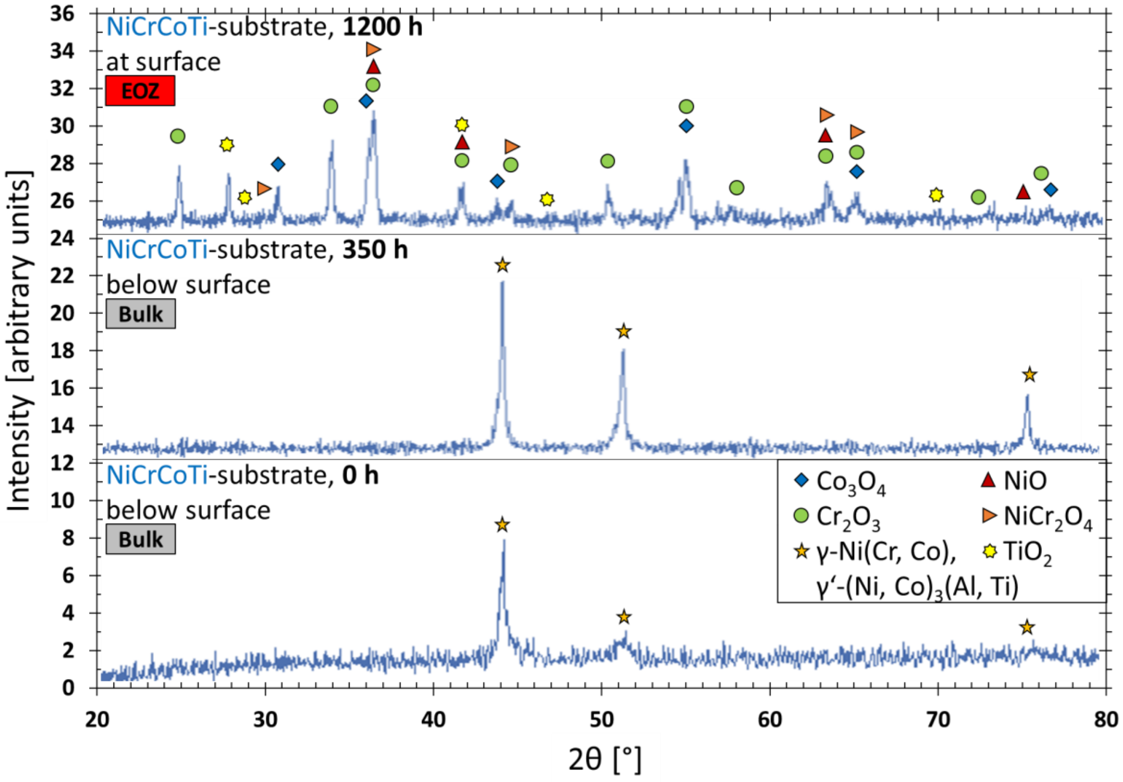
NiCrCoTi-substrate, 1200 h
at surface
EOZ
NiCrCoTi-substrate, 350 h
below surface
Bulk
NiCrCoTi-substrate, 0 h
below surface
Bulk
Co3O4
NiO
Cr2O3
NiCr2O4
γ-Ni(Cr, Co),
TiO2
γ'-(Ni, Co)3(Al, Ti)
Intensity [arbitrary units]
2θ [°]
0
2
4
6
8
10
12
14
16
18
20
22
24
26
28
30
32
34
36
20
30
40
50
60
70
80

Fig. 11

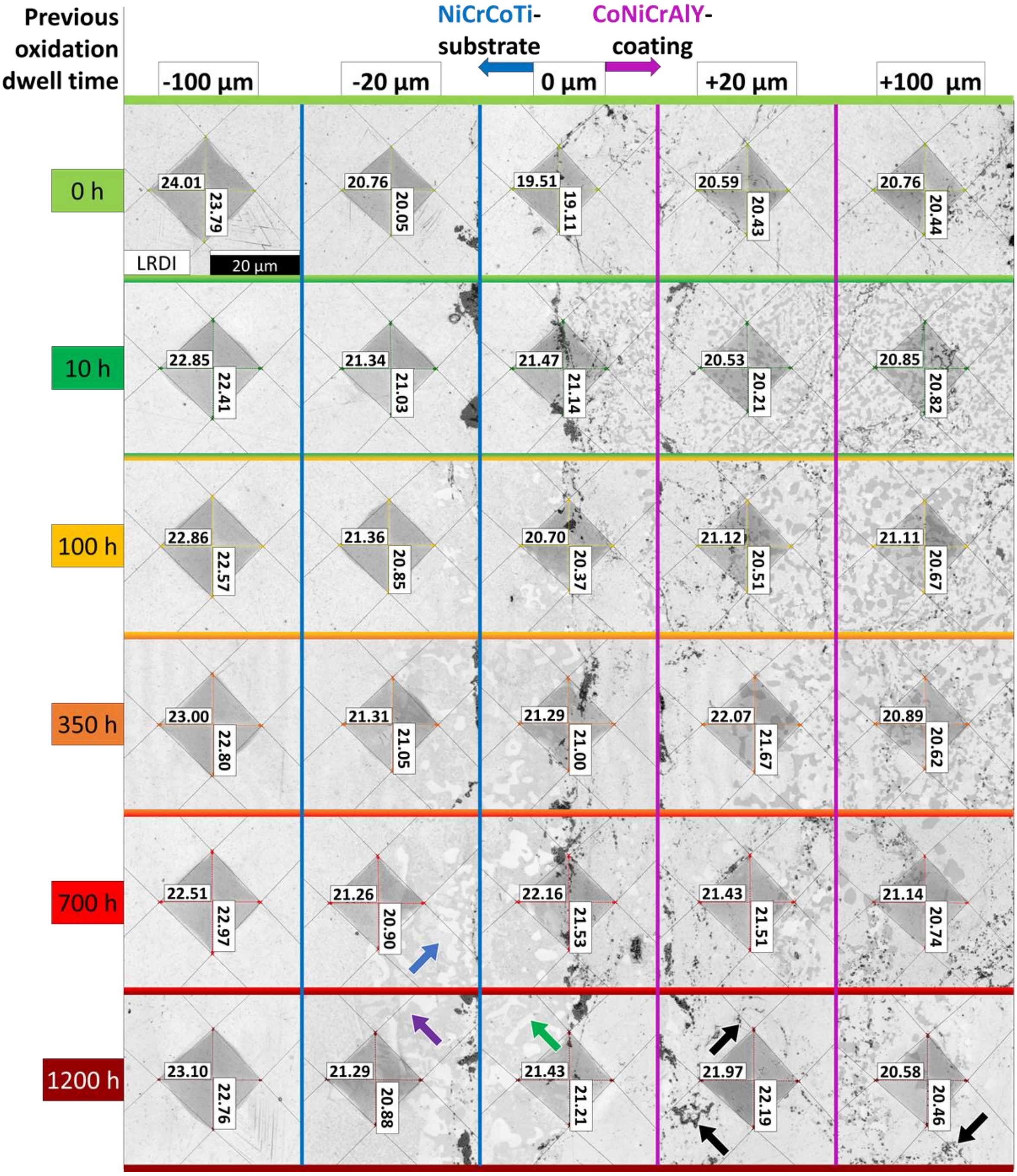
Previous oxidation dwell time
NiCrCoTi- substrate
CoNiCrAlY- coating
-100 µm
-20 µm
0 µm
+20 µm
+100 µm
0 h
24.01
23.79
LRDI
20 µm
20.76
20.05
19.51
19.11
20.59
20.43
20.76
20.44
10 h
22.85
22.41
21.34
21.03
21.47
21.14
20.53
20.21
20.85
20.82
100 h
22.86
22.57
21.36
20.85
20.70
20.37
21.12
20.51
21.11
20.67
350 h
23.00
22.80
21.31
21.05
21.29
21.00
22.07
21.67
20.89
20.62
700 h
22.51
22.97
21.26
20.90
22.16
21.53
21.43
21.51
21.14
20.74
1200 h
23.10
22.76
21.29
20.88
21.43
21.21
21.97
22.19
20.58
20.46

Fig. 12

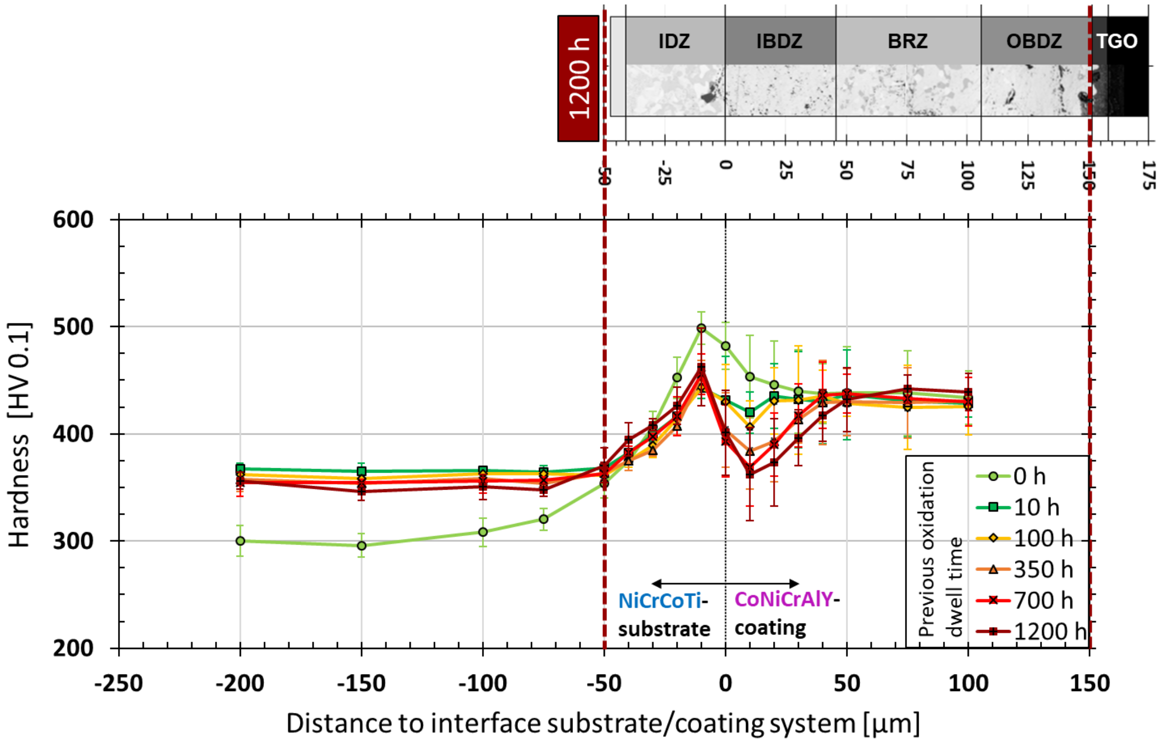
1200 h
IDZ
IBDZ
BRZ
OBDZ
TGO
-50
-25
0
25
50
75
100
125
150
175
600
500
400
300
200
Hardness [HV 0.1]
-250
-200
-150
-100
-50
0
50
100
150
Distance to interface substrate/coating system [µm]
NiCrCoTi-
substrate
CoNiCrAlY-
coating
Previous oxidation
dwell time
0 h
10 h
100 h
350 h
700 h
1200 h

Fig. 13

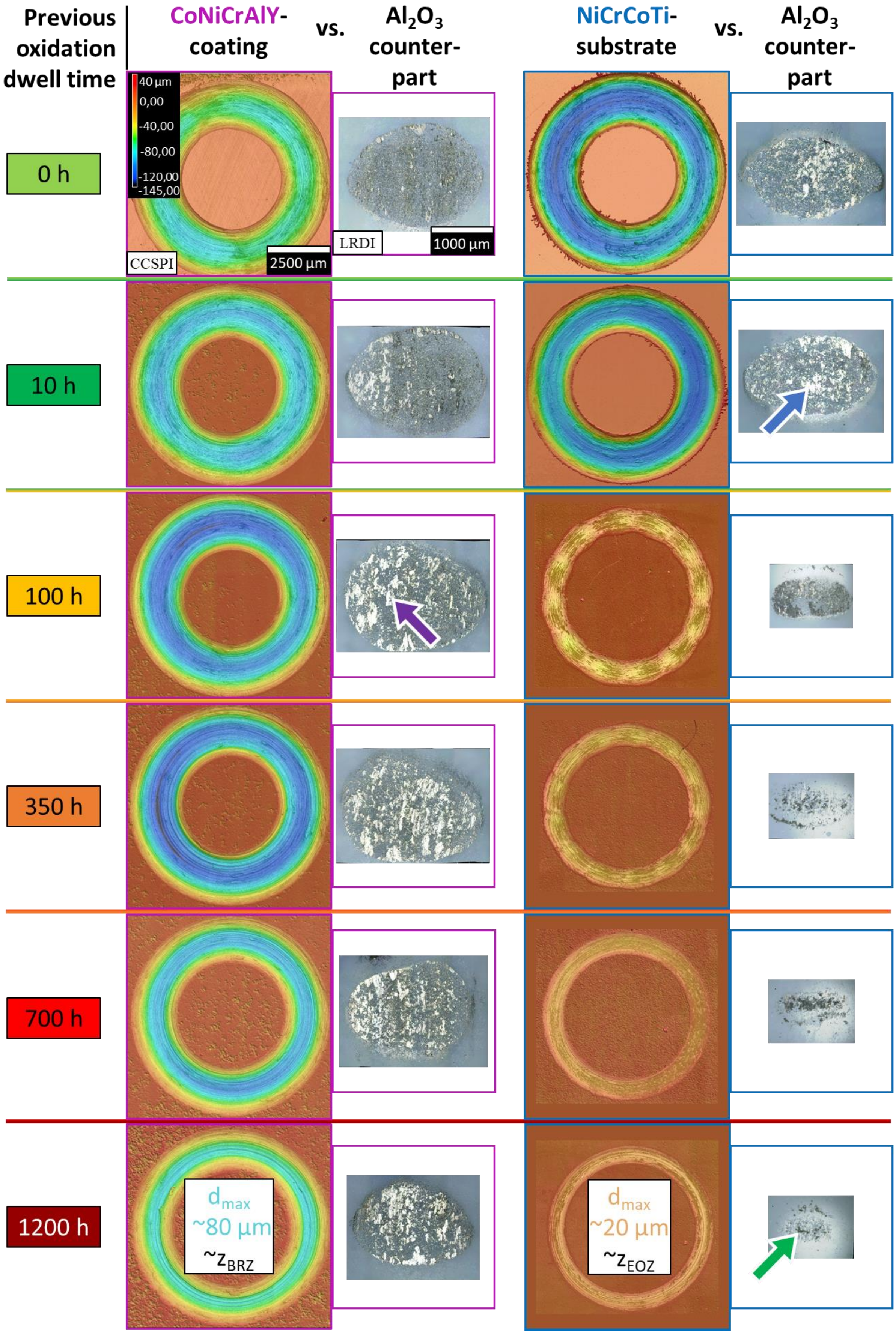
Previous oxidation dwell time
CoNiCrAlY-coating
vs.
Al_2O_3 counter-part
NiCrCoTi-substrate
vs.
Al_2O_3 counter-part
40 µm
0,00
-40,00
-80,00
-120,00
-145,00
CCSPI
2500 µm
LRDI
1000 µm
0 h
10 h
100 h
350 h
700 h
1200 h
d_{max} ~80 µm ~Z_{BRZ}
d_{max} ~20 µm ~Z_{EOZ}

Fig. 14

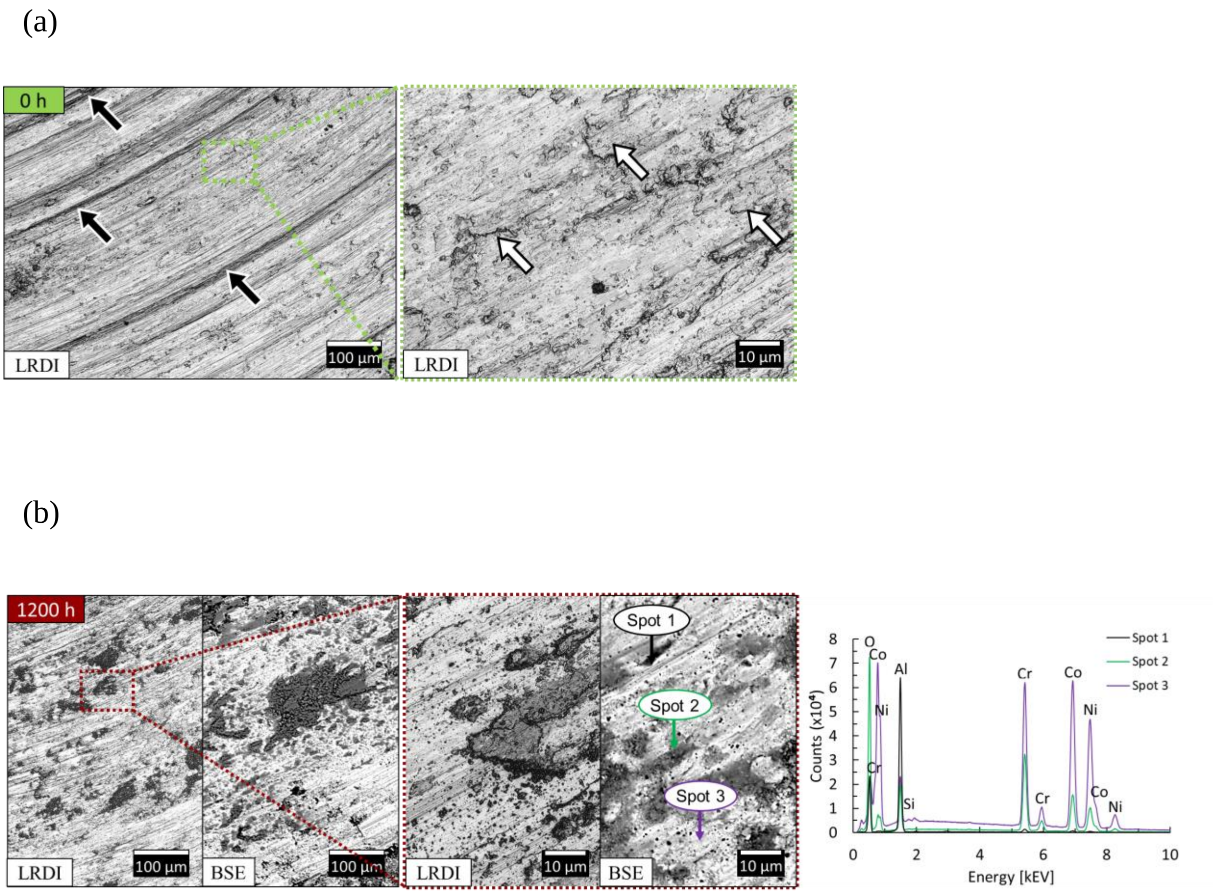
(a)
0 h
LRDI
100 µm
LRDI
10 µm
(b)
1200 h
LRDI
100 µm
BSE
100 µm
LRDI
10 µm
BSE
10 µm
Spot 1
Spot 2
Spot 3
Counts (x10⁴)
Energy [kEV]
0
1
2
3
4
5
6
7
8
0
2
4
6
8
10
O
Co
Ni
Cr
Al
Si
Cr
Cr
Co
Ni
Co
Ni
Spot 1
Spot 2
Spot 3

Fig. 15

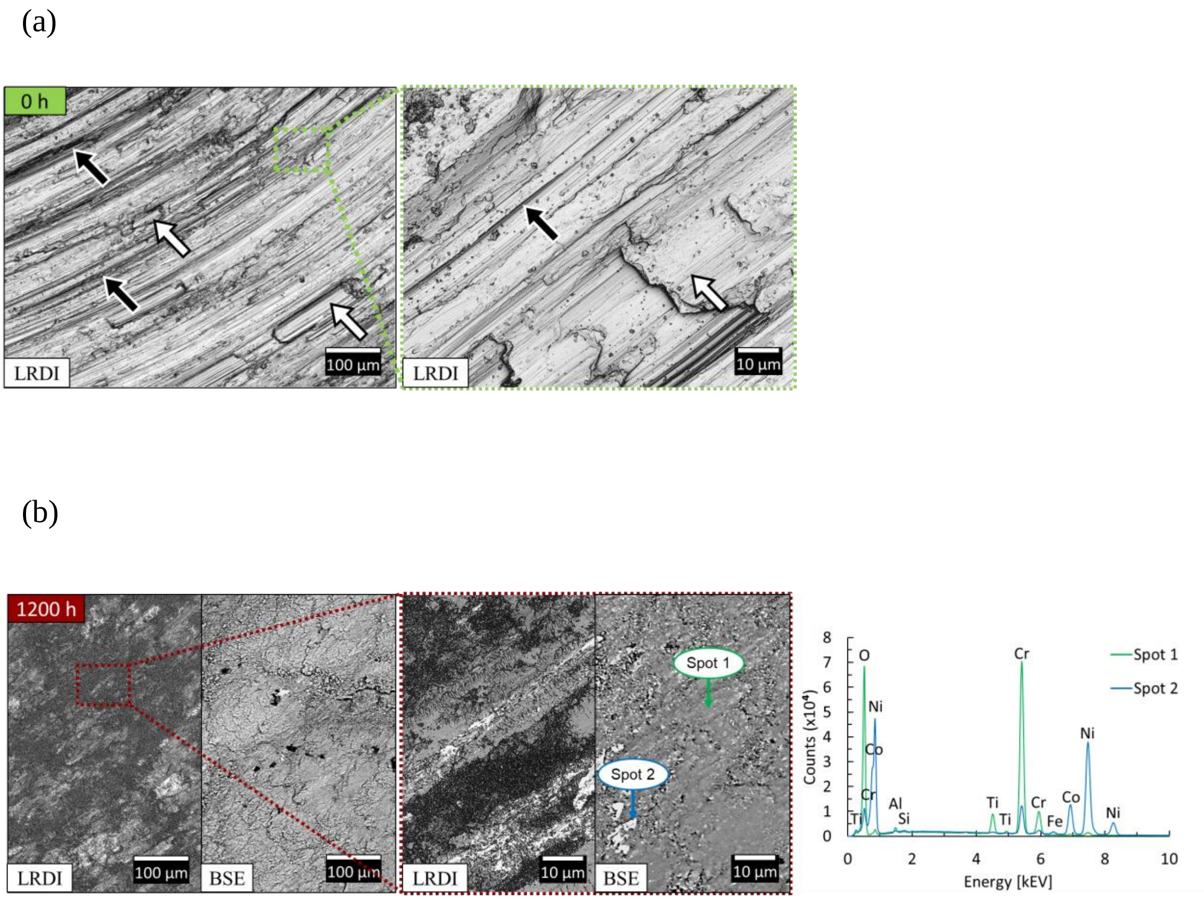
(a)
0 h
LRDI
100 µm
LRDI
10 µm
(b)
1200 h
LRDI
100 µm
BSE
100 µm
LRDI
10 µm
BSE
10 µm
Spot 1
Spot 2
Counts (x10⁴)
0
1
2
3
4
5
6
7
8
Energy [kEV]
0
2
4
6
8
10
O
Ni
Co
Cr
Ti
Al
Si
Ti
Ti
Cr
Cr
Fe
Co
Ni
Ni
Spot 1
Spot 2

Fig. 16

(a)

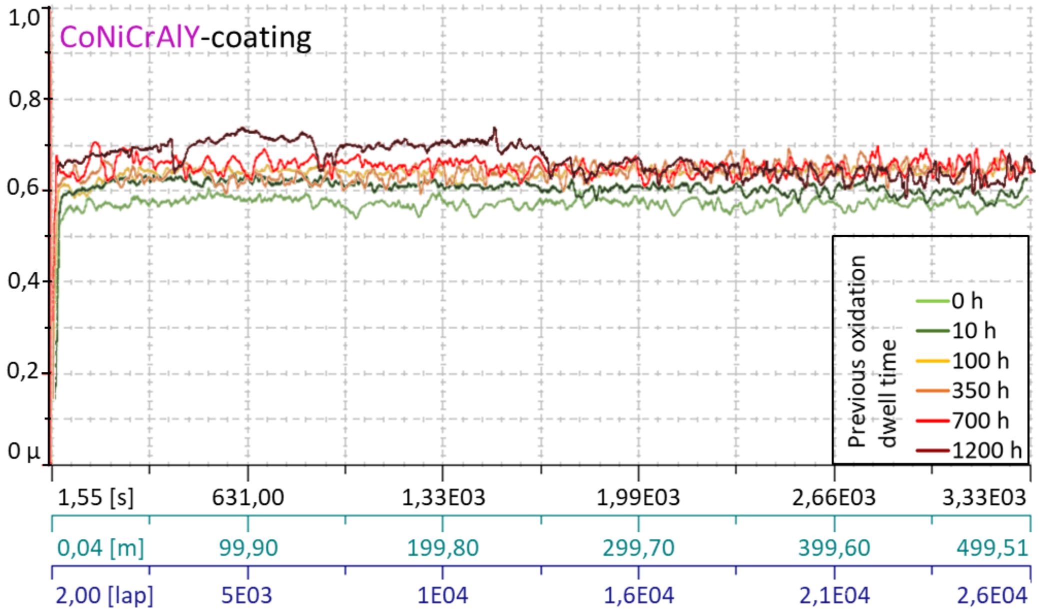
CoNiCrAlY-coating
1,0
0,8
0,6
0,4
0,2
0 µ
1,55 [s]
631,00
1,33E03
1,99E03
2,66E03
3,33E03
0,04 [m]
99,90
199,80
299,70
399,60
499,51
2,00 [lap]
5E03
1E04
1,6E04
2,1E04
2,6E04
Previous oxidation dwell time
0 h
10 h
100 h
350 h
700 h
1200 h

(b)

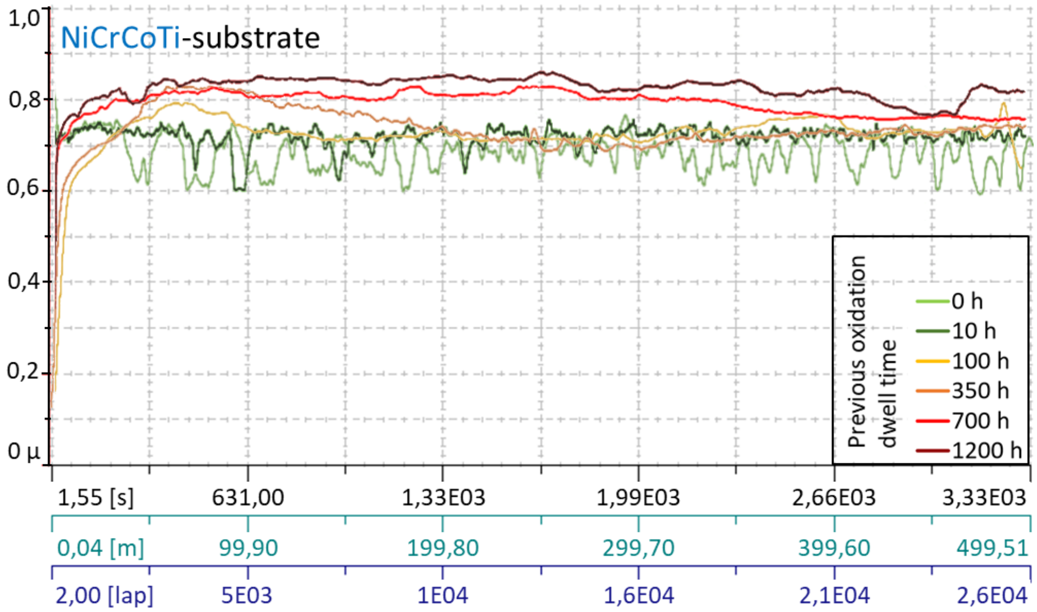
NiCrCoTi-substrate
1,0
0,8
0,6
0,4
0,2
0 µ
1,55 [s]
631,00
1,33E03
1,99E03
2,66E03
3,33E03
0,04 [m]
99,90
199,80
299,70
399,60
499,51
2,00 [lap]
5E03
1E04
1,6E04
2,1E04
2,6E04
Previous oxidation dwell time
0 h
10 h
100 h
350 h
700 h
1200 h

Fig. 17

(a)

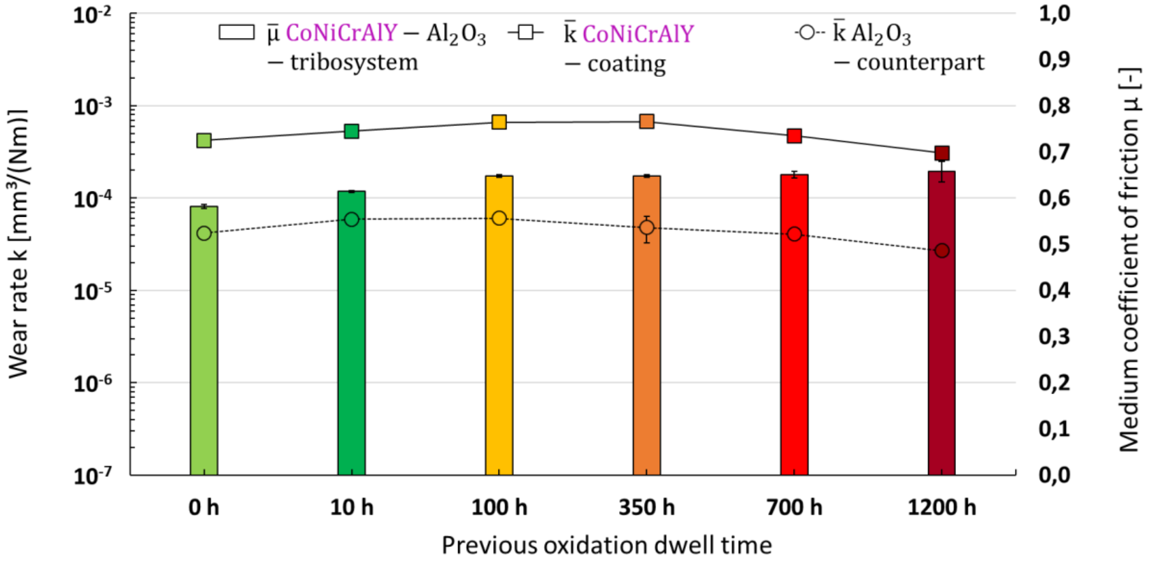
$\bar{\mu}$ CoNiCrAlY – Al_2O_3 – tribosystem
$\bar{k}$ CoNiCrAlY – coating
$\bar{k}$ Al_2O_3 – counterpart
Wear rate k [mm³/(Nm)]
10^{-2}
10^{-3}
10^{-4}
10^{-5}
10^{-6}
10^{-7}
Medium coefficient of friction μ [-]
1,0
0,9
0,8
0,7
0,6
0,5
0,4
0,3
0,2
0,1
0,0
0 h
10 h
100 h
350 h
700 h
1200 h
Previous oxidation dwell time

(b)

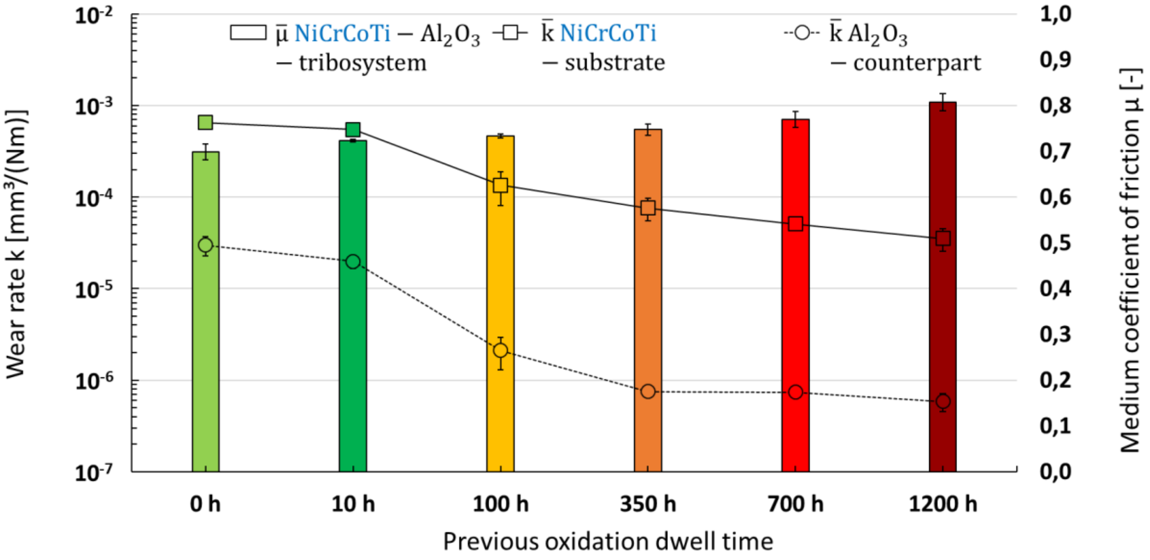
$\bar{\mu}$ NiCrCoTi – Al_2O_3 – tribosystem
$\bar{k}$ NiCrCoTi – substrate
$\bar{k}$ Al_2O_3 – counterpart
Wear rate k [mm³/(Nm)]
10^{-2}
10^{-3}
10^{-4}
10^{-5}
10^{-6}
10^{-7}
Medium coefficient of friction μ [-]
1,0
0,9
0,8
0,7
0,6
0,5
0,4
0,3
0,2
0,1
0,0
0 h
10 h
100 h
350 h
700 h
1200 h
Previous oxidation dwell time

Fig. 18

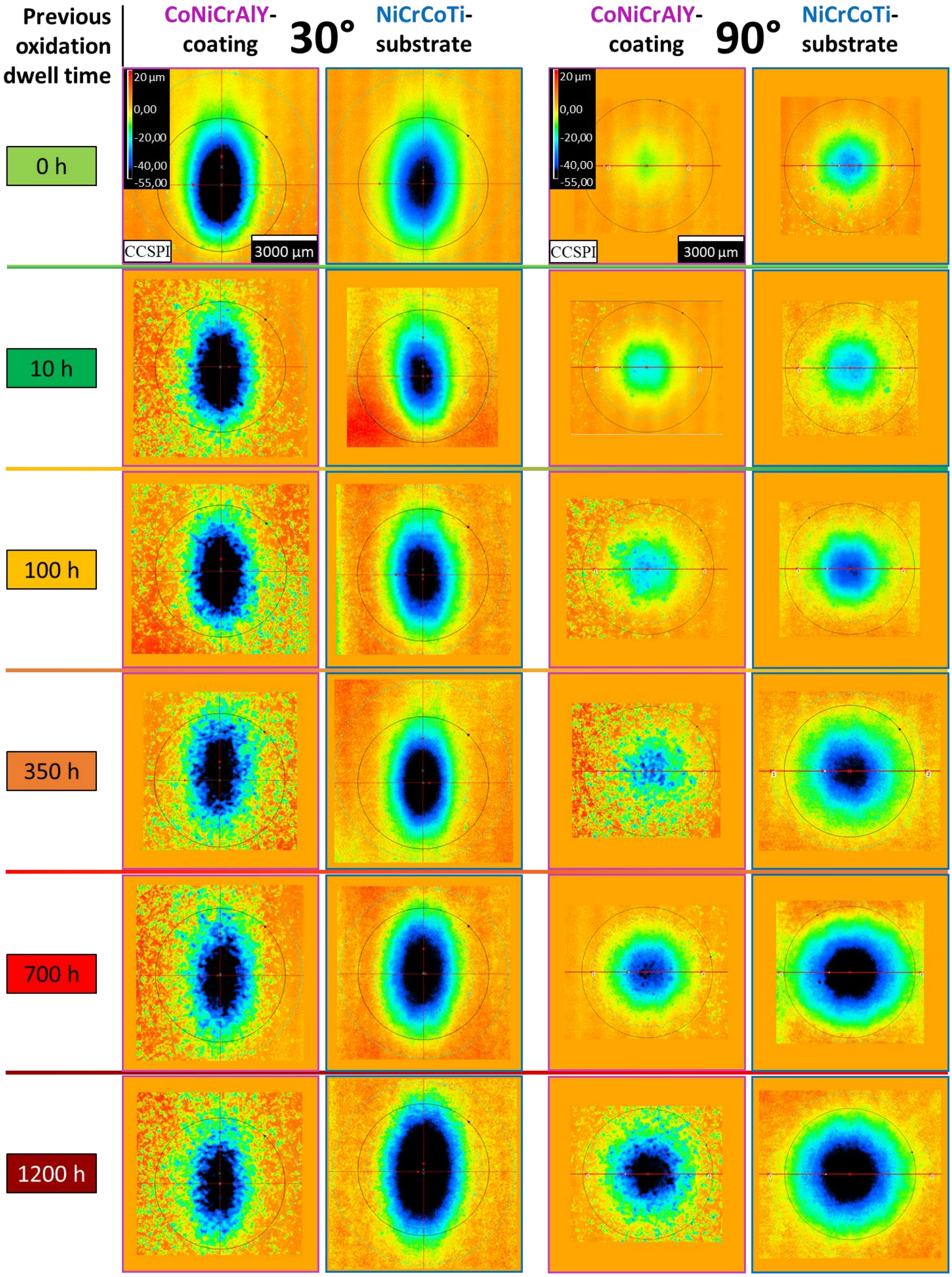
Previous oxidation dwell time
CoNiCrAlY-coating
30°
NiCrCoTi-substrate
CoNiCrAlY-coating
90°
NiCrCoTi-substrate
20 µm
0,00
-20,00
-40,00
-55,00
CCSPI
3000 µm
0 h
10 h
100 h
350 h
700 h
1200 h

Fig. 19

(a)

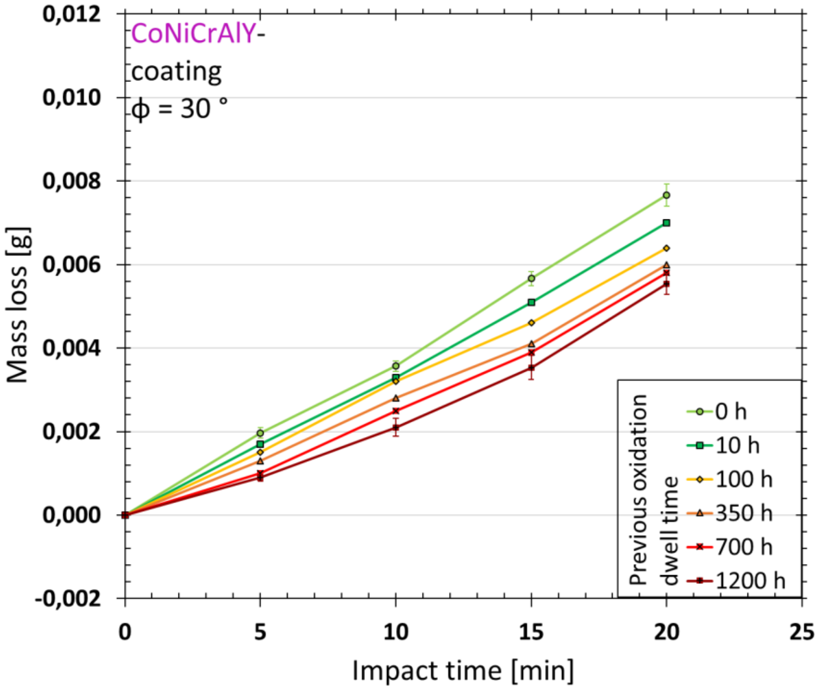
CoNiCrAlY-
coating
ϕ = 30 °
Mass loss [g]
0,012
0,010
0,008
0,006
0,004
0,002
0,000
-0,002
0
5
10
15
20
25
Impact time [min]
Previous oxidation
dwell time
0 h
10 h
100 h
350 h
700 h
1200 h

(b)

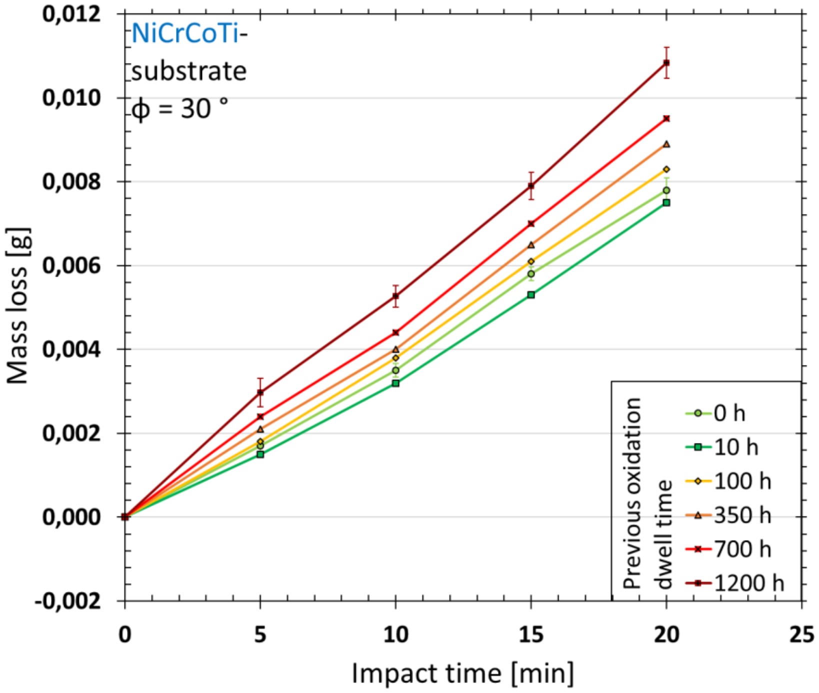
NiCrCoTi-
substrate
ϕ = 30 °
Mass loss [g]
0,012
0,010
0,008
0,006
0,004
0,002
0,000
-0,002
0
5
10
15
20
25
Impact time [min]
Previous oxidation
dwell time
0 h
10 h
100 h
350 h
700 h
1200 h

Fig. 20

(a)

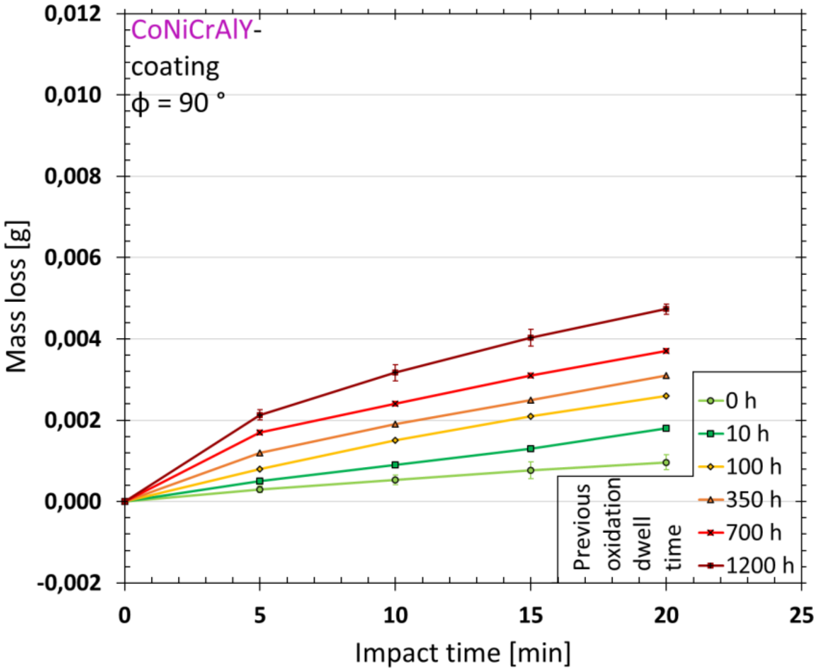
CoNiCrAlY-coating
ϕ = 90 °
Mass loss [g]
0,012
0,010
0,008
0,006
0,004
0,002
0,000
-0,002
0
5
10
15
20
25
Impact time [min]
Previous oxidation dwell time
0 h
10 h
100 h
350 h
700 h
1200 h

(b)

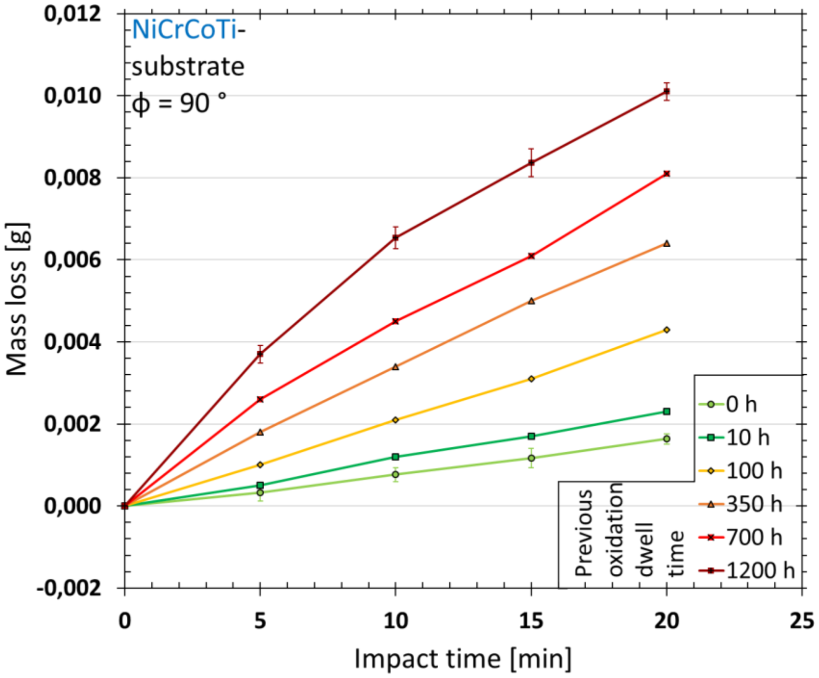
NiCrCoTi-substrate
ϕ = 90 °
Mass loss [g]
0,012
0,010
0,008
0,006
0,004
0,002
0,000
-0,002
0
5
10
15
20
25
Impact time [min]
Previous oxidation dwell time
0 h
10 h
100 h
350 h
700 h
1200 h

Fig. 21

Suggested reviewers

Prof. Dr. Lech Pawlowski - lech.pawlowski@unilim.fr

University of Limoges
Institut de recherche sur les céramiques IRCER
Limoges, France, Fr-87068

Dr. Giovanni Bolelli - giovanni.bolelli@unimore.it

University of Modena and Reggio Emilia
Department of Engineering "Enzo Ferrari"
Modena, Italy, I-41125

Prof. Dr. Shrikant Joshi - shrikant.joshi@hv.se

University West
Department of Engineering Science
Trollhattan, Sweden, S-46153

CRediT author statement

Markus Kiryc: Conceptualization, Methodology, Formal analysis, Investigation, Data curation, Visualization, Writing - original draft

Deniz Kurumlu: Resources, Review & editing

Gunther Eggeler: Resources, Review & editing

Robert Vaßen: Resources, Review & editing

Gabriela Marginean: Resources, Review & editing

Declaration of interests

☒The authors declare that they have no known competing financial interests or personal relationships that could have appeared to influence the work reported in this paper.

☐The authors declare the following financial interests/personal relationships which may be considered as potential competing interests: